

**Bangor University**

## **DOCTOR OF PHILOSOPHY**

### **Photo-effects in Organic MIS Devices and Related Structures**

Rostirolla, Bruno

*Award date:*  
2019

*Awarding institution:*  
Bangor University

[Link to publication](#)

#### **General rights**

Copyright and moral rights for the publications made accessible in the public portal are retained by the authors and/or other copyright owners and it is a condition of accessing publications that users recognise and abide by the legal requirements associated with these rights.

- Users may download and print one copy of any publication from the public portal for the purpose of private study or research.
- You may not further distribute the material or use it for any profit-making activity or commercial gain
- You may freely distribute the URL identifying the publication in the public portal ?

#### **Take down policy**

If you believe that this document breaches copyright please contact us providing details, and we will remove access to the work immediately and investigate your claim.

Download date: 19. Sept. 2024

BANGOR UNIVERSITY

# Photo-effects in Organic MIS Devices and Related Structures

by

Bruno Rostirolla

A thesis submitted for the degree of Doctor of Philosophy

College of Physical and Applied Sciences

School of Electronic Engineering

2018

# TABLE OF CONTENTS

<i>DECLARATION OF AUTHORSHIP</i>	<i>ii</i>
<i>LIST OF FIGURES</i>	<i>vi</i>
<i>LIST OF TABLES</i>	<i>x</i>
<i>ABSTRACT</i>	<i>xi</i>
<i>ACKNOWLEDGEMENTS</i>	<i>xii</i>
<b>1. INTRODUCTION</b>	<b>1</b>
<i>REFERENCES</i>	<i>5</i>
<b>2. BACKGROUND CONCEPTS AND LITERATURE REVIEW</b>	<b>7</b>
2.1. <i>Introduction</i>	<i>7</i>
2.2. <i>Background to Organic Semiconductors</i>	<i>8</i>
2.2.1. <i>Hybridization &amp; Molecular Orbitals</i>	<i>8</i>
2.2.2. <i>Light Absorption</i>	<i>11</i>
2.2.3. <i>Charge Transport</i>	<i>13</i>
2.3. <i>Metal-Insulator-Semiconductor Capacitor</i>	<i>15</i>
2.3.1. <i>Ideal MIS Capacitor</i>	<i>16</i>
2.3.2. <i>Admittance of MIS Capacitors</i>	<i>20</i>
2.3.3. <i>Doping Density and the Mott-Schottky Analysis</i>	<i>22</i>
2.3.4. <i>Real MIS Capacitors and Equivalent Circuits</i>	<i>23</i>
2.3.4.1. <i>Contact Resistance</i>	<i>26</i>
2.3.4.2. <i>Time Constant Dispersion</i>	<i>27</i>
2.3.4.3. <i>Flatband Voltage</i>	<i>28</i>
2.3.4.4. <i>Insulator Leakage</i>	<i>29</i>
2.3.4.5. <i>Interface States</i>	<i>30</i>
2.3.4.6. <i>Lateral Conduction</i>	<i>32</i>
2.4. <i>Organic MIS Capacitors</i>	<i>32</i>
<i>CONCLUSION</i>	<i>37</i>
<i>REFERENCES</i>	<i>39</i>

<b>3. MATERIALS &amp; METHODS</b>	<b>41</b>
3.1. <i>Introduction</i>	41
3.2. <i>Materials</i>	42
3.2.1. <i>Poly(3-hexylthiophene)</i>	42
3.2.2. <i>[6,6]-Phenyl C61 butyric acid methyl ester</i>	43
3.2.3. <i>Dinaphtho[2,3-b:2',3'-f]thieno[3,2-b]thiophene</i>	44
3.2.4. <i>Poly(4-vinyl phenol)</i>	45
3.2.5. <i>Polystyrene</i>	46
3.3. <i>Fabrication of organic-based devices</i>	47
3.3.1. <i>Substrate Cleaning</i>	47
3.3.2. <i>Spin-Coating</i>	48
3.3.3. <i>Thermal Evaporation</i>	48
3.4. <i>Measurement Techniques</i>	49
3.4.1. <i>Admittance Experiments</i>	49
3.4.2. <i>Current-time Experiments</i>	50
REFERENCES	51
<b>4. P3HT:PCBM-BASED DEVICES</b>	<b>53</b>
4.1. <i>Introduction</i>	53
4.2. <i>P3HT:PCBM-based MIS capacitors</i>	54
4.2.1. <i>Overall behaviour of P3HT:PCBM-based capacitors</i>	54
4.2.2. <i>Effect of light</i>	59
4.2.3. <i>Effect of NIR light</i>	64
4.3. <i>P3HT:PCBM Charge-Injection-Device</i>	73
CONCLUSION	76
REFERENCES	77
<b>5. DNTT-BASED DEVICES</b>	<b>78</b>
5.1. <i>Introduction</i>	78
5.2. <i>DNTT-based MIS capacitors</i>	80
5.2.1. <i>Overall behaviour of DNTT-based capacitors</i>	80
5.2.2. <i>Effect of Measurement Frequency</i>	85
5.2.3. <i>Effect of Temperature</i>	86
5.2.4. <i>Effect of Light</i>	90

5.2.5. <i>Effect of Bias Stress</i>	94
5.3. <i>DNTT-based Thin-film Transistors</i>	98
5.3.1. <i>Characteristics immediately after fabrication</i>	100
5.3.2. <i>Characteristics after 2.5 days</i>	102
CONCLUSION	106
REFERENCES	108
<b>6. DEVELOPING THE PHOTOCAPACITANCE MODEL</b>	<b>109</b>
6.1. <i>Introduction</i>	109
6.2. <i>Photocapacitance Modelling</i>	109
CONCLUSION	124
REFERENCES	126
<b>7. CONCLUSIONS &amp; FURTHER WORK</b>	<b>127</b>
7.1. <i>Conclusions</i>	127
7.2. <i>Further Work</i>	129
APPENDIX A	131
PUBLICATIONS AND CONFERENCES	136

# LIST OF FIGURES

2.1	The three hybridization orbital configurations (a) $sp^3$ (b) $sp^2$ (c) $sp$ .	8
2.2	(a) Chemical representations of benzene. (b) $\sigma$ bonds and (c) $\pi$ bonds. (d) Result of the superposition of $\pi$ orbitals. The dashed line represents the plane formed by the carbon atoms.	9
2.3	Energy diagram scheme of $\pi$ - $\pi^*$ and $\sigma$ - $\sigma^*$ transitions.	10
2.4	Hopping mechanism representing holes (red) and electrons (blue) transport when an electric field (yellow arrow) is applied.	14
2.5	Schematic view of a MIS capacitor.	15
2.6	Flatband condition. $\chi$ is the electron affinity of the semiconductor.	16
2.7	Accumulation case.	17
2.8	Depletion case.	18
2.9	Capacitance-Voltage profile of an ideal MIS device based on a p-type semiconductor.	20
2.10	Mott-Schottky plot, describing the doping density and built-in voltage.	23
2.11	Equivalent circuit of a MIS capacitor in accumulation.	24
2.12	Equivalent circuit for a MIS capacitor in depletion.	25
2.13	Simulated (a) C-f and (b) $G/\omega$ -f for an ideal MIS capacitor driven from accumulation (black line) to full depletion (red line). Semiconductor layer thickness used was 200 nm, $C_I = 400$ pF, $R_B = 4400$ $\Omega$ and $C_B = 600$ pF.	26
2.14	Equivalent circuit for a MIS in depletion with contact resistance.	27
2.15	Equivalent circuit for a MIS device in depletion with a distribution of relaxation frequencies.	28
2.16	Horizontal shifts in C-V curve of MIS devices for $V_{FB} = 0$ (black line); $V_{FB} > 0$ (red line) and $V_{FB} < 0$ (green line).	28
2.17	Energy-band diagram showing conduction mechanism of (a) tunnelling, (b) thermionic emission, and (c) Frenkel-Poole emission.	30
2.18	Equivalent circuit of a MIS capacitor in depletion with insulator leakage effects.	30
2.19	Equivalent circuit of a MIS with a single interface state level.	31
2.20	Equivalent circuit of a MIS device with a distribution of interface state energies.	31
2.21	Experimental (a) and simulated (b) effect of light energy on the C-V response of P3HT-based MIS capacitors.	34
2.22	Estimated doping density deviations for (a) low doping densities; and (b) thin semiconductor layers.	36

2.23	Simulated C-V curves. The arrow indicates the increase in disorder/broadening of the DOS.	37
3.1	Chemical structure of regioregular P3HT	42
3.2	Chemical structure of PCBM.	44
3.3	Chemical structure of DNTT.	45
3.4	Chemical structure of (a) PVP and (b) PS.	46
3.5	Top view of the substrate holder. The grey square is a recess where the substrate fits while held by an o-ring and vacuum.	48
4.1	P3HT:PCBM-based MIS capacitor device structure.	54
4.2	(a) C-f and (b) loss-f curves of P3HT:PCBM-based MIS capacitor in the dark, under vacuum, at different applied gate voltages.	56
4.3	(a) C-V and (b) loss-V curves of P3HT:PCBM-based MIS capacitor in the dark, in vacuum, at 1 kHz.	57
4.4	Doping density NA as a function of depletion layer thickness for a P3HT:PCBM MIS capacitor	58
4.5	Absorbance of P3HT (red line), PCBM (black line) and P3HT:PCBM (green line) films.	59
4.6	C-V of P3HT:PCBM capacitors when exposed to different light wavelengths.	60
4.7	Loss-V of P3HT:PCBM capacitors when exposed to different light wavelengths.	62
4.8	(a) C-V and (b) loss-V of P3HT:PCBM capacitors in the dark before (black line) and after (red rhombus) being exposed to 600 nm light (green line).	63
4.9	Absorbance (black line) and shift in minimum capacitance (red dots) of a P3HT-only device exposed to different light wavelength.	65
4.10	C-V of a PCBM-only capacitor in the dark and when exposed to different light wavelengths.	66
4.11	I-V of a PVP-only MIM capacitor in the dark and when exposed to different light wavelengths.	67
4.12	Shifts in current when a P3HT:PCBM-based MIS capacitor was exposed to different light wavelengths. In the inset, the current-time experiment that originated each point.	68
4.13	Energy distribution scheme of a P3HT:PCBM-based MIS capacitor. Approximate values are in eV with respect to the vacuum level.	69
4.14	Current-time of a P3HT:PCBM MIS capacitor exposed to pulses of 500 nm at different applied gate voltages.	70
4.15	Current-time of a P3HT:PCBM MIS capacitor exposed to pulses of 900 nm at different applied gate voltages.	71
4.16	Magnitude of the current response when a P3HT:M012-based MIS capacitor was exposed to different light wavelengths.	72
4.17	Minimum capacitance of a P3HT:Klook MIS capacitor when exposed to different light wavelengths.	73
4.18	Structure of a CID based on PVP insulator and P3HT:PCBM blend as active layer.	74

4.19	Transfer of photo-created electrons from the 1st capacitor to the deeper potential well beneath the 2nd capacitor.	75
4.20	Current in (a) first and (b) second capacitor as 500 nm light is turned ON/OFF.	75
5.1	Dual-gate like structure consisted of an DNTT-based transistor with a blend-based MIS capacitor on top.	79
5.2	Device structure of DNTT-based MIS capacitor.	81
5.3	Frequency dependence of (a) capacitance and (b) loss ( $G/\omega$ ) of DNTT-based MIS capacitors measured in the dark, in air with different applied gate voltages.	82
5.4	(a) C-V and (b) loss-V plots of a DNTT MIS capacitor measured in the dark in air (black) and in vacuum (red) at 1 kHz.	82
5.5	C-V plots for DNTT-based MIS capacitors (a) under vacuum and (b) in air when in the dark and exposed to 360 nm light.	83
5.6	C-V plots for a DNTT MIS capacitor under 360 nm light exposures showing the effect of voltage scan range.	84
5.7	(a) Capacitance and (b) loss plots obtained in air for different applied AC signal frequencies.	86
5.8	Effect of temperature on (a) C-V and (b) loss-V plots of a DNTT MIS capacitor when measured at 300 Hz in air.	87
5.9	Effect of temperature on (a) C-V and (b) loss-V plots of a DNTT MIS capacitor when measured at 5 kHz in air.	88
5.10	Simulations showing the effect of changing bulk resistance on the (a) C-f and (b) loss-f plots in an ideal MIS capacitor. Semiconductor layer thickness used was 200 nm, $C_i = 400$ pF and $C_b = 600$ pF.	89
5.11	Estimated value of interface trap density as a function of temperature for DNTT-based MIS devices in air in dark.	90
5.12	Effect of long wavelength light, in air, on (a) C-V and (b) loss-V of DNTT MIS capacitors.	91
5.13	Effect of 500 nm light soaking in air on the (a) C-V and (b) loss-V of DNTT MIS capacitors over a period of roughly 7 hours.	92
5.14	Effect of 400 nm light soaking in air on the (a) C-V and (b) loss-V of DNTT MIS capacitors over a period of roughly 2 and a half hours.	93
5.15	(a) C-V and (b) loss-V plots showing partial recovery 15 hours after ceasing the 500 nm light exposure.	94
5.16	Voltage dependence of (a) capacitance and (b) $G/\omega$ of DNTT-based MIS capacitors measured in the dark, in air at 1 kHz	95
5.17	Time evolution of the capacitance (black dots) and conductance (red triangles) in a DNTT capacitor subject to a bias stress of -25 V.	95
5.18	(a) C-V and (b) loss-V plots of DNTT-based MIS capacitors before (black) and after (red) the -25 V stress. The effects of keeping the sample under vacuum for 4 hrs (yellow), 48 hrs (green) and under air exposure of 48 hrs (blue) are shown.	96
5.19	(a) Transfer and (b) output curves of Lisicon/DNTT transistors with a W/L ratio of 40 and channel length of 50 $\mu\text{m}$ immediately after fabrication.	101

5.20	(a) Linear transfer curves of one device in group A #1 in the linear (black) and saturation (red) regimes. (b) Hole mobility of transistors in group A #1 calculated as a function of $V_G$ in the linear (black) and saturation (red) regimes.	101
5.21	(a) Transfer and (b) output curves of Lisicon/DNTT transistors with a W/L ratio of 40 and channel length of 50 $\mu\text{m}$ after 2 and half days of air exposure.	103
5.22	(a) Linear transfer curves of all devices in group A #1 in the linear (black) and saturation (red) regimes. (b) Hole mobility of transistors in group A #1 calculated as a function of $V_G$ in the linear (black) and saturation (red) regimes after 2 and half days of air exposure in the dark.	104
5.23	Mean hole mobility as a function of channel length for devices with (a) same width (2 mm) and (b) same W/L ratio (20).	105
5.24	AFM image of DNTT on top of Lisicon D207-MAK.	105
6.1	P3HT MIS capacitor device structure with illumination through the gate electrode.	110
6.2	Simulated C-V plots using the initial model for different light wavelengths.	114
6.3	Effect of $(E_c - E_{fn})$ value on the simulated C-V curves using the new model. Values used for calculation were $K = 1 \times 10^{10}$ , $N_t = 1 \times 10^{18} \text{ m}^{-3}$ , $(E_c - E_t) = 0.65 \text{ eV}$ .	117
6.4	Effect of $(E_c - E_t)$ on the simulated C-V curves using the new model. Values used for calculation were $K = 1 \times 10^{10}$ , $N_t = 1 \times 10^{18} \text{ m}^{-3}$ , $(E_c - E_{fn}) = 1.5 \text{ eV}$ .	118
6.5	Effect of fine tuning $(E_c - E_t)$ on the simulated C-V curves using the new model. Values used for calculation were $K = 1 \times 10^{10}$ , $N_t = 1 \times 10^{18} \text{ m}^{-3}$ , $(E_c - E_{fn}) = 1.2 \text{ eV}$ .	119
6.6	Effect of K value on the simulated C-V curves using the new model. Values used for calculation were $N_t = 1 \times 10^{18} \text{ m}^{-3}$ , $(E_c - E_t) = 0.65 \text{ eV}$ , $(E_c - E_{fn}) = 1.2 \text{ eV}$ .	120
6.7	Effect of $N_t$ value on the simulated C-V curves using the new model. Values used for calculation were $K = 1 \times 10^{10}$ , $(E_c - E_{fn}) = 1.2 \text{ eV}$ , $(E_c - E_t) = 0.65 \text{ eV}$ .	121
6.8	Experimental and simulated C-V curves for a P3HT MIS capacitor in dark. Values used for calculation were $\epsilon_r = 3.4$ , $CI = 200 \text{ pF}$ , $d_{\text{semi}} = 80 \text{ nm}$ , $K = 0$ , $N_t = 1 \times 10^{18}$ , $E_c - E_{fn} = 1.6$ , $E_c - E_t = 0.65$ .	122
6.9	Experimental and simulated C-V curves for a DNTT MIS capacitor in dark. Values used for calculation were $\epsilon_r = 3$ , $CI = 158 \text{ pF}$ , $d_{\text{semi}} = 80 \text{ nm}$ , $K = 0$ , $N_t = 1 \times 10^{18}$ , $E_c - E_{fn} = 0.01$ , $E_c - E_t = 0.60$ .	123
6.10	Simulated C-V curves for a P3HT MIS capacitor in dark. Values used for calculation were $\epsilon_r = 3.4$ , $CI = 200 \text{ pF}$ , $d_{\text{semi}} = 80 \text{ nm}$ , $K = 0$ , $N_t = 1 \times 10^{18}$ , $E_c - E_{fn} = 1.6$ , $E_c - E_t = 0.65$ .	124

# LIST OF TABLES

<b>3.1</b>	Substrate cleaning procedure.	<b>47</b>
<b>5.1</b>	Channel length and width for the 5 different rows on the PEN substrate. Each group contained nine transistors.	<b>124</b>
<b>6.1</b>	Device parameters and constants used during the simulations.	<b>116</b>

# ABSTRACT

The field of organic electronics has exponentially increased, especially in the last decade, with the discovery of numerous applications. In the first part of this work, the behaviour of poly(3-hexylthiophene):[6,6]-phenyl C<sub>61</sub> butyric acid methyl ester (P3HT:PCBM) blends as active layer of a MIS capacitor was investigated. Electrical characterisation of devices was performed both in the dark and under illumination with light of controlled wavelength. When the device was exposed to light of different wavelengths, minimum capacitance shifts in the capacitance-voltage (C-V) plots were observed. Exposure to near-infrared (NIR) light also shifted the minimum capacitance, which was investigated with the use of different LUMO level PCBM-like molecules. The NIR response was likely to be related to the HOMO of P3HT and LUMO of PCBM energy difference. The device quickly recovered after light exposure and only a small anticlockwise hysteresis was observed (less than 0.5 V), indicating that a small quantity of electrons remained trapped at the semiconductor/insulator interface. A charge-injection-device with the blend as the active layer was also fabricated, however, electron transfer was not observed.

The response of dinaphtho[2,3-b:2',3'-f]thieno[3,2-b]thiophene (DNTT)-based MIS capacitors and thin film transistors under different ambient conditions was also investigated. Analysing the C-V plots of DNTT MIS capacitors when exposed to light, bias stress, periods of vacuum and measurement frequency lead to the conclusion that exposure to air is needed in order to trigger light-related processes in the semiconducting layer. These processes however, tend to follow DNTT's absorption profile. A comparable feature was observed in the DNTT thin film transistors, where transistors characteristics significantly improved after 2.5 days of air exposure. Hole mobility, calculated both in the linear and saturation regimes, improved to  $\sim 0.3 \text{ cm}^2/\text{Vs}$  after the period of air exposure.

A theoretical model that describes the features observed in the C-V plots of MIS capacitors was developed. In order to account for limited anticlockwise hysteresis, electron capture and emission rate from traps, described using Shockley-Read-Hall statistics, was introduced. The model correctly predicts the behaviour of MIS capacitors where electron trapping at the semiconductor/interface is not prominent.

# ACKNOWLEDGEMENTS

First of all, I would like to thank God.

Many thanks to my supervisor Professor David Martin Taylor, who kept me motivated throughout this time and whose insights and advices were substantial to the development of this thesis. His aid was not limited to work hours but also extended afterwards, where he and his wife helped me view Bangor as a new home.

Thanks to Colin, Eifion, Melanie, Nor, Professor Jeff Kettle and especially to Dr Paul Sayers, for all the patience and help during my adaptation period.

Many thanks to Merck Chemicals Ltd., especially to Dr Lichun Chen, for all the financial support, materials provided, and discussions had. All the seminars and presentations held at Merck help me grew as a person during these years.

I would like to deeply thank my family and especially my wife Talita, who always supported me, even when we were going through dark times. Her love and kind words made this thesis become true.

# CHAPTER 1

## INTRODUCTION

The idea of conducting and controlling electrical current in plastics took a sharp turn in the 1970s when the concept of doping was introduced to organic semiconductors. Although several materials were being investigated<sup>1</sup>, it was the polyacetylene polymer that claimed the honour to be the “first” conductive plastic<sup>2</sup>. The work of Alan J. Heeger, Alan G. MacDiarmid and Hideki Shirakawa was later awarded with the Nobel Prize for Chemistry in 2000 “*for the discovery and development of electrically conductive polymers*”<sup>3</sup>. Nowadays, conductive organic materials can vary from small molecules that exhibit band-like conduction to complex polymers, where electrical conduction relies on hopping, and fullerene-based materials.

Forty years later and the field of organic electronics has exponentially increased, especially in the last decade, with the discovery of numerous applications. To name a few, organic semiconductors can be used as the active layer in thin-film transistors<sup>4-7</sup>, which can be integrated into electronic circuits<sup>8-13</sup>; photovoltaic cells<sup>14-16</sup>; photodetectors<sup>17-19</sup>; OLED displays<sup>20-22</sup> and in RFID tags<sup>23,24</sup>. In contrast to standard silicon-based electronics, organic semiconductors can be applied easily to flexible substrates with low-cost fabrication techniques such as spin-coating and roll-to-roll printing (R2R)<sup>8,9,25</sup>, and can be implemented in smart wearable textiles and devices<sup>21,26-</sup>

The wide range of applications of organic semiconductors has also attracted major companies, such as Merck Chemicals Ltd., Samsung, LG, Sony, AU Optronics and others, to invest in the emerging market of organic-based technology. The organic electronics market is expected to grow to US\$ 79.6 billion by 2020 with a major portion of it going to displays based on organic materials<sup>29</sup>. However, to be able to reach this projected bright future, organic materials have to provide advantages over the already established silicon industry.

It is not by chance that silicon has dominated the electronics industry. It is one of the most abundant elements on earth and, when purified and in crystalline form, has excellent electrical conduction and absorption of visible light. With a high relative dielectric constant, excitons created through light absorption are readily dissociated into free charge carriers. Although expensive, the processes of purifying and doping are already well known and developed. On the other hand, standard silicon devices are usually thick ( $\sim \mu\text{m}$ ) and hard to be integrated in flexible devices.

As already mentioned, organic materials are easily applied to flexible substrates using solution-based techniques like spin-coating and R2R, making this a key advantage over inorganic devices. Due to the wide variety of organic compounds, tunability becomes a factor to consider, once one control the electronic properties by controlling the attached side chains on a polymer for example. However, due to the small relative dielectric constants of organic semiconductors, excitons created through light absorption must first be dissociated with additional help (e.g. at interfaces or in externally applied electrical fields) in order to produce free charge carriers. Device durability is also a problem to be tackled, since most organic compounds are prone to oxidation, light and thermal degradation, hindering device performance over time.

This work described in this thesis was undertaken with the aim to better understand the processes behind light induced charge creation and its impact on device performance on two different types of organic compounds: the well-known polymer:fullerene blend of P3HT:PCBM, widely studied in photovoltaic devices; and DNNT, a small molecule with great durability and transistor performance. For such a

---

task, a relatively simple device structure was chosen to be the target of analysis: an organic-based Metal-Insulator-Semiconductor (MIS) capacitor. By controlling the applied gate voltage, one can control the charge population within the semiconductor and probe the semiconductor-insulator interface by analysing its small-signal admittance response.

Chapter 2 reviews the relevant literature covering the fundamental aspects of organic semiconductors and MIS device operation. Attention is given to the analysis of admittance curves and frequency measurements, which can provide valuable information on the characteristics of the semiconductor-insulator interface. The last section describes the recent use of organic semiconductors in MIS capacitors and the key findings behind it.

In Chapter 3, a brief review is provided of the materials and fabrication techniques used throughout this thesis. Chapter 4 investigates the photo-electrical behaviour of poly(3-hexylthiophene): [6,6]-phenyl C<sub>61</sub> butyric acid methyl ester (P3HT:PCBM) through admittance measurements in MIS capacitors. The absorption of long wavelengths, near infrared, is also discussed. A charge-injection-device was fabricated and analysed through current-time experiments with and without light exposure.

Chapter 5 discusses the experimental results obtained under different ambient conditions from a MIS capacitor incorporating the small molecule dinaphtho[2,3-b:2',3-f]thieno[3,2-b]thiophene (DNTT). Later, DNTT was used with Lisicon D207-MAK, an insulator provided by Merck Chemicals Ltd., to test the reliability of the semiconductor-insulator pair in an array of 90 transistors. Transistor characteristics were analysed immediately after device fabrication and after two and a half days of air exposure in the dark.

Chapter 6 discusses the results obtained from an improved mathematical model of photocapacitance in organic MIS capacitors in which electron trapping at the semiconductor/insulator interface is better described. Firstly, the original model is

presented and its validity is discussed. Then, as a solution to better represent a more general behaviour, the idea of electron capture, emission and recombination rates are introduced into the model.

Finally in Chapter 7, the conclusions of the various strands of work are brought together and suggestions made for further work.

## REFERENCES

- 1 D. Jérôme, A. Mazaud, M. Ribault, and K. Bechgaard, *J. Physique Lett.* **41**, 95 (1980).
- 2 H. Shirakawa, E. J. Louis, A. G. MacDiarmid, C. K. Chiang, and A. J. Heeger, *Journal of the Chemical Society, Chemical Communications*, 578 (1977).
- 3 *Nobelprize.org*, (2000).
- 4 N. K. Za'aba, J. J. Morrison, and D. M. Taylor, *Organic Electronics* **45**, 174 (2017).
- 5 M. da Silva Ozório, G. L. Nogueira, R. M. Morais, C. da Silva Martin, C. J. L. Constantino, and N. Alves, *Thin Solid Films* **608**, 97 (2016).
- 6 G. A. Abbas, Z. Ding, H. E. Assender, J. J. Morrison, S. G. Yeates, E. R. Patchett, and D. M. Taylor, *Organic Electronics* **15**, 1998 (2014).
- 7 D. Ji, L. Jiang, X. Cai, H. Dong, Q. Meng, G. Tian, D. Wu, J. Li, and W. Hu, *Organic Electronics* **14**, 2528 (2013).
- 8 E. R. Patchett, A. Williams, Z. Ding, G. Abbas, H. E. Assender, J. J. Morrison, S. G. Yeates, and D. M. Taylor, *Organic Electronics* **15**, 1493 (2014).
- 9 D. M. Taylor, E. R. Patchett, A. Williams, N. J. Neto, Z. Ding, H. E. Assender, J. J. Morrison, and S. G. Yeates, *Electron Devices, IEEE Transactions on* **61**, 2950 (2014).
- 10 S. D. Ogier, H. Matsui, L. Feng, M. Simms, M. Mashayekhi, J. Carrabina, L. Terés, and S. Tokito, *Organic Electronics* **54**, 40 (2018).
- 11 S. Masaya Kondo and Takafumi Uemura and Takafumi Matsumoto and Teppei Araki and Shusuke Yoshimoto and Tsuyoshi, *Applied Physics Express* **9**, 061602 (2016).
- 12 J. Roh, H. Roh, H. Shin, H. Kim, and C. Lee, *Polymer Bulletin* **73**, 2531 (2016).
- 13 P. Watson Colin, A. Brown Beverley, J. Carter, J. Morgan, and D. M. Taylor, *Advanced Electronic Materials* **2**, 1500322 (2016).
- 14 Z. Fei, D. Eisner Flurin, X. Jiao, M. Azzouzi, A. Röhr Jason, Y. Han, M. Shahid, S. R. Chesman Anthony, D. Easton Christopher, R. McNeill Christopher, D. Anthopoulos Thomas, J. Nelson, and M. Heeney, *Advanced Materials* **30**, 1705209 (2018).
- 15 C. Sun, F. Pan, H. Bin, J. Zhang, L. Xue, B. Qiu, Z. Wei, Z.-G. Zhang, and Y. Li, *Nature Communications* **9**, 743 (2018).
- 16 X. Xu, Z. Li, W. Zhang, X. Meng, X. Zou, D. Di Carlo Rasi, W. Ma, A. Yartsev, R. Andersson Mats, A. J. Janssen René, and E. Wang, *Advanced Energy Materials* **8**, 1700908 (2017).
- 17 Y. Liu, Z. Yang, and S. Liu, *Advanced Science* **5**, 1700471 (2017).
- 18 F. Zhao, K. Xu, X. Luo, Y. Liang, Y. Peng, and F. Lu, *Advanced Optical Materials* **6**, 1700509 (2017).
- 19 J. Zhou and J. Huang, *Advanced Science* **5**, 1700256 (2017).
- 20 H.-W. Chen, J.-H. Lee, B.-Y. Lin, S. Chen, and S.-T. Wu, *Light: Science & Applications* **7**, 17168 (2018).
- 21 S. Kwon, H. Kim, S. Choi, E. G. Jeong, D. Kim, S. Lee, H. S. Lee, Y. C. Seo, and K. C. Choi, *Nano Letters* **18**, 347 (2018).
- 22 X. Yang, X. Zhang, J. Deng, Z. Chu, Q. Jiang, J. Meng, P. Wang, L. Zhang, Z. Yin, and J. You, *Nature Communications* **9**, 570 (2018).
- 23 A. Falco, F. J. Salmerón, C. F. Loghin, P. Lugli, and A. Rivadeneyra, *Sensors* **17** (2017).

- <sup>24</sup> V. Fiore, P. Battiato, S. Abdinia, S. Jacobs, I. Chartier, R. Coppard, G. Klink, E. Cantatore, E. Ragonese, and G. Palmisano, *IEEE Transactions on Circuits and Systems I: Regular Papers* **62**, 1668 (2015).
- <sup>25</sup> J. A. Avila-Niño, E. R. Patchett, D. M. Taylor, H. E. Assender, S. G. Yeates, Z. Ding, and J. J. Morrison, *Organic Electronics* **31**, 77 (2016).
- <sup>26</sup> K. Bansal Ashu, S. Hou, O. Kulyk, M. Bowman Eric, and D. W. Samuel Ifor, *Advanced Materials* **27**, 7638 (2014).
- <sup>27</sup> R. Fan Feng, W. Tang, and L. Wang Zhong, *Advanced Materials* **28**, 4283 (2016).
- <sup>28</sup> T. Yokota, P. Zalar, M. Kaltenbrunner, H. Jinno, N. Matsuhisa, H. Kitanosako, Y. Tachibana, W. Yukita, M. Koizumi, and T. Someya, *Science Advances* **2** (2016).
- <sup>29</sup> *Organic Electronics Market by Applications (Display, ORFID, OLED Lighting, Photovoltaic, System Components) - Global Opportunity Analysis and Industry Forecast, 2013 - 2020* (2014). Accessed July 2018

# CHAPTER 2

## BACKGROUND CONCEPTS AND LITERATURE REVIEW

### 2.1 Introduction

In this chapter, the fundamental aspects of organic semiconductors and devices are explained. The concepts of hybridization needed to understand the semiconducting character of organic compounds are discussed first, together with the formation of molecular orbitals. Notions of light interaction, charge transport and excitations are also mentioned. Later, the operation of metal-insulator-semiconductor (MIS) capacitors is explained. The last section discusses briefly the literature on organic-based MIS capacitors.

## 2.2 Background to Organic Semiconductors

### 2.2.1 Hybridization & Molecular Orbitals

The electronic properties of materials are mainly associated with the characteristics of the outer electrons. In the case of carbon,  $^{12}_6\text{C}$ , its six electrons are energetically distributed in the following atomic orbitals:  $1s^2 2s^2 2p_x^1 2p_y^1 2p_z^0$ . The kind of bond made by carbon with other elements is covalent, in which electrons are shared between the different atoms.

To bind with another element and then form a molecule, these atomic orbitals go through a process called hybridization, in which the electrons are `rearranged` into new orbitals. This process can be understood as a promotion of an electron from the  $2s$  level to a new hybrid orbital formed by the orbitals  $s$  and  $p$ , namely  $sp$  orbitals. Of the three different  $sp$  hybrid orbitals ( $sp$ ,  $sp^2$  and  $sp^3$ ; Figure 2.1), the one that gives the compound a semiconductor character is the  $sp^2$ , shown in Figure 2.1b. In this case, three  $sp^2$  orbitals are formed and are separated by an angle of  $120^\circ$ , while the conserved  $p_z$  orbital remains perpendicular to the plane formed by the hybrid orbitals.

The three  $sp^2$  orbitals can overlap to a high degree with other atoms making a strong  $\sigma$  bond, which requires considerable energy to break, keeping the molecule stable. On the other hand, the remaining  $p_z$  orbital overlaps to a lesser degree with its neighbouring atoms making a less energetic double bond, namely a  $\pi$  bond<sup>1</sup>.

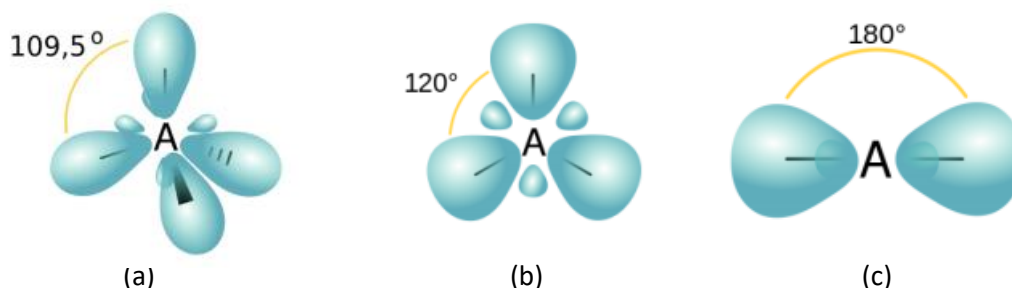


**Figure 2.1 – The three hybridization orbital configurations (a)  $sp^3$  (b)  $sp^2$  (c)  $sp$ . Adapted from <sup>2</sup>.**

When already hybridized carbon atoms bind together, the atomic orbitals can overlap each other. In the case of the benzene molecule ( $C_6H_{12}$ ), the three  $sp^2$  orbitals of one carbon makes a  $\sigma$  bond with the two neighbouring carbons and one hydrogen atom. The superposition of the remaining  $p_z$  orbitals of all carbon atoms forms the  $\pi$  double bond. Due to the weaker interaction between these last orbitals, those electrons cannot be tied to a specific carbon atom, giving rise to a delocalized electron cloud that spans the whole molecule (Figure 2.2).

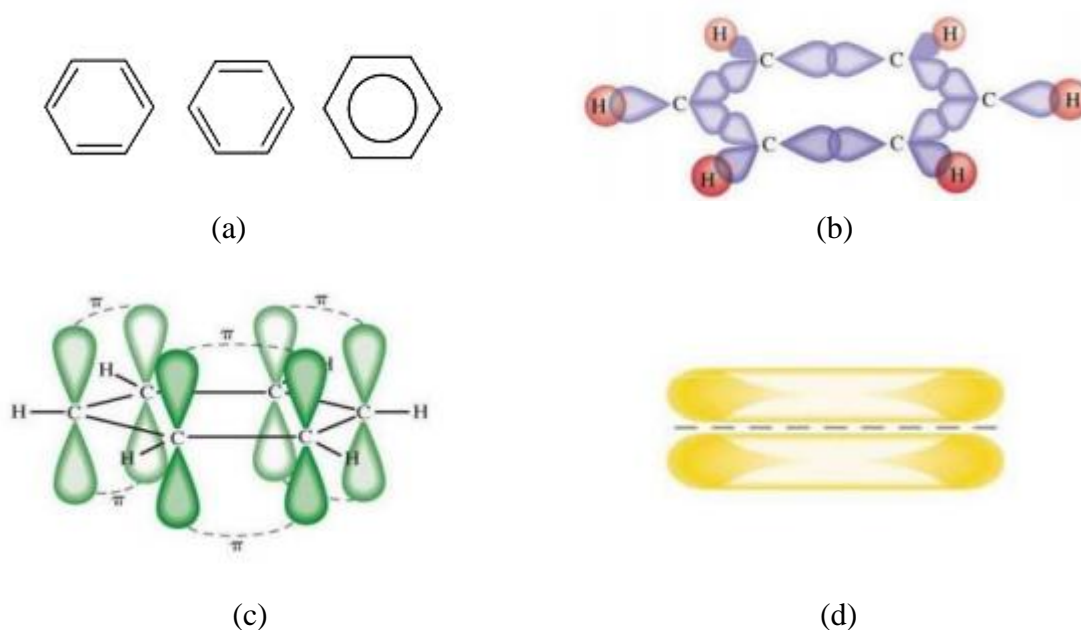


**Figure 2.2 - (a) Chemical representations of benzene. (b)  $\sigma$  bonds and (c)  $\pi$  bonds. (d) Result of the superposition of  $\pi$  orbitals. The dashed line represents the plane formed by the carbon atoms.**

**Adapted from <sup>3</sup>.**

Due to the coupling of the binding electrons, their energy levels split into bonding ( $\sigma$ ,  $\pi$ ) and antibonding ( $\sigma^*$ ,  $\pi^*$ ) states, giving rise to a band gap. Since the  $\sigma$  bonds have a higher degree of overlapping than the  $\pi$  bond, the energy required to excite one electron from a  $\pi$  state to a  $\pi^*$  state is much less than the analogous transition  $\sigma$ - $\sigma^*$ . A visual representation of these transition energies for one molecule is given in Figure 2.3. As the molecules stack and are held by van der Waals forces to become a solid,

more molecular orbitals come into play, giving rise to new bonding and antibonding energy levels.

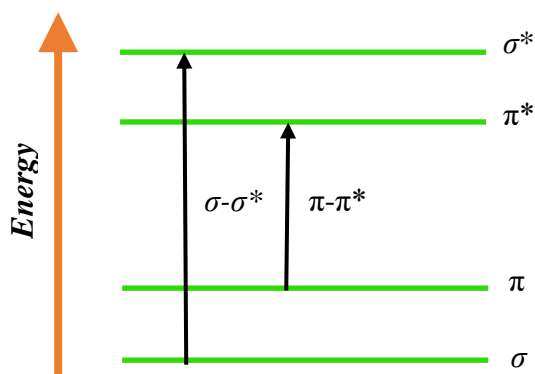


**Figure 2.3 – Energy diagram scheme of  $\pi\text{-}\pi^*$  and  $\sigma\text{-}\sigma^*$  transitions.**

In a perfect scenario, where molecules stack regularly, no impurities are present, trap sites are non-existent and the usual disorder of organic materials is neglected, there will be a continuous distribution of energy levels that will “condense” into bands. The energy gap is then defined by the energetic difference between the top of the valence band and the bottom of the conduction band. However, as we move to a more realistic view, organic compounds and their energy levels will be affected by impurities, trap-sites and, probably the most important feature, disorder. Such is the case that these drawbacks impact heavily on their photoelectric properties, making it almost impossible for organic semiconductors to compete with inorganic semiconductors when pristine purity and extremely high efficiency are required.

Due to the molecular character of most organic solids, the energy gap between the excited states and the ground states are better represented by the idea of specific molecular orbital energies. Then, the top of the valence band in an inorganic semiconductor is replaced with the Highest Occupied Molecular Orbital (HOMO) and the bottom of the conduction band with the Lowest Unoccupied Molecular Orbital (LUMO). It is important to notice that these energies, for a specific molecule, are

sensitive to a variety of aspects: planarization, length of the conjugation segment, doping density, molecule stacking, molecule-molecule interactions, fabrication procedures<sup>1,4-6</sup> to name but a few.

## 2.2.2 Light Absorption

In the ground state, all bonding molecular orbitals up to the HOMO are filled with two electrons with opposite spin directions, while all antibonding molecular orbitals from the LUMO to higher energies are empty. Photon-induced transitions can occur between these different energy levels, and optical measurements constitute an important means of determining the energy level structure of both organic and inorganic semiconductors<sup>7</sup>. The energy gap for conjugated molecules is typically 2 - 3 eV, making them good absorbers/emitters of visible light. The complex refractive index characterizes the optical properties of semiconductors,

$$\bar{n} = n_r - ik_e \quad (2.1)$$

where the real part  $n_r$  is related to the propagation velocity of light in the medium ( $v$ ) and the velocity of light in vacuum ( $c$ ) through:

$$n_r = \frac{c}{v} \quad (2.2)$$

and the imaginary part  $k_e$ , called the extinction coefficient, determines the absorption coefficient  $\alpha$  for a particular wavelength  $\lambda$ , through<sup>7</sup>:

$$\alpha(\lambda) = \frac{4\pi k_e}{\lambda} . \quad (2.3)$$

When a photon with energy  $E = h\nu$  ( $h$  being Planck's constant and  $\nu$  the frequency of the light) greater than the LUMO-HOMO energy difference strikes the solid, an electron can be excited to a higher energy level and participate in other

processes. As photons are absorbed by the material, the light intensity  $I(x)$  at a depth  $x$  in the semiconductor will diminish as described by the Beer-Lambert Law:

$$I(x) = I_0 e^{-\alpha(\lambda)x} \quad (2.4)$$

with  $I_0$  being the initial intensity. Typically, the absorption coefficients of organic semiconductors are in the order of  $10^5 \text{ cm}^{-1}$ , meaning that a 100 nm thick layer is enough to make sure that a large fraction of incident photons are absorbed throughout the material.

Unlike inorganic semiconductors, where light absorption leads almost directly to free charge carriers, the low relative dielectric constant of organic semiconductors ( $\epsilon \approx 2 - 4$ ) makes the Coulomb attraction between the excited electron and its vacancy, the created hole, strong enough to make them bind, forming a neutral excited state named an exciton which distorts the molecular structure. In inorganic materials, the dielectric constant is high enough to shield the excited electron from the hole, leading to spontaneous dissociation of the exciton into free e/h (electron-hole) pairs<sup>8</sup>. Due to the relatively large exciton binding energy in organic semiconductor, a few hundreds of meV, a non-negligible potential barrier arises and, in order to yield free charge carriers, additional force is required to overcome the exciton binding energy. One can reduce it with an applied external electric field, as in a MIS capacitor<sup>9,10</sup>, or can make use of the different electron affinities of donor and acceptor compounds, as in a heterojunction solar cell<sup>11,12</sup>, both methods dissociating the exciton.

However, while photon absorption and exciton dissociation are happening, a number of processes compete against the formation of free carriers which results in exciton quenching. The exciton diffusion length is approximately 10 nm<sup>13</sup>, therefore only photons absorbed near a dissociating region will yield free e/h pairs. These exciton-quenching processes hinder the overall efficiency of photoelectronic devices, leading to charge losses throughout the semiconductor that can be observed as smaller than expected current and voltage output.

### 2.2.3 Charge Transport

“It may seem odd to write an article entitled ‘charge transport in organic semiconductors’ when these materials are inherently insulators”<sup>1</sup>. This quote from Bäessler and Köhler describes how much of a challenge it is to conduct electrical charges in organic materials, yet it is possible. Following the conductivity equation,  $\sigma = n\mu q$ , where  $n$  and  $\mu$  are the density and mobility of the free charge carrier respectively, and  $q$  the elementary charge, one must provide the organic material with free charge carriers externally, either by injection from metal electrodes or by light excitation, in order to produce an electrical current. Due to the relatively large band gaps of organic semiconductors, 2 – 3 eV, thermal generation of free carriers in organic semiconductors is almost non-existent<sup>14,15</sup>.

After light absorption and successful exciton dissociation, photo-generated electrons and holes are free to contribute to device current. As discussed above, organic molecules are held together by weak van der Waals forces and, although some organic crystals can stack highly in order to exhibit band-like structures at room temperature<sup>16-20</sup>, most organic solids, especially polymers, have a spatial and energetic disordered character. Due to this disorder, the transport of charges through organic semiconductors follows a phonon-assisted hopping mechanism<sup>8</sup>, as illustrated in Figure 2.4.

The electric field drives the charges to the collection terminals, but to be able to move through the active layer, these charges will have to gain/lose energy and hop between localized molecular states. The availability of these states is intrinsically related to the molecular configuration of the solid, therefore, highly packed systems, as in evaporated small molecules<sup>16,21-24</sup>, tend to have a higher charge carrier mobility when compared to solution processed polymers<sup>25</sup>.

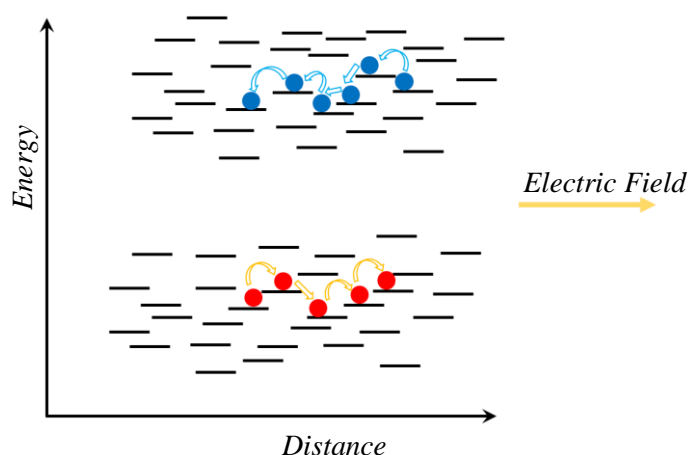


**Figure 2.4 – Hopping mechanism representing holes (red) and electrons (blue) transport when an electric field (yellow arrow) is applied.**

As mentioned in Section 2.2.1, since the semiconductor character arises from the  $sp^2$  hybridization, organic semiconductors are inclined to display anisotropic charge mobilities, with good transport through the conjugated segment and very poor charge conduction elsewhere<sup>26</sup>. The conduction also depends largely on the quality of the sample, since impurity-induced trap sites play an important role in charge transport<sup>1,4</sup>.

The charge carrier mobility ( $\mu$ ) is the parameter commonly used to characterize the performance of electronic devices, such as transistors. Typically, crystalline silicon can achieve extremely high mobilities in the order of  $\sim 10^3$   $\text{cm}^2/\text{Vs}$ <sup>[7]</sup> and hydrogenated amorphous silicon (a-Si:H) in the range of  $\sim 1$   $\text{cm}^2/\text{Vs}$ . In the past, organic-based field effect transistors showed a charge mobility  $\mu$  in the order of  $10^{-3}$   $\text{cm}^2/\text{Vs}$ <sup>[27]</sup>, though organic electronic devices are improving every year, with transistors achieving mobilities in the  $10^0$ - $10^1$   $\text{cm}^2/\text{Vs}$  range<sup>21,22,27-29</sup>.

Organic-based transistors often rely on the standard metal-oxide-semiconductor field effect transistor (MOSFET) model to calculate the charge carrier mobility through the  $I$ - $V$  curve. This, however can lead to inaccuracies when used to analyse non-ideal transistors. Bittle *et al*<sup>29</sup> analysed several papers where the drain current  $I_D$  displayed an abrupt change in slope with respect to  $V_{GS}$ , the gate-source voltage, whereas it should

remain constant. This non-ideal behaviour can lead to different values, close to one order of magnitude difference, in the calculated mobility when using different slopes.

## 2.3 Metal-Insulator-Semiconductor Capacitor

The semiconductor industry is probably the largest industry in the world and is widely recognized as a key driver for economic growth and technology enhancement<sup>30</sup>. This was only possible with the understanding of how semiconductors work. In the mid-20th century, the growth of semiconductor physics exploded and led to the development of key electronic devices, such as transistors, used in every smartphone and medical device nowadays.

One of the more basic devices created at that time was the Metal-Insulator-Semiconductor (MIS) capacitor (Figure 2.5), which consists of a metal electrode, known as gate, an insulating layer, a semiconductor and a metal ohmic contact on top for electrical connectivity. It was first proposed as a voltage-controlled variable capacitor in 1959<sup>7</sup>. Since the gate voltage can control the charge population within the semiconductor, it is widely used as a tool to probe the semiconductor/insulator interface.

In this section, using standard crystalline silicon semiconductor as a guide, ideal MIS capacitor regimes will be discussed first, and then the discussion of more realistic cases containing interface states, lateral conduction and trap sites will take place.

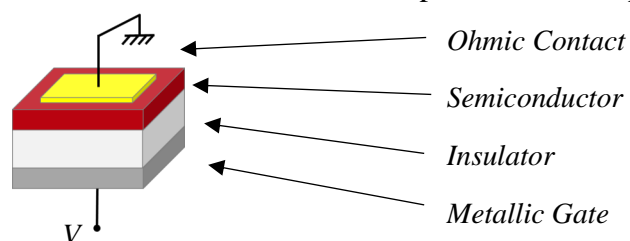


**Figure 2.5 – Schematic view of a MIS capacitor.**

### 2.3.1 Ideal MIS Capacitor

As mentioned above, the gate voltage modulates the population of charges inside the semiconductor, which then changes the overall capacitance of the device. These changes can be described more easily with the help of band diagrams and equivalent circuits. In an ideal case, the semiconductor and the dielectric are free of any defects and unwanted impurities, permanent polarization mechanisms, interface states, lateral conduction and any other effect/entity that may hinder the flow of charge carriers throughout the operation of the device. The top electrode forms an ohmic contact with the semiconductor while an infinite resistance for the insulator is assumed, creating a large energy barrier between the metal gate and the semiconductor.

For an intrinsic semiconductor, where no charges are induced by dopants, the intrinsic Fermi level ( $E_I$ ) lies at the centre of the band gap ( $E_G$ ), as in Fig. 2.6. Depending on the doping profile, the semiconductor Fermi level ( $E_{FS}$ ) can move closer to the conduction band edge  $E_C$  (n-type) or closer to the valence band edge  $E_V$  (p-type). In the following analysis, a p-type semiconductor with same work function as the metal will be used as an example, but the explanation is analogous for an n-type semiconductor.

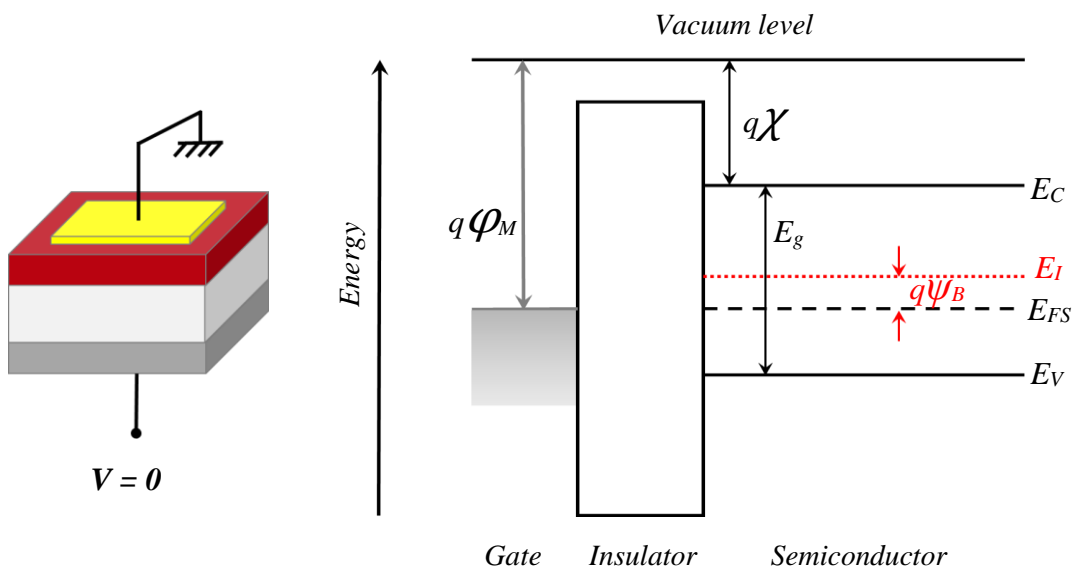


**Figure 2.6 – Flatband condition.  $\chi$  is the electron affinity of the semiconductor.**

Depending on the applied gate bias, four different regimes can be distinguished: flatband, accumulation, depletion and inversion<sup>7,31</sup>. In thermal equilibrium, when there is no applied voltage at the gate ( $V = 0$ ), no electric field is induced in the semiconductor, thus the energy bands remain *flat*, as in Figure 2.6, and the net space charge in the region is zero. In this case,  $\psi_B$ , the bulk potential, remains the same throughout the semiconductor.

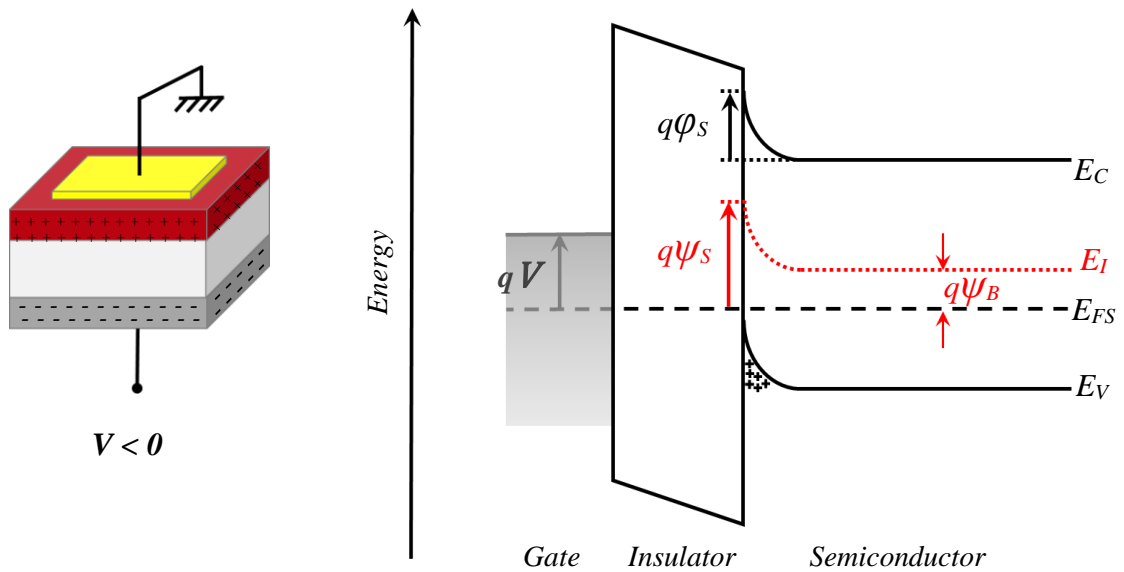


**Figure 2.7 – Accumulation case.**

When a negative voltage is applied at the metal gate ( $V < 0$ ), an electric field is induced within the semiconductor drawing the positive charge carriers (holes) to the semiconductor/insulator interface, creating an *accumulation* layer of majority carriers. This will make the energy bands bend upwards, bringing the valence band edge  $E_V$  closer to the Fermi level  $E_{FS}$ , as in Figure 2.7. As the voltage increases to more negative values, the population of holes increases and also the band bending. The carrier density depends exponentially on the energy difference between  $E_{FS}$  and  $E_V$  and, in the ideal case, no current flows in the structure, therefore the Fermi level  $E_{FS}$  remains flat<sup>7</sup>, the system is in thermal equilibrium. The total band bending is described by  $\phi_s$ , which is the surface potential with respect to the bulk potential  $\psi_B$ .

As the applied bias moves from negative to positive ( $V > 0$ ), the accumulated holes are pushed away from the interface, creating a region free of majority carriers, called a *depletion* region. If the semiconductor is p-doped, the fixed ionized acceptor atoms remain, giving rise to a negative space charge region causing the semiconductor bands to bend downwards (Figure 2.8). As the voltage increases, the width  $w$  of the depletion region increases until it expands through the whole semiconductor, or inversion sets in.

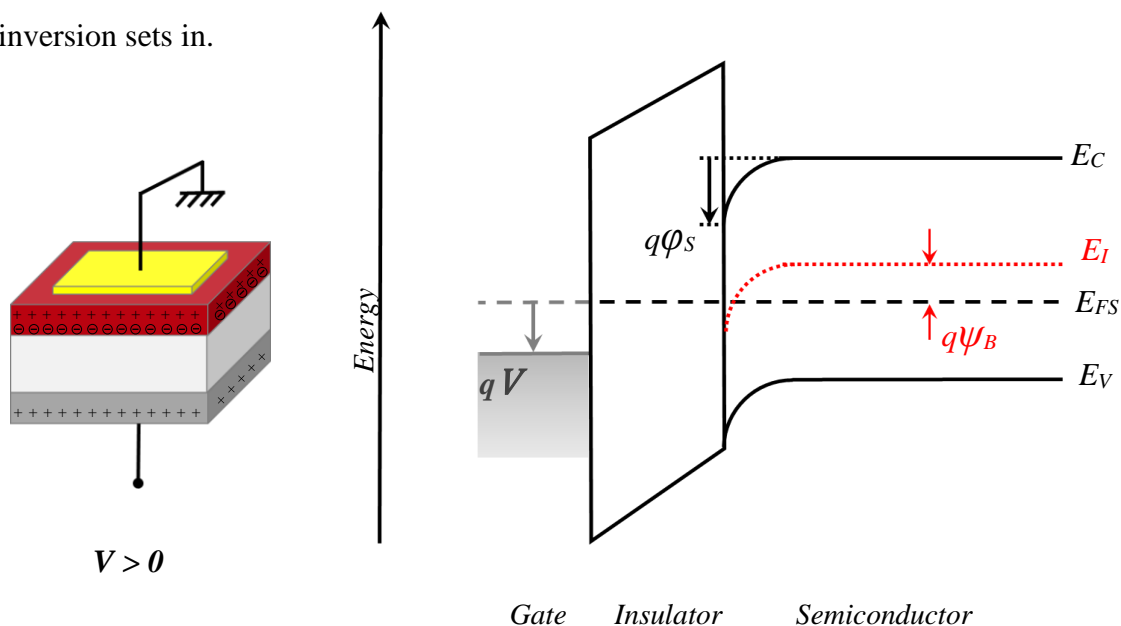


**Figure 2.8 – Depletion case.**

In standard silicon devices, inversion occurs when the gate voltage increases to such high positive values that band bending causes the intrinsic Fermi level  $E_i$  to cross  $E_{FS}$ . In this case, thermal generation of electrons increases and they are drawn to the semiconductor/insulator interface, creating an accumulation of minority carriers known as an *inversion* layer. Now, the depletion region no longer expands and every change in negative charge will occur in the inversion layer, rather than by exposure of more ionised acceptors. This is not commonly observed in organic semiconductors, due to their wide band gap<sup>9</sup>. Hence, the depletion region continues to expand with increasing voltage until full depletion (known as *deep depletion*) occurs or the gate dielectric breaks down.

The depletion region thickness  $w$ , which will be used as a factor for an indirect measure of the semiconductor thickness throughout the thesis, can be calculated without much difficulty. In the absence of any work-function difference between the top contact and the semiconductor, the applied gate voltage  $V$  will partly appear across the insulator,  $V_I$ , and partly across the semiconductor. Thus:

$$V = V_I + \psi_S . \quad (2.5)$$

The potential across the insulator is given by:

$$V_I = \xi_I d = \frac{|Q_S|d}{\epsilon_I} = \frac{|Q_S|}{C_I} \quad (2.6)$$

where  $d$  is the insulator thickness,  $\xi_I$  is the electric field in the insulator,  $Q_S$  is the charge per unit area in the electrode,  $\epsilon_I$  represents the dielectric constant of the insulator, while  $C_I$  represents the insulator capacitance per unit area. Assuming the depletion approximation is valid, in which the charge density transition between the depletion region edge and the bulk of the semiconductor follows a box function, one can calculate the charge in the depletion region as<sup>7</sup>:

$$Q_S = -qN_A w \quad (2.7)$$

where  $N_A$  is the semiconductor doping density.

From this, the potential  $\psi_S$  across the depletion region may be deduced from Poisson's equation and expressed as:

$$\psi_S = \frac{qN_A w^2}{2\epsilon_S} \quad (2.8)$$

where  $\epsilon_S$  is the dielectric constant of the semiconductor. Using the above relations, the thickness of the depletion region can be deduced, i.e.:

$$w = \sqrt{\frac{\epsilon_S^2}{C_I^2} + \frac{2\epsilon_S V}{qN_A} - \frac{\epsilon_S}{C_I}} \quad (2.9)$$

Once  $w$  is known, the capacitance of the depletion region can be deduced.

### 2.3.2 Admittance of MIS Capacitors

The changes in the population of holes/electrons at the semiconductor can be seen as changes in the capacitance-voltage ( $C$ - $V$ ) response of a MIS capacitor. The admittance  $Y$ , the inverse of the impedance  $Z$ , is a measure of how easily current flows through the device, and can be expressed as:

$$Y \equiv \frac{1}{Z} = G + jB = G + j\omega C \quad (2.10)$$

where  $G$  is the conductance,  $B$  the susceptance,  $j$  the imaginary number  $\sqrt{-1}$ ,  $\omega$  the angular frequency, and  $C$  the capacitance. When performing a  $C$ - $V$  measurement on a standard silicon MIS capacitor, the four different regimes (accumulation, depletion, deep depletion and inversion) can be observed. In order to do so, a small AC signal is superimposed on the DC gate voltage. The charge carriers will start moving forward and backwards as they try to follow the potential variations. At low frequencies, the carriers are able to follow the AC signal and inversion can be observed, as in the blue line in Figure 2.9.

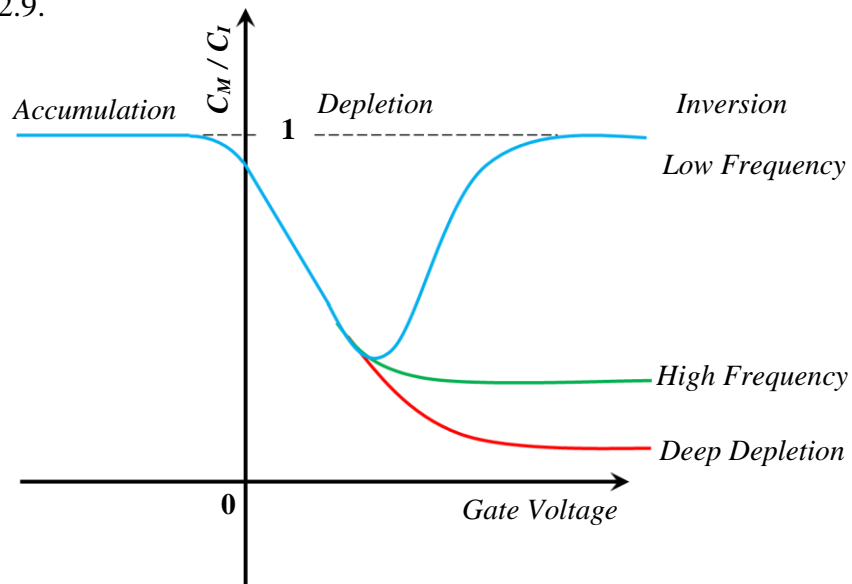


**Figure 2.9 – Capacitance-Voltage profile of an ideal inorganic MIS device based on a p-type semiconductor.**

However, if the frequency is high, electron generation/recombination processes cannot respond quickly enough to the potential fluctuations. In this case, the minority carriers only respond to slow changes in the DC voltage (green line). At high frequencies with a fast gate-voltage sweep rate in the positive direction, the minority electrons do not have enough time to come to equilibrium even with the large-signal variation<sup>7</sup>, making the depletion region grow until it fills the whole semiconductor, known as *deep depletion*, red line in Figure 2.9.

The ability of the electron concentration to follow the applied AC signal, therefore, determines the measured capacitance. At low frequencies an inversion layer of minority carriers is formed and can be observed, increasing the measured capacitance back to the insulator geometrical capacitance. Otherwise, depending on the voltage sweep rate, the inversion layer cannot be observed or is not created at all. In the latter case, the depletion region will expand until it spans the whole semiconductor, so that  $w = d_s$ .

To better understand the  $C$ - $V$  curve of a MIS device, one can model it as a capacitive element, as it was originally conceived. While in accumulation, the MIS device works as a two-plate capacitor, with the semiconductor acting as the top metal plate. As the gate voltage goes to more negative values, the concentration of holes at the semiconductor/insulator interface increases following:

$$C = \frac{Q}{V} \quad (2.11)$$

and the measured capacitance per unit area  $C_M$  is then determined by the geometrical capacitance of the insulator itself:

$$C_M \approx C_I = \frac{\epsilon_I}{d}. \quad (2.12)$$

As the voltage switches to positive, holes are pushed away from the interface and the depletion region starts forming. When performing the  $C$ - $V$  measurement, the depletion region acts as a capacitive element ( $C_D$ ) in series with the insulator

capacitance, so that the measured capacitance decreases as the depletion thickness  $w$  increases:

$$\frac{1}{c_M} = \frac{1}{c_I} + \frac{1}{c_D} \quad (2.13)$$

where

$$C_D = \frac{\epsilon_S}{w} . \quad (2.14)$$

If inversion occurs, then at low frequency electrons accumulated at the semiconductor/insulator respond to the small-signal voltage and bring the capacitance back to the geometrical capacitance of the insulator. At high frequency, minority electrons in the inversion cannot follow the small-signal. If the voltage sweep rate is sufficiently low for inversion charge to follow the applied gate voltage, then the capacitance will remain at the value corresponding to the onset of inversion – at this point the depletion region does not expand further. If inversion does not set in, the depletion region continues to expand and the capacitance fall until it reaches a new minimum plateau corresponding to full depletion of the semiconductor.

For the inorganic metal-SiO<sub>2</sub>-Si system, the range over which the capacitance is most frequency-dependent is between 5 Hz and 1 kHz<sup>7</sup>. In organic-based MIS capacitors, the formation of an inversion layer is hindered by the slow rate at which minority carriers are thermally created. However, Lüssem *et al* demonstrated that with the introduction of additional layers of doped pentacene an organic-based inversion transistor can be realized<sup>32</sup>. A population of electrons at the semiconductor/insulator interface can also be stimulated by photon absorption, demonstrated by Watson *et al*<sup>33</sup>, and discussed in section 2.3.5.

### 2.3.3 Doping Density and the Mott-Schottky Analysis

In the  $C$ - $V$  plot of an ideal MIS capacitor, the rate at which the device goes from accumulation to depletion is determined by the doping density  $N_A$  of the semiconductor.

Assuming that there are no free carriers inside the depletion region, a Mott-Schottky plot,  $1/C_M^2$  vs  $V$ , can be used to determine the doping density of a semiconductor. For a uniformly doped semiconductor, the slope of the Mott-Schottky plot yields  $1/N_A$ , while the intersection with the voltage axis yields the built in voltage  $V_{BI}$  of the device, as in Figure 2.10. Depending on the doping type of the semiconductor, the slope can be positive (p-type) or negative (n-type).

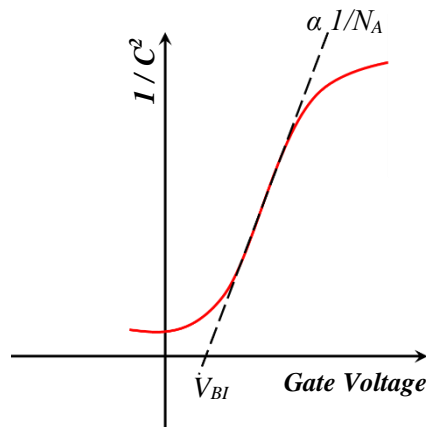


**Figure 2.10 – Mott-Schottky plot, describing the doping density and built-in voltage.**

Furthermore, the analysis also allows the doping density to be determined as a function of depletion region width since:

$$N_A(w) = -\frac{2}{q\epsilon_s} \left( \frac{dC_M(w)^{-2}}{dV} \right)^{-1}. \quad (2.15)$$

### 2.3.4 Real MIS Capacitors and Equivalent Circuits

The use of an ideal scenario may not be enough to explain certain features in everyday devices. Effects such as hysteresis in the  $C$ - $V$  and energy-loss plots can be explained by the presence of interface trap sites, lateral conduction currents and other processes. In this section, a brief description of these properties is given and, to better

understand them, a representation using equivalent circuits is used. A more detailed view of these topics can be found in the literature<sup>7,31,34-38</sup>.

When the majority carriers are not able to respond to the applied AC signal, they will lag behind it and create a source of energy loss through the system. This happens when the charge carrier relaxation time  $\tau_D$  is higher than the applied AC signal period and is modelled by a resistive element in the equivalent circuit. When in accumulation, the device can be represented by the circuit in Figure 2.11, where  $C_B$  is the bulk capacitance of the semiconductor per unit area,  $R_B$  the bulk resistance in parallel with  $C_B$ , and  $C_I$  the insulator capacitance per unit area.

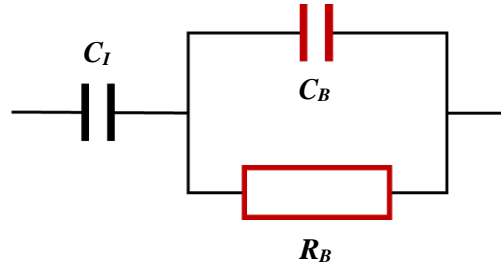


**Figure 2.11 – Equivalent circuit of a MIS capacitor in accumulation.**

The measured capacitance  $C_M$  and loss  $G_M/\omega$  are then given by:

$$C_M = C_G + \frac{C_I - C_G}{1 + (\omega\tau_R)^2} \quad (2.16)$$

$$\frac{G_M}{\omega} = \frac{\omega R_B C_I^2}{1 + (\omega\tau_R)^2} \quad (2.17)$$

where  $C_G$  is the series sum of  $C_I$  and  $C_B$ , and  $\tau_R$  the circuit relaxation time:

$$\tau_R = R_B(C_I + C_B) \quad (2.18)$$

with  $f_R$ , the relaxation frequency, given by:

$$f_R = \frac{1}{2\pi R_B(C_I + C_B)}. \quad (2.19)$$

When the depletion region starts forming, a new capacitive element ( $C_D$ ), representing the depletion region, appears and the bulk of the semiconductor will decrease in length, changing  $R_B$  and  $C_B$  to  $R_B'$  and  $C_B'$ , as in Figure 2.12. As the space-charge region grows,  $R_B'$  decreases and  $C_B'$  increases.

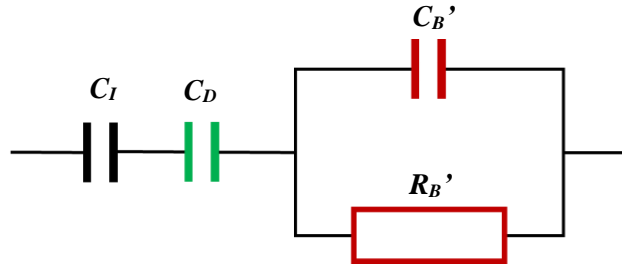


**Figure 2.12 – Equivalent circuit for a MIS capacitor in depletion.**

The loss vs frequency plot displays a Maxwell-Wagner effect, which describes the frequency response of a two-layer dielectric<sup>34,39</sup>. As the device is driven from accumulation to full depletion, the relaxation frequency  $f_R$  will increase between the limits<sup>34</sup>:

$$\frac{1}{2\pi R_B(C_I + C_B)} < f_R < \frac{1}{2\pi \rho_S \epsilon_S} \quad (2.20)$$

where  $\rho_S$  is the semiconductor resistivity.

The effects of the depletion region thickness on Capacitance-Frequency ( $C$ - $f$ ) and Loss-Frequency ( $G/\omega$ - $f$ ) plots were simulated using Equations 2.16 and 2.17 and are shown in Figure 2.13. In accumulation (black line) at low frequencies  $f \ll f_R$ , charges are able to follow the small-signal voltage and do not present any source of energy loss, thus the measured capacitance  $C_M \approx C_I$  and  $G/\omega \approx 0$ . As the frequency comes close to the relaxation frequency of the device,  $f \approx f_R$ , charges will lag behind the AC signal and become a source of energy loss with a maximum centred at  $f = f_R$ . As this happens,  $R_B$  no longer shunts  $C_B$  and  $C_M$  decreases with increasing frequency. At higher frequencies,  $f \gg f_R$ , none of the majority carriers are able to respond to the small-signal oscillations, so no energy loss is associated with it and  $C_M$  attains a constant value equal to the series sum of  $C_I$  and  $C_B$ .

As the depletion region thickness increases, its influence become more relevant and at low frequencies,  $C_M$  decreases and is represented by a series sum of  $C_I$  and  $C_D$ . When the depletion region spans the whole semiconductor (red line), the measured capacitance remains at a minimum value, corresponding to the series sum of  $C_I$  and  $C_B$ , over the whole frequency range. In this case, the semiconductor is depleted of all majority carriers and they do not represent a source of energy loss. The relaxation frequency  $f_R$  increases as depletion thickness increases following Equation 2.20, moving the loss peak to higher frequencies.

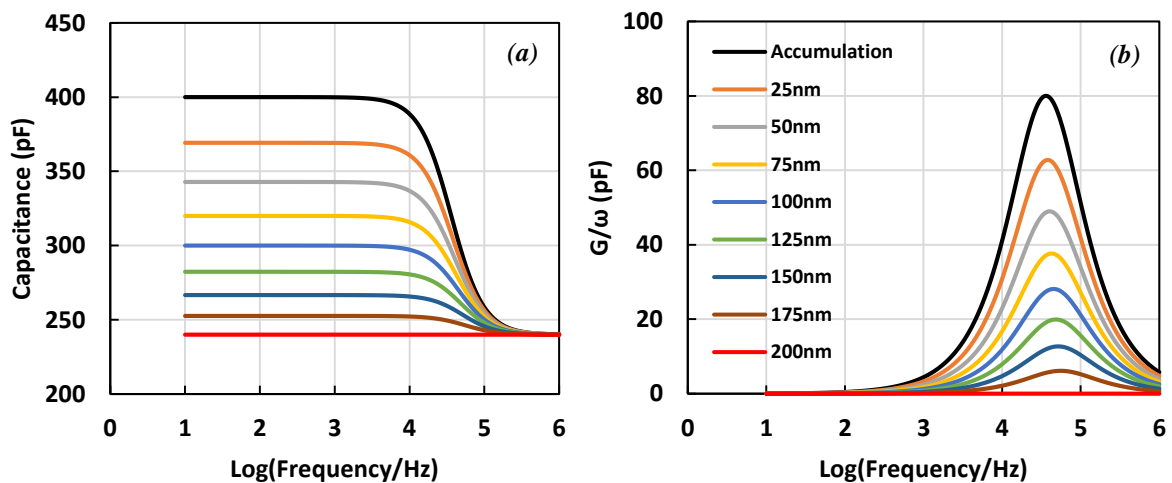


**Figure 2.13– Simulated (a)  $C$ - $f$  and (b)  $G/\omega$ - $f$  for an ideal MIS capacitor driven from accumulation (black line) to full depletion (red line). Semiconductor layer thickness used was 200 nm,  $C_I = 400$  pF,  $R_B = 4400 \Omega$  and  $C_B = 600$  pF.**

### 2.3.4.1 Contact Resistance

In real MIS devices, the work function of the top contact might not match exactly the conduction or valence band energies of the semiconductor, providing a barrier for charge injection/extraction. Such a barrier can be represented by a resistive element  $R_C$  in series with the rest of the circuit, represented in Figure 2.14.

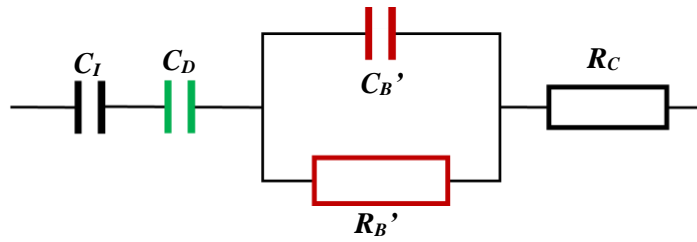


**Figure 2.14 – Equivalent circuit for a MIS in depletion with contact resistance.**

The extra resistive element acts as a second source of energy loss with an associated relaxation frequency  $f_R$  given by:

$$f_R = \frac{1}{2\pi R_C C_S} \quad (2.21)$$

where  $C_S$  is the series combination of  $C_I$ ,  $C_D$  and  $C_B'$ . This energy loss occurs at much higher frequencies than the one related to the classical Maxwell-Wagner dispersion<sup>34</sup>. It also causes the measured capacitance to fall to zero.

### 2.3.4.2 Time Constant Dispersion

Due to the hopping nature of charge transport in organic semiconductors, the charge carrier mobility is frequency-dependent and this can be seen as a broadening of the Maxwell-Wagner dispersion and reduction in loss peak<sup>34</sup>. This behaviour can be modelled as a distribution of majority carrier relaxation times centred at  $\tau_R$ , which is represented by the equivalent circuit in Figure 2.15.

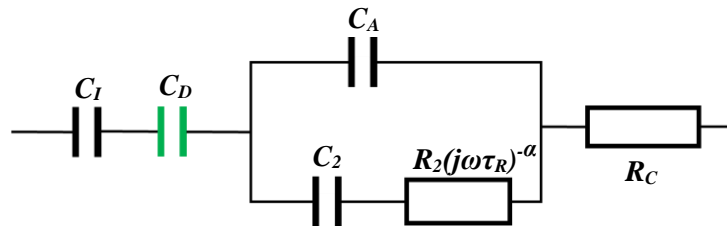


**Figure 2.15 – Equivalent circuit for a MIS device in depletion with a distribution of relaxation frequencies.**

The parameter  $\alpha$  is a fitting parameter that ranges from 0 to 1. When  $\alpha = 0$  the circuit reverts back to the one in Figure 2.14 and as  $\alpha$  increases, the relaxation frequency dispersion increases and the broadening and reduction of the loss peak centred at  $\tau_R$  increases.

### 2.3.4.3 Flatband Voltage

In the ideal scenario, the semiconductor and metal gate have the same work function and the insulator is free of any charges, so that the flatband voltage  $V_{FB}$  is zero. This is not always the case in real MIS devices. Differences in work function and insulator charges induce deviations from the ideal scenario, requiring additional voltage to flatten the energy bands. These features can be observed as horizontal shifts in the  $C$ - $V$  curve of MIS devices, represented by the red and green lines in Figure 2.16.

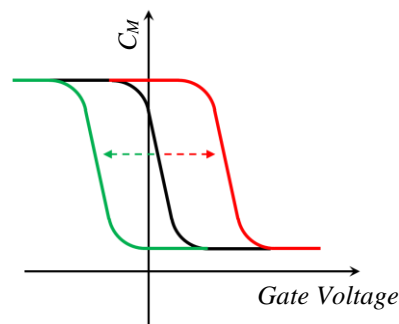


**Figure 2.16 – Horizontal shifts in  $C$ - $V$  curve of MIS devices for  $V_{FB} = 0$  (black line);  $V_{FB} > 0$  (red line) and  $V_{FB} < 0$  (green line).**

Assuming a p-type semiconductor as an example, a positive shift in  $V_{FB}$  indicates either that negative charges are present in the insulator, or that the metal work function is less than the semiconductor's. On the other hand, a negative  $V_{FB}$  indicates that the insulator has positive charges or that the metal work function is greater than the semiconductor's. In any case, the shift in  $V_{FB}$  can be described by:

$$\Delta V_{FB} = \varphi_{ms} - \frac{Q_I}{C_I} \quad (2.22)$$

where  $\varphi_{ms}$  is the metal-semiconductor work function difference and  $Q_I$  the charge density in the insulator.

The nature of these insulator charges can be fixed, mobile ionic entities or trapped charges that are initially neutral but acquire charge through other processes (current through insulator, photon excitation, etc.)<sup>7</sup>. Control of sample quality plays an important role in preventing any unwanted impurity-induced trap sites and charge centres. Shifts in the flatband voltage can also be caused by charge trapping at the semiconductor/insulator interface and can be the origin of hysteresis in the  $C$ - $V$  curve.

#### **2.3.4.4 Insulator leakage**

In an ideal MIS capacitor, the conductance of the insulating layer is assumed to be zero. However, real insulators will always display some degree of leakage current. Depending on the device, high leakage currents ( $> 10^{-10}$  A) can influence the response of the device and can be a source of operational instability, leading to short lifetimes<sup>40</sup>. The origin of these currents can vary and, in most cases, are dependent on the electric field intensity and temperature. Figure 2.17 represents three common types of carrier transport through the insulating layer.

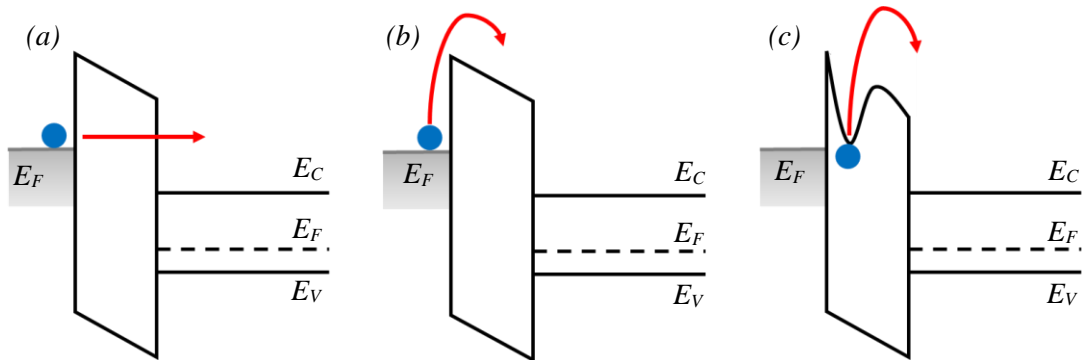


**Figure 2.17 – Energy-band diagram showing conduction mechanism of (a) tunnelling, (b) thermionic emission, and (c) Frenkel-Poole emission. Adapted from <sup>7</sup>.**

In the direct tunnelling case, charges have a probability of penetrating through the insulator barrier and, when high fields are present, it is the most common conduction mechanism<sup>7</sup>, especially in ultra-thin insulators. In thermionic emission, charges go over the barrier while in the Frenkel-Poole emission, charges are released from traps into the conduction band through thermal excitation. Such conduction effects are represented by an additional resistance  $R_I$  parallel to the insulator capacitance (Figure 2.18).

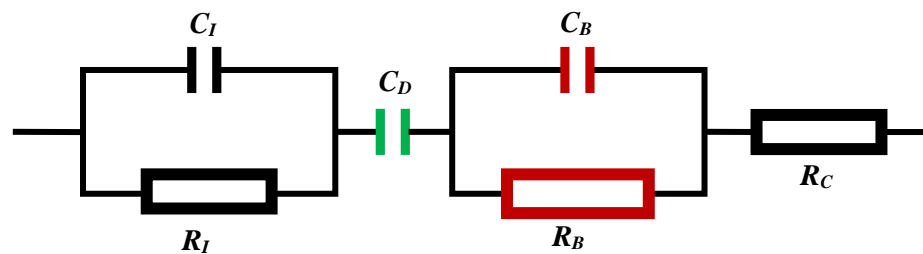


**Figure 2.18 – Equivalent circuit of a MIS capacitor in depletion with insulator leakage effects.**

### 2.3.4.5 Interface states

The properties of the semiconductor/insulator interface have significant importance to several devices, the transistor being one of them. Injected charges go through the channel formed near the interface and imperfections lead to smaller than expected

output currents. Surface roughness and impurities can create energy barriers and interface states that hinder the charge transport along the semiconductor/insulator interface. The same happens in a MIS capacitor, where interface states can trap/release charges through its operation, changing its  $C$ - $V$  profile.

These states give rise to energy levels within the semiconductor band gap and the capture, storage and release of charge carriers can be described by the additional  $R_T$ - $C_T$  branch represented in Figure 2.19. Interface states have a distribution of associated energies and each individual state will have a corresponding R-C branch, but only those located a few  $kT$  ( $k$  being the Boltzmann constant and  $T$  the absolute temperature) either side of  $E_{FS}$  will change occupancy and contribute to the measured admittance<sup>34,35</sup>. The R-C branches can be condensed into one frequency-dependent parallel R-C<sup>34</sup>, as in Figure 2.20.

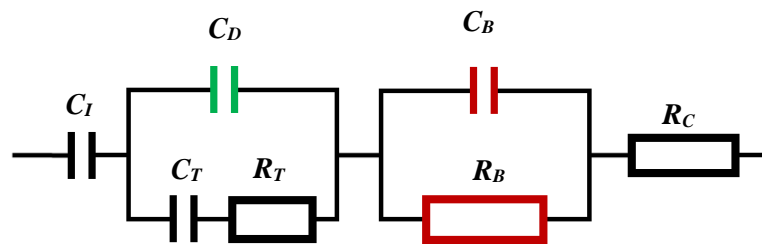


**Figure 2.19 – Equivalent circuit of a MIS with a single interface state level.**

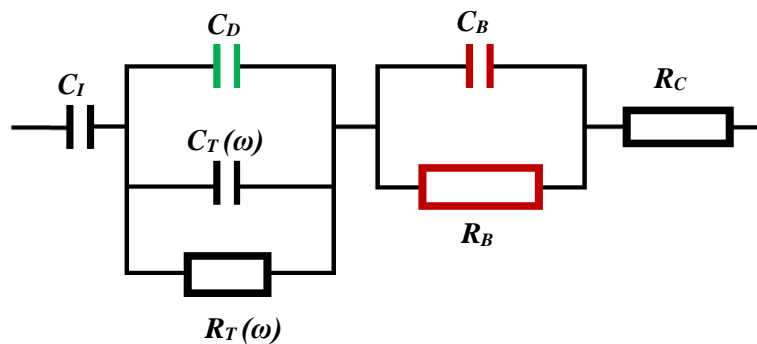


**Figure 2.20 – Equivalent circuit of a MIS device with a distribution of interface state energies.**

### 2.3.4.6 Lateral conduction

Solution processing of organic semiconductors is one of the cheapest and fastest ways of depositing organic materials. The spin-coating technique, for example, relies on rotating the substrate with the desired solution at very high speed, covering the whole substrate with a thin layer (~100 nm) of organic compound. The excess solvent can be removed by an annealing process. Usually, when preparing samples by spin-coating, the semiconducting layer covers the whole substrate and, if no patterning process is used, the excess semiconductor layer can affect the performance of electronic devices. The control of these lateral current effects is important, since it can act as another path for charges to move.

If the semiconductor layer extends beyond the perimeter of the top or bottom electrode in a MIS capacitor, the majority carriers can move to the excess area, extending the accumulation layer surface and changing the measured capacitance  $C_M$ . In accumulation, majority carriers can flow laterally, increasing the device area. When the depletion region is formed, its high resistance avoids the flow of charges and the lateral conduction effects are reduced. The length at which carriers can move laterally is limited by the applied AC frequency. If the signal frequency is low, carriers can diffuse a long way into the excess semiconductor, while at high frequencies the charge carriers are confined to the electrode area<sup>37</sup>.

### 2.3.5 Organic MIS Capacitors

In this section, a very brief discussion of organic-based MIS capacitors in the literature is made. Unfortunately, the use of organic semiconductors in MIS capacitors is not as vast as in other devices, such as transistors and solar cells. As mentioned in previous sections, organic semiconductors differ from their inorganic counterparts, but most

analyses of organic-based devices follow the model derived for inorganic semiconductors.

Using a structure similar to two MIS capacitors connected in series, Watson and Taylor showed how photo-created charges can be transferred from one device to another<sup>33</sup>. The charge-injection-device (CID) is a primitive version of the optical sensor known as the charge-coupled-device (CCD). Such a structure consists of two capacitors where charge carriers can flow from one to the other by controlling the respective gate bias. The device was made with P3HT, a polymer widely used in organic solar cells due to its good absorption of visible light, and the photoresist SU8-2000.5 as the insulating layer. By measuring the C-V profile of both capacitors separately in the dark and with light exposure, the authors were able to show that light only entered the first MIS capacitor. The photo-generated electrons were drawn to the semiconductor/insulator interface and remained there either trapped or free, both producing a shift in the flatband voltage of the device and creating a hysteresis effect in the C-V curve. The authors managed to transfer some of the photocreated charges from one capacitor to the other changing its C-V response, even though light was not entering it. Such hysteresis was observed on the second capacitor while the first was illuminated, indicating that a part of the created charges were transferred<sup>33</sup>. The authors determined the efficiency of charge transfer to be as high as 40%<sup>33</sup>.

In later works<sup>9</sup>, the authors developed a model describing how light affects the C-V response of organic-based MIS capacitors. As before, photo-created electrons accumulated at the interface causing a positive shift in the flatband voltage which, resulted in anticlockwise hysteresis. The rate of excess charge increase also caused the depletion capacitance to rise from a minimum value in the dark to a new level depending on the light intensity and voltage sweep rate, as in Figure 2.21*a*. The authors exposed the device to light in the 400-700 nm range and the results were consistent with the absorption profile of P3HT<sup>9</sup>. The theoretical model proposed by the authors is similar to the ones described in section 2.3.4 which understands the depletion region as a two-plate capacitor in series with the insulator capacitance. Light that entered the

capacitor through the insulator was absorbed by P3HT, which decreased the light intensity at a depth  $x$  following Lambert's law (section 2.2.2).

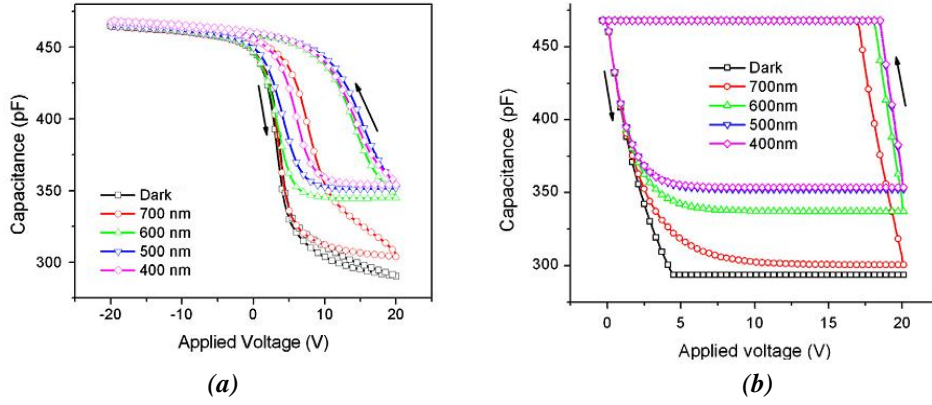


**Figure 2.21 – Experimental (a) and simulated (b) effect of light energy on the C-V response of P3HT-based MIS capacitors.**

**Adapted with permission from <sup>9</sup>.**

The local change in photon density then determines the exciton generation rate through:

$$\frac{dN_{ex}(x)}{dt} = -\eta \frac{d\phi(x)}{dx} = \eta \frac{\lambda}{hc} \alpha(\lambda) I_0 e^{-\alpha(\lambda)x} \quad (2.23)$$

where  $N_{ex}(x)$  is the exciton concentration,  $\eta$  represents the efficiency of exciton generation,  $\Phi(x)$  is the photon flux density,  $h$  is the Planck's constant,  $c$  is the speed of light in vacuum,  $I_0$  is the initial light intensity,  $\lambda$  is the light's wavelength and  $\alpha(\lambda)$  is the absorption coefficient.

The authors assumed that photo-created excitons dissociate into free charge carriers subject to the local Coulomb and electric fields following the Onsager model for geminate recombination<sup>9</sup>. It was also assumed that all free electrons would reach the semiconductor/insulator interface and become trapped, therefore, the rate of electron trapping  $dn_t(t)/dt$  could be written as:

$$\frac{dn_t(t)}{dt} = \eta \frac{\lambda I_0}{hc} \xi(0) \alpha(\lambda) \int_0^{d_p(t)} e^{-\alpha(\lambda)x} (1 + \beta F(x)) dx \quad (2.24)$$

where  $\xi(0)$  is the probability of exciton dissociation when  $F$ , the electric field, is zero,  $d_p(t)$  is the depletion region thickness and  $\beta$  is a constant given by:

$$\beta = \frac{e^3}{8\pi\epsilon\epsilon_0 k^2 T^2} \quad (2.25)$$

where  $e$  is the fundamental electrical charge,  $k$  is Boltzmann's constant and  $T$  the temperature in Kelvin.

By integrating equation 2.24, the authors were able to evaluate  $dn_i(t)/dt$  which was then used to calculate the shift in the flatband voltage. With that, the authors estimated the depletion region thickness needed to compute the final capacitance of the device. The proposed model was cyclic. The depletion region thickness was needed to calculate the electron trapping which would then be used to estimate a new depletion region value. A simulated C-V curve is shown in Figure 2.21b. By assuming that all photo-created charges were trapped, the model would always produce a large hysteresis effect on the return sweep. On a first analysis, the model predicted the expected behaviour of a p-type semiconductor but did not assume that photo-created charges could remain free at the interface or that trapped charges could be released.

Another point of discussion for organic-based devices is the validity of the Mott-Schottky analysis, discussed in section 2.3.3, for estimating the doping density. The apparent doping density of organic semiconductors calculated from this method may be incorrect, as explained by Kirchartz *et al*<sup>41</sup>. Using a drift-diffusion model, the authors considered two situations in organic solar cells: *a*) low doping densities, where the estimated  $N_A$  would resemble the one from an intrinsic semiconductor, as in Figure 2.22a; and *b*) thin semiconductor layers (below 100 nm), where the apparent  $N_A$  would be overestimated by almost an order of magnitude, Figure 2.22b.

In intrinsic or lightly doped materials, the capacitance is no longer dominated by the charge of the doping atoms, but instead by the charge carriers injected from the electrodes<sup>41</sup>. In Figure 2.22a, the Mott-Schottky analysis has been used to calculate the apparent doping density for three simulated cases: an intrinsic semiconductor (black line), low doping density  $N_A = 5 \times 10^{15} \text{ cm}^{-3}$  (blue dots) and regular doping density  $N_A = 5 \times 10^{16} \text{ cm}^{-3}$  (red squares).

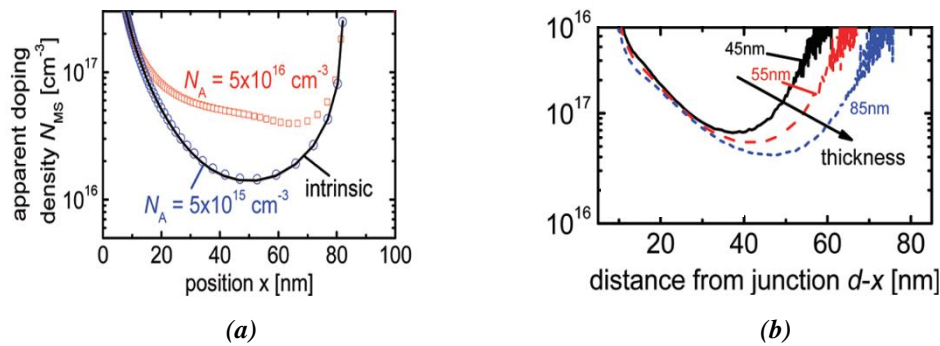


**Figure 2.22 – Estimated doping density deviations for (a) low doping densities; and (b) thin semiconductor layers. Reprinted with permission from<sup>41</sup>. Copyright 2017 American Chemical Society.**

The authors showed that for lightly doped semiconductors  $N_A < 1 \times 10^{16} \text{ cm}^{-3}$  and usual semiconductor thicknesses of 100 nm, the apparent doping density calculated from this method may not be detected<sup>41</sup>. It is important to note however, that when the authors expanded the active layer thickness to 1  $\mu\text{m}$ , the low doping density case could be detected. Their results indicate that for every thickness there is a range of doping densities that are not detectable<sup>41</sup>.

For thin semiconducting layers, the apparent doping density calculated from the Mott-Schottky analysis may be overestimated by one order of magnitude. Figure 2.22b shows three experimental results, for the same semiconductor, with different thickness: 45 nm (black line), 55 nm (red dashed line) and 85 nm (blue dashed line). The authors concluded that the apparent  $N_A$  calculated from the Mott-Schottky analysis for thicker and/or more heavily doped devices is more reliable<sup>41</sup>.

Using a different approach, Maddalena *et al*<sup>42</sup> extracted the width of the density of states (DOS) from the C-V profile of MIS capacitors. Determining the DOS of van der Waals, disordered molecular solids is a far from trivial problem, since every molecule has its own unique environment<sup>42</sup>. For their calculations, the authors assumed that the semiconductor is intrinsic, a different approach from that discussed above, and modelled the C-V curve by analysing the position of the centre of charge as a function of gate voltage. The theory described in section 2.3 uses the depletion region thickness

as a parameter to explain the features seen in the C-V response. During the modelling, the authors were able to fit values for the width of the Gaussian distribution of the DOS and observed that upon increasing disorder, the functional dependence of the centre of charge on  $V_G$  becomes smoother, hence the C-V curve becomes less steep, as in Figure 2.23. The authors also detected differences when comparing patterned and unpatterned semiconductor layers due to lateral conduction effects, mentioned in the above section.

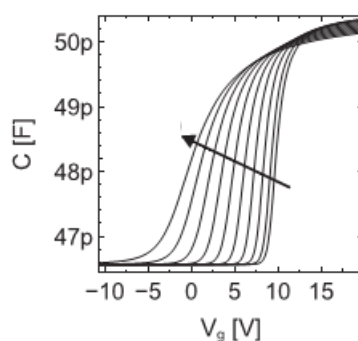


**Figure 2.23 – Simulated C-V curves. The arrow indicates the increase in disorder/broadening of the DOS. Reprinted from <sup>42</sup> with permission from Elsevier.**

## CONCLUSION

In this chapter, the relevant theoretical background for understanding organic semiconductors and their uses in electronic devices were briefly explained. In section 2.2, the ideas of how the semiconductor character arises from the  $sp^2$  hybridization in an organic semiconductor, how light interacts with them and how charge transport can occur even in a material thought to be insulating were discussed. The hopping nature of the charge transport in disordered materials was briefly explained.

In section 2.3, the operation of an MIS capacitor and its admittance, needed to better understand the analyses throughout this thesis, were reviewed. First, the ideal

MIS capacitor was introduced. The effects of depletion region in the C-V response were also discussed. Later, in the subsection 2.3.4, the operation of realistic MIS devices with interface states, lateral conduction effects, shifts in the flatband voltage and insulator leakage were mentioned.

In the last subsection, a very brief review was provided of some major papers centred around organic MIS capacitors. From this short analysis, it is clear that there is still room for debate in the field of organic electronics. Models that depart from two very different points, i.e. assuming that the semiconductor is doped or intrinsic, can reproduce with good results a similar C-V response behaviour. This will be a topic of discussion in the following results chapter.

## REFERENCES

- 1 H. Bässler and A. Köhler, in *Unimolecular and Supramolecular Electronics I; Vol. 312*, edited by R. M. Metzger (Springer Berlin Heidelberg, 2012), p. 1.
- 2 Orbital Hybridization, [en.wikipedia.org/wiki/Orbital\\_hybridisation](http://en.wikipedia.org/wiki/Orbital_hybridisation), accessed Jan 2017 (2017).
- 3 D. J. Coutinho, Master Dissertation, Universidade de São Paulo (2011).
- 4 S. Günes, H. Neugebauer, and N. S. Sariciftci, *Chemical Reviews* **107**, 1324 (2007).
- 5 H. Bässler, *Physica Status Solidi (b)* **175**, 15 (1993).
- 6 H.-H. Cho, T. E. Kang, K.-H. Kim, H. Kang, H. J. Kim, and B. J. Kim, *Macromolecules* **45**, 6415 (2012).
- 7 S. M. Sze, *Physics of Semiconductor Devices* (John Wiley & Sons, 1981).
- 8 K.-J. Baeg, M. Binda, D. Natali, M. Caironi, and Y.-Y. Noh, *Advanced Materials* **25**, 4267 (2013).
- 9 C. P. Watson, M. Devynck, and D. M. Taylor, *Organic Electronics* **14**, 1728 (2013).
- 10 M. Devynck, B. Rostirolla, C. P. Watson, and D. M. Taylor, *Applied Physics Letters* **105**, 183301 (2014).
- 11 Y. Yang, W. Chen, L. Dou, W.-H. Chang, H.-S. Duan, B. Bob, and G. Li, *Nature Photonics* **9**, 190 (2015).
- 12 M. C. Scharber, *Advanced Materials* **28**, 1994 (2016).
- 13 I. J. Curtin, D. W. Blaylock, and R. J. Holmes, *Applied Physics Letters* **108**, 163301 (2016).
- 14 D. M. Taylor, J. A. Drysdale, I. Torres, and O. Fernández, *Applied Physics Letters* **89** (2006).
- 15 J. Lancaster, D. M. Taylor, P. Sayers, and H. L. Gomes, *Applied Physics Letters* **90** (2007).
- 16 K. A. McGarry, W. Xie, C. Sutton, C. Risko, Y. Wu, V. G. Young, J.-L. Brédas, C. D. Frisbie, and C. J. Douglas, *Chemistry of Materials* **25**, 2254 (2013).
- 17 Y. Nakayama, J. Niederhausen, S. i. Machida, Y. Uragami, H. Kinjo, A. Vollmer, J. P. Rabe, N. Koch, and H. Ishii, *Organic Electronics* **14**, 1825 (2013).
- 18 C.-H. Wang, C.-Y. Hsieh, and J.-C. Hwang, *Advanced Materials* **23**, 1630 (2011).
- 19 D. Ji, L. Jiang, X. Cai, H. Dong, Q. Meng, G. Tian, D. Wu, J. Li, and W. Hu, *Organic Electronics* **14**, 2528 (2013).
- 20 J. Takeya, M. Yamagishi, Y. Tominari, R. Hirahara, Y. Nakazawa, T. Nishikawa, T. Kawase, T. Shimoda, and S. Ogawa, *Applied Physics Letters* **90** (2007).
- 21 Z. Ding, G. Abbas, H. E. Assender, J. J. Morrison, S. G. Yeates, E. R. Patchett, and D. M. Taylor, *ACS Applied Materials & Interfaces* **6**, 15224 (2014).
- 22 E. R. Patchett, A. Williams, Z. Ding, G. Abbas, H. E. Assender, J. J. Morrison, S. G. Yeates, and D. M. Taylor, *Organic Electronics* **15**, 1493 (2014).
- 23 J. Park, L.-M. Do, J.-H. Bae, Y.-S. Jeong, C. Pearson, and M. C. Petty, *Organic Electronics* **14**, 2101 (2013).
- 24 H. Klauk, M. Halik, U. Zschieschang, G. Schmid, W. Radlik, and W. Weber, *Journal of Applied Physics* **92**, 5259 (2002).

- 25 M. da Silva Ozório, G. L. Nogueira, R. M. Morais, C. da Silva Martin, C. J. L. Constantino,  
and N. Alves, *Thin Solid Films* **608**, 97 (2016).
- 26 Y. Zhang, Y. Diao, H. Lee, T. J. Mirabito, R. W. Johnson, E. Puodziukynaite, J. John, K. R.  
Carter, T. Emrick, S. C. B. Mannsfeld, and A. L. Briseno, *Nano Letters* **14**, 5547 (2014).
- 27 H. Sirringhaus, *Advanced Materials* **26**, 1319 (2014).
- 28 G. A. Abbas, Z. Ding, H. E. Assender, J. J. Morrison, S. G. Yeates, E. R. Patchett, and D.  
M. Taylor, *Organic Electronics* **15**, 1998 (2014).
- 29 E. G. Bittle, J. I. Basham, T. N. Jackson, O. D. Jurchescu, and D. J. Gundlach, *Nature*  
*Communications* **7**, 10908 (2016).
- 30 RNCOS, "Global Semiconductor Market Outlook 2022," (2016).
- 31 D. Neamen, *Semiconductor Physics and Devices* (Mc Graw Hill, 2003).
- 32 B. Lüssem, M. L. Tietze, H. Kleemann, C. Hoßbach, J. W. Bartha, A. Zakhidov, and K.  
Leo, *Nature Communications* **4**, 2775 (2013).
- 33 C. P. Watson and D. M. Taylor, *Applied Physics Letters* **99** (2011).
- 34 I. Torres and D. M. Taylor, *Journal of Applied Physics* **98** (2005).
- 35 C. P. Watson, PhD Thesis, Bangor University (2011).
- 36 N. Alves and D. M. Taylor, *Applied Physics Letters* **92** (2008).
- 37 D. M. Taylor and N. Alves, *Journal of Applied Physics* **103** (2008).
- 38 I. Torres, D. M. Taylor, and E. Itoh, *Applied Physics Letters* **85**, 314 (2004).
- 39 T. Prodromakis and C. Papavassiliou, *Applied Surface Science* **255**, 6989 (2009).
- 40 P. A. Bobbert, A. Sharma, S. G. J. Mathijssen, M. Kemerink, and D. M. de Leeuw,  
*Advanced Materials* **24**, 1146 (2012).
- 41 T. Kirchartz, W. Gong, S. A. Hawks, T. Agostinelli, R. C. I. MacKenzie, Y. Yang, and J.  
Nelson, *The Journal of Physical Chemistry C* **116**, 7672 (2012).
- 42 F. Maddalena, C. de Falco, M. Caironi, and D. Natali, *Organic Electronics* **17**, 304  
(2015).

# CHAPTER 3

## MATERIALS & METHODS

### 3.1 Introduction

The different materials, experimental methods and fabrication techniques used throughout the development of this thesis are introduced in this chapter. Aiming at giving the reader some background information, the specifics of each device design and fabrication will be discussed when they are relevant. With this in mind, first a description of the semiconducting and insulating materials is provided, along with an extensive list of references detailing its uses in organic-based electronic devices. Then, the procedures involving the different devices are explained and lastly, the experimental methods used to characterize and investigate the properties of the organic devices are discussed.

## 3.2 Materials

### 3.2.1 Poly(3-hexylthiophene)

Poly(3-hexylthiophene) (P3HT) (Figure 3.1) is one of the most commonly used polythiophenes in organic electronics<sup>1-3</sup>, with extensive studies in organic-based transistors<sup>4</sup> and especially in organic solar cells<sup>5,6</sup>. In 1986 Tsumura et al produced the first polythiophene-based transistor with a hole mobility of  $10^{-5}$  cm<sup>2</sup>/Vs<sup>[7]</sup>, demonstrating the promising future that this class of materials would have. However, the inability to make a solution out of unsubstituted polythiophene hampered the development of high performance devices in the early stages. Nowadays, side chains that are attached to the #3 carbon atom of the thiophene backbone makes possible the solubility of polythiophenes in organic solvents, such as chloroform and chlorobenzene. Of the different poly(alkyl thiophene), P3HT stood out due to its great light absorption in the visible range and with a hole mobility in the  $10^{-2}$ - $10^{-1}$  cm<sup>2</sup>/Vs range<sup>[8]</sup>, making P3HT a good candidate for organic electronic devices.

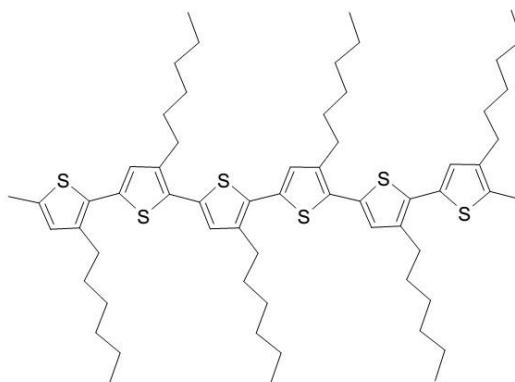


**Figure 3.1 – Chemical structure of regioregular P3HT.**

Of the three different configurations, the Head-to-Tail (HT) coupling allows the best  $\pi$ -orbital overlap, resulting in better charge transport characteristics. A high degree of HT regioregularity is often associated with higher performance devices<sup>9</sup>. Although a polymer by nature, P3HT films can achieve a good degree of polycrystallinity with the use of post-process techniques. Such procedures, for example annealing the film

under vacuum and slowly removing the solvent components, has been shown to increase the charge transport properties due to changes in the film morphology<sup>9-12</sup>.

Regarded as a p-type semiconductor, P3HT as for most organic semiconductors, also suffers from oxidation processes leading to higher doping densities and poorer device performances. Such stability issues are often tackled by encapsulating the device and thus delaying any effects from the environment. Even though higher performance semiconductors are available nowadays, P3HT is still used in investigations regarding the fundamental aspects of organic semiconductors due to the extensive literature around it.

### 3.2.2 [6,6]-Phenyl C<sub>61</sub> butyric acid methyl ester

[6,6]-Phenyl C<sub>61</sub> butyric acid methyl ester (PCBM) is a material from the fullerene family (Figure 3.2), often used in organic solar cells in conjunction with P3HT<sup>5</sup>. Fullerenes, spherical molecules made of pentagonal and hexagonal carbon rings, were first discovered in their stable form in 1985 by Kroto et al<sup>13</sup>, when the authors were trying to understand the mechanism by which long-chain carbon molecules are formed in interstellar space. The proposed structure, a truncated icosahedron, was not fully admitted by the scientific community at the time<sup>14</sup>, but many detailed investigations<sup>15,16</sup> followed the initial article providing substantial experimental data for the unusually stable structure of fullerenes. The idea that carbon could naturally be arranged in another structure rather than graphite or diamond sprouted a whole new field of research, eventually awarding Harold W. Kroto, Robert F. Curl and Richard E. Smalley the Nobel Prize for Chemistry in 1996<sup>17</sup> for the discovery of fullerenes.

Nowadays, the large-scale production of fullerene derivatives is common and its uses in biomedical and photoelectronics research have matured. On the biological side, fullerene derivatives work as a “functionalized cage” and are primarily used in radio-imaging, gene/drug delivery, oxidative stress reduction and cancer therapy<sup>18,19</sup>.

On the electronics side, fullerenes are used as an electron acceptor molecule due to its low lying LUMO and n-type behaviour.

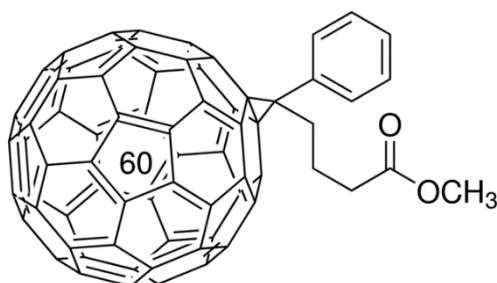


**Figure 3.2 – Chemical structure of PCBM.**

In plastic solar cells, fullerenes are used in conjunction with an absorbing conjugated polymer. By making a polymer:fullerene blend, the length at which the photocreated exciton needs to move before being dissociated is decreased drastically, enhancing the efficiency of charge collection<sup>2,20,21</sup>. The most common fullerene derivative in organic electronics is PCBM, with an improved solubility in organic solvents due to the presence of the side chains. Due to the relatively high electron mobility (in the range of  $10^{-3}$ - $10^{-2}$  cm<sup>2</sup>/Vs), PCBM has also been investigated in field-effect transistors<sup>22,23</sup>.

### 3.2.3 Dinaphtho[2,3-b:2',3'-f]thieno[3,2-b]thiophene

First synthesized by Yamamoto and Takimiya in 2007<sup>24</sup>, the small molecule dinaphtho[2,3-b:2',3'-f]thieno[3,2-b]thiophene (DNTT) (Figure 3.3) showed great air stability and robustness<sup>25</sup>, even over a storage period of 9 months<sup>26</sup> when used in organic devices. Although organic transistors have been researched for quite a while now, they still struggle with environmental and operational stability problems. The presence of oxygen, moisture and/or light can affect the performance of such devices and ultimately hinder the charge transport behaviour. Similar to pentacene, DNTT has two thiophene central rings attached to two benzene rings at each side. Such a

configuration increases its ionization potential when compared to pentacene, making the DNTT molecule less prone to oxidation effects. Together with its low lying HOMO of -5.19 eV, DNTT's energy gap of 3.38 eV also contributes to its great environmental stability<sup>24</sup>.

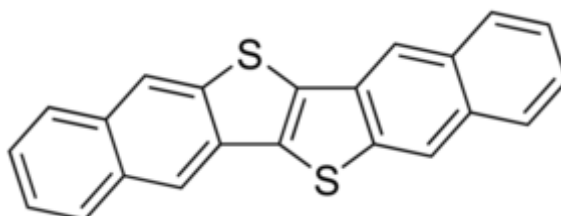


**Figure 3.3 – Chemical structure of DNTT.**

Since the development of DNTT, its use in organic electronic devices has been exploited. Several reports make use of the air-stable small molecule in transistors<sup>24,26-30</sup>, achieving hole mobility as high as 8.3 cm<sup>2</sup>/Vs with an on/off ratio >10<sup>8</sup> when in single crystal form<sup>31</sup>. Due to its high charge carrier mobility and environmental stability, DNTT and its derivatives have been used in the development of organic-based integrated circuits, such as inverters and ring oscillators<sup>25,32-34</sup>, NOR/NAND gates<sup>35</sup>, memory circuits<sup>36</sup> and OLED drivers<sup>37</sup>. Apart from a few reports<sup>38,39</sup>, the use of DNTT has not been investigated in MIS capacitors. As shown by Hayashi et al<sup>38</sup>, the admittance of the device can be influenced by areas of DNTT not covered by the top electrode due to lateral conduction effects. When the measurements are performed at low frequencies (~10<sup>0</sup>-10<sup>1</sup> Hz) the charge carriers are allowed to drift and diffuse into uncovered areas, resulting in additional energy losses in the device, as explained in Section 2.3.4.6.

### 3.2.4 Poly(4-vinyl phenol)

Poly(4-vinyl phenol) (PVP) (Figure 3.4 a) is a cross-linkable transparent insulating material that has found extensive use in organic thin-film transistors due to its ability to be deposited from solution and the lack of costly post-deposition processes<sup>40</sup>. It was first used as an alternative for thermally grown SiO<sub>2</sub> in 2002, showing great results with pentacene<sup>41</sup>. Being a powder, PVP is mainly dissolved in a solution of poly(melamine-co-formaldehyde) (PMF) and propylene glycol monomethyl ether acetate (PGMEA). While PGMEA is the actual solvent, the addition of PMF in the solution has shown to decrease hysteresis effects in pentacene transistors<sup>42</sup>.

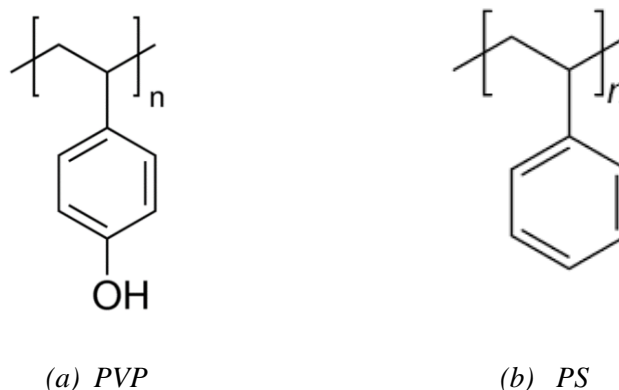


**Figure 3.4 – Chemical structure of (a) PVP and (b) PS.**

To reduce problems arising from some remaining OH<sup>-</sup> groups (which easily attract water), a cross-linking procedure is employed. Usually this step involves a simple thermal annealing in vacuum, however some quicker alternatives such as using microwave ovens are also being studied<sup>43</sup>.

### 3.2.5 Polystyrene

Polystyrene (PS) (Figure 3.4 b) is one of the most commonly used plastics and still find its place in electronics as an insulating layer. PS is solution-processed, transparent and

with a relative dielectric constant of 2.6. Being soluble in toluene, a thermal annealing process after the deposition is usually required to get rid of any remaining solvent.

### 3.3 Fabrication of organic-based devices

To ensure that the samples produced throughout the development of this thesis were free from contaminants and unwanted impurities a strict protocol of fabrication was followed, all of which were performed either inside a Class 1000 Cleanroom facility, or using a N<sub>2</sub>-filled glovebox, both available at Bangor University, using the required personal-protective equipment.

#### 3.3.1 Substrate Cleaning

The substrates used in this thesis were 25x25mm<sup>2</sup> cut microscope slides. They were first gently cleaned using Decon 90 and ultrapure water (UPW) to remove any residual glass from the cutting process. The remaining cleaning procedure was carried in an ultrasonic bath as follows:

<i>Stage</i>	<i>Bath</i>	<i>Time</i>
<i>1</i>	Decon 90 with UPW	5 min; rinse with UPW
<i>2</i>	UPW	5 min; rinse with UPW
<i>3</i>	UPW	5 min; rinse with UPW
<i>4</i>	Acetone	15 min; dried with N <sub>2</sub> flow
<i>5</i>	2-Propanol	15 min; dried with N <sub>2</sub> flow

**Table 3.1 – Substrate cleaning procedure**

### 3.3.2 Spin-Coating

Spin-coating is a solution-based deposition technique that is commonly used in the fabrication of organic electronic devices. The solution is dropped onto the substrate which is rotated at high speeds (typically  $\sim 1000$  rpm), spreading the solution across the surface of the substrate. A thin layer is produced as result while the excess solution is cast away. The final thickness will depend on the solution used, type of substrate and spin speed to mention a few parameters. The uniform wetting of the surface is important and it will depend on the substrate's surface tension and on the solution's surface energy. In this thesis, all spin-coating depositions were made using a modified substrate holder (Figure 3.5), in which the substrate's surface is coplanar with rest of the substrate holder, preventing any accumulation of material at the borders.

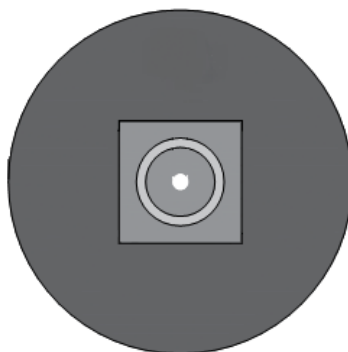


**Figure 3.5 – Top view of the substrate holder. The grey square is a recess where the substrate fits while held by an o-ring and vacuum.**

### 3.3.3 Thermal Evaporation

Thermally evaporating a compound inside a vacuum chamber allows for fine control of the final thickness, with the use of a crystal sensor, while avoiding unwanted contamination from the environment. Such a deposition technique is widely used to make metallic layers (aluminium and gold in this thesis), but also used to deposit small molecules such as DNNT. The materials are placed inside a chamber where the pressure is decreased to values lower than  $5 \times 10^{-6}$  mbar. At these pressures, the oxidation effects are greatly reduced and the temperature required to evaporate a material decreases, allowing for the deposition onto the substrate through a shadow mask without compromising the metallic/organic layer quality.

## 3.4 Measurement Techniques

### 3.4.1 Admittance Experiments

The measurement of the voltage and frequency dependence of the capacitance and loss of MIS capacitors was made using a HP 4284A Precision LCR Meter. For the voltage dependences, the superimposed AC signal always had the same amplitude of 100 mV, while the frequency could vary from 100 Hz to 5kHz in different experiments. The samples were held inside a cryostat (Oxford Instruments Optistat Model DN-V) and the electrical connections were made using conductive silver paint and gold wire. When needed, a rough vacuum pump ( $10^{-2}$  mbar) was connected to the cryostat. The temperature of the sample was controlled by an Oxford Instruments Intelligent Temperature Controller (ITC 502) and, unless stated otherwise, the standard measurement temperature was 300K. During the light experiments, a Xenon lamp was used as light source. The white light would then go through a monochromator (HORIBA Jobin Yvon Triax 320) and filters that were remotely controlled to provide

the desired wavelength. The monochromatic light passed through the cryostat's quartz window and entered the device from the thin transparent aluminium layer.

### 3.4.2 Current-time Experiments

For the I-t experiments, the sample was held inside the cryostat and monochromatic light shone onto the device through the aluminium layer. Light input was remotely switched ON/OFF with the use of a filter wheel and the current was measured as a function of time using a Keithley 617 Programmable Electrometer.

## REFERENCES

- 1 H. Sirringhaus, N. Tessler, and R. H. Friend, *Science* **280**, 1741 (1998).
- 2 S. Günes, H. Neugebauer, and N. S. Sariciftci, *Chemical Reviews* **107**, 1324 (2007).
- 3 J.-F. Chang, B. Sun, D. W. Breiby, M. M. Nielsen, T. I. Sölling, M. Giles, I. McCulloch, and H. Sirringhaus, *Chemistry of Materials* **16**, 4772 (2004).
- 4 L. Reséndiz, M. Estrada, A. Cerdeira, B. Iñiguez, and M. J. Deen, *Organic Electronics* **11**, 1920 (2010).
- 5 M. T. Dang, L. Hirsch, and G. Wantz, *Advanced Materials* **23**, 3597 (2011).
- 6 A. Ng, X. Liu, W. Y. Jim, A. B. Djurišić, K. C. Lo, S. Y. Li, and W. K. Chan, *Journal of Applied Polymer Science* **131**, n/a (2014).
- 7 A. Tsumura, H. Koezuka, and T. Ando, *Applied Physics Letters* **49**, 1210 (1986).
- 8 H. Sirringhaus, P. J. Brown, R. H. Friend, M. M. Nielsen, K. Bechgaard, B. M. W. Langeveld-Voss, A. J. H. Spiering, R. A. J. Janssen, E. W. Meijer, P. Herwig, and D. M. de Leeuw, *Nature* **401**, 685 (1999).
- 9 Y. Kim, S. A. Choulis, J. Nelson, D. D. C. Bradley, S. Cook, and J. R. Durrant, *Applied Physics Letters* **86** (2005).
- 10 G. Li, Y. Yao, H. Yang, V. Shrotriya, G. Yang, and Y. Yang, *Advanced Functional Materials* **17**, 1636 (2007).
- 11 M. Reyes-Reyes, K. Kim, and D. L. Carroll, *Applied Physics Letters* **87**, 083506 (2005).
- 12 A. Zen, J. Pflaum, S. Hirschmann, W. Zhuang, F. Jaiser, U. Asawapirom, J. P. Rabe, U. Scherf, and D. Neher, *Advanced Functional Materials* **14**, 757 (2004).
- 13 H. W. Kroto, J. R. Heath, S. C. O'Brien, R. F. Curl, and R. E. Smalley, *Nature* **318**, 162 (1985).
- 14 H. W. Kroto, A. W. Allaf, and S. P. Balm, *Chemical Reviews* **91**, 1213 (1991).
- 15 R. Taylor, J. P. Hare, A. a. K. Abdul-Sada, and H. W. Kroto, *Journal of the Chemical Society, Chemical Communications*, 1423 (1990).
- 16 W. Kratschmer, L. D. Lamb, K. Fostiropoulos, and D. R. Huffman, *Nature* **347**, 354 (1990).
- 17 Nobelprize.org.
- 18 V. Biju, *Chemical Society Reviews* **43**, 744 (2014).
- 19 M. Yamada, T. Akasaka, and S. Nagase, *Accounts of Chemical Research* **43**, 92 (2010).
- 20 G. Dennler, M. C. Scharber, and C. J. Brabec, *Advanced Materials* **21**, 1323 (2009).
- 21 C. J. Brabec, S. Gowrisanker, J. J. M. Halls, D. Laird, S. Jia, and S. P. Williams, *Advanced Materials* **22**, 3839 (2010).
- 22 C. Waldauf, P. Schilinsky, M. Perisutti, J. Hauch, and C. J. Brabec, *Advanced Materials* **15**, 2084 (2003).
- 23 T. D. Anthopoulos, C. Tanase, S. Setayesh, E. J. Meijer, J. C. Hummelen, P. W. M. Blom, and D. M. de Leeuw, *Advanced Materials* **16**, 2174 (2004).
- 24 T. Yamamoto and K. Takimiya, *Journal of the American Chemical Society* **129**, 2224 (2007).
- 25 U. Zschieschang, F. Ante, T. Yamamoto, K. Takimiya, H. Kuwabara, M. Ikeda, T. Sekitani, T. Someya, K. Kern, and H. Klauk, *Advanced Materials* **22**, 982 (2010).

- 26 Z. Ding, G. Abbas, H. E. Assender, J. J. Morrison, S. G. Yeates, E. R. Patchett, and D. M. Taylor, *ACS Applied Materials & Interfaces* **6**, 15224 (2014).
- 27 K. Pei, Z. Wang, X. Ren, Z. Zhang, B. Peng, and P. K. L. Chan, *Applied Physics Letters* **107**, 033302 (2015).
- 28 U. Zschieschang and H. Klauk, *Organic Electronics* **25**, 340 (2015).
- 29 G. A. Abbas, Z. Ding, H. E. Assender, J. J. Morrison, S. G. Yeates, E. R. Patchett, and D. M. Taylor, *Organic Electronics* **15**, 1998 (2014).
- 30 J.-F. Chang, W.-R. Chen, S.-M. Huang, Y.-C. Lai, X.-Y. Lai, Y.-W. Yang, and C.-H. Wang, *Organic Electronics* **27**, 84 (2015).
- 31 S. Haas, Y. Takahashi, K. Takimiya, and T. Hasegawa, *Applied Physics Letters* **95**, 022111 (2009).
- 32 E. R. Patchett, A. Williams, Z. Ding, G. Abbas, H. E. Assender, J. J. Morrison, S. G. Yeates, and D. M. Taylor, *Organic Electronics* **15**, 1493 (2014).
- 33 U. Zschieschang, R. Hofmockel, R. Rödel, U. Kraft, M. J. Kang, K. Takimiya, T. Zaki, F. Letzkus, J. Butschke, H. Richter, J. N. Burghartz, and H. Klauk, *Organic Electronics* **14**, 1516 (2013).
- 34 D. M. Taylor, E. R. Patchett, A. Williams, Z. Ding, H. E. Assender, J. J. Morrison, and S. G. Yeates, *Chemical Physics* **456**, 85 (2015).
- 35 D. M. Taylor, E. R. Patchett, A. Williams, N. J. Neto, Z. Ding, H. E. Assender, J. J. Morrison, and S. G. Yeates, *Electron Devices, IEEE Transactions on* **61**, 2950 (2014).
- 36 B. Peng and P. K. L. Chan, *Organic Electronics* **15**, 203 (2014).
- 37 Y. Fujisaki, Y. Nakajima, T. Takei, H. Fukagawa, T. Yamamoto, and H. Fujikake, *Electron Devices, IEEE Transactions on* **59**, 3442 (2012).
- 38 T. Hayashi, N. Take, H. Tamura, T. Sekitani, and T. Someya, *Journal of Applied Physics* **115**, 093702 (2014).
- 39 T. Hayashi, N. Take, H. Nakano, A. Fujiwara, T. Sekitani, and T. Someya, *Display Technology, Journal of* **11**, 604 (2015).
- 40 M. E. Roberts, N. Queraltó, S. C. B. Mannsfeld, B. N. Reinecke, W. Knoll, and Z. Bao, *Chemistry of Materials* **21**, 2292 (2009).
- 41 H. Klauk, M. Halik, U. Zschieschang, G. Schmid, W. Radlik, and W. Weber, *Journal of Applied Physics* **92**, 5259 (2002).
- 42 S. C. Lim, S. H. Kim, J. B. Koo, J. H. Lee, C. H. Ku, Y. S. Yang, and T. Zyung, *Applied Physics Letters* **90**, 173512 (2007).
- 43 C.-L. Fan, M.-C. Shang, M.-Y. Hsia, S.-J. Wang, B.-R. Huang, and W.-D. Lee, *APL Mater.* **4**, 036105 (2016).

# CHAPTER 4

## P3HT:PCBM-BASED DEVICES

### 4.1 Introduction

The field of organic electronics has developed rapidly in the past decades, as several electronic devices such as LEDs, transistors and solar cells were fabricated using organic semiconductors. With that, a better understanding of the processes driving their operation was needed. In Chapter 2, it was shown that using simple structures, such as MIS capacitors, can provide some insight into the operation of organic electronic devices.

This chapter discusses the results obtained when P3HT:PCBM blends were used as the active layer in organic MIS capacitors. This particular polymer:fullerene combination is one of the most studied systems in the field of organic electronics<sup>1-6</sup>, mainly due to its excellent light absorption in the visible range and ease of fabrication via solution processes. Firstly, the admittance characteristics of the capacitors were investigated under different experimental conditions. Then the response of the devices

to NIR light was investigated. Finally, the charge transfer characteristics of blend-based charge injection devices were studied.

## 4.2 P3HT:PCBM-based MIS capacitors

### 4.2.1 Overall behaviour of P3HT:PCBM-based capacitors

In this section, MIS capacitors fabricated with the well-known blend of P3HT:PCBM were investigated. The device structure is shown in Figure 4.1 and consisted of an aluminium gate electrode, an insulating layer, a layer of polymer:fullerene blend and evaporated gold as the top electrode.

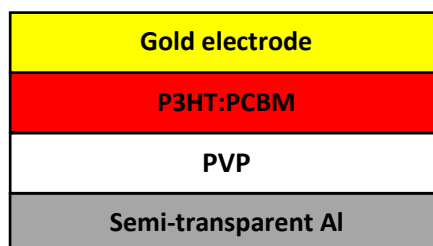
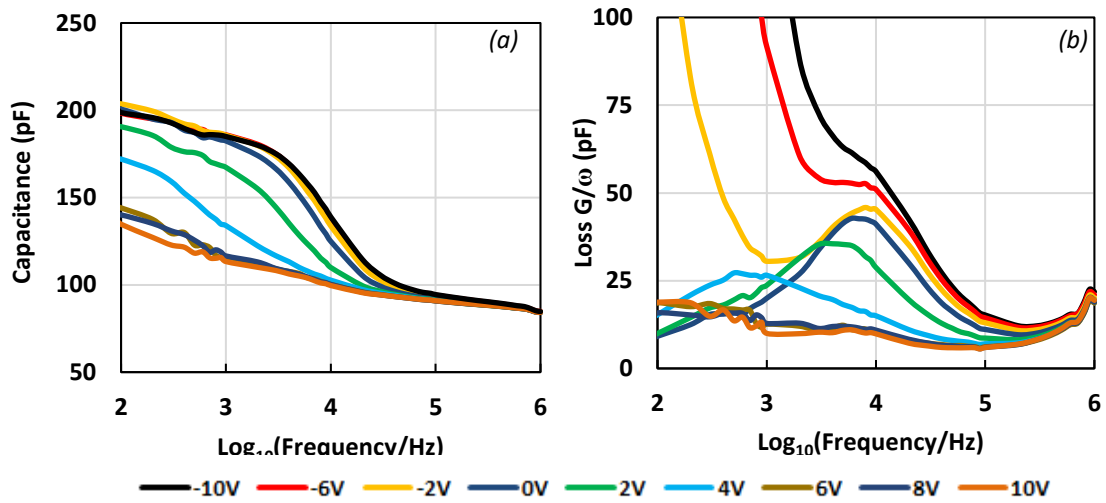


**Figure 4.1 – P3HT:PCBM-based MIS capacitor device structure.**

Glass slides used as substrates were cleaned using standard procedures described in Section 3.3.1. A thin layer (~10 nm) of aluminium was thermally evaporated to serve as a semi-transparent gate electrode, onto which a solution of PVP (3 wt.%) and poly(melamine-co-formaldehyde) (PMF) (1 wt.%) in propylene glycol monomethyl ether acetate (PGMEA) was spin-coated to form the insulating layer. After spin-coating, the PVP layer was thermally cross-linked on a hot plate, initially in air for 2 min at 100 °C and then under vacuum for 30 min at 160 °C. Subsequently, a solution of poly(3-hexylthiophene) (P3HT) and [6,6]-phenyl C<sub>61</sub> butyric acid methyl ester (PCBM) (1:1 weight ratio, 15 mg/mL) in chloroform was spin-coated onto the insulator. In order to remove any residual solvent, the samples were annealed at 140 °C for 1 hour

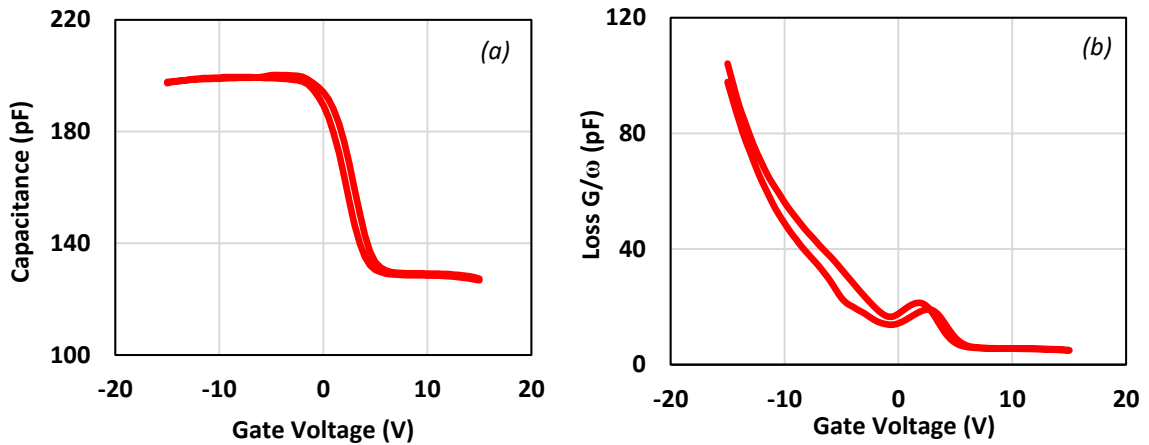
in vacuum. The devices were finished by the thermal evaporation of a ~60 nm thick gold electrode. P3HT and PCBM were kindly provided by Merck Chemicals Ltd., while PVP, PMF and PGMEA were purchased from Sigma-Aldrich. All electrical characterization was carried out using a precision LCR meter (HP 4284A). The admittance plots were obtained with an AC signal amplitude of 100 mV with the bias voltage stepped in 0.5 V increments at a sweep rate of 0.2 V/s.

Figure 4.2 shows (a) capacitance-frequency ( $C$ - $f$ ) and (b) loss-frequency ( $G/\omega$ - $f$ ) curves for a P3HT:PCBM MIS capacitor in the dark, in a  $10^{-2}$  mbar vacuum, at different applied gate voltages. Over the frequency range of  $10^2 - 10^6$  Hz, both the capacitance and loss were dependent on the applied bias. At negative voltages (black line), the capacitance decreased from ~200 pF at  $10^2$  Hz to ~80 pF at  $10^6$  Hz. As the gate bias increased to positive values, the maximum capacitance, measured at 100 Hz decreased from ~200 pF to ~130 pF as the bias increased from -10 V to 6 V (brown line). At higher positive voltages, the capacitance remained independent of the gate bias over the whole frequency range. These shifts are consistent with the formation of a conventional depletion region inside the semiconductor blend<sup>7</sup>, as described in Section 2.3. The  $G/\omega$ - $f$  plot displayed a loss peak centred at ~10 kHz that gradually decreases as the gate voltage increases. The loss peak also shifted to lower frequencies as the voltage increased.



**Figure 4.2 – (a) C-f and (b) loss-f curves of P3HT:PCBM-based MIS capacitor in the dark, under vacuum, at different applied gate voltages.**

The capacitance-voltage ( $C$ - $V$ ) and loss-voltage ( $G/\omega$ - $V$ ) of the same device, in the dark, measured at 1 kHz under vacuum, are shown in Figure 4.3. The curves also showed the typical behaviour of a p-type semiconductor, with an accumulation of holes at negative bias and the formation of a depletion region as the gate bias became positive. The capacitance of the depletion region decreases with increasing positive bias and since it is in series with the insulator capacitance results in a decrease in the measured capacitance, as described in Section 2.3.2. The device showed a very steep accumulation-depletion transition, indicative of a light doping density, accompanied by a loss peak at a similar gate voltage and a near zero flatband voltage. Both plots showed a small anticlockwise hysteresis.



**Figure 4.3 – (a) C-V and (b) loss-V curves of P3HT:PCBM-based MIS capacitor in the dark, in vacuum, at 1 kHz.**

From the accumulation and depletion capacitance, the thickness of the insulator and semiconductor layers can be deduced using equations (2.12) and (2.13). In accumulation, the measured capacitance of  $\sim 200$  pF corresponds to a PVP layer  $\sim 210$  nm thick. From equation (2.13) the depletion layer capacitance was estimated to be  $\sim 350$  pF, which corresponds to a semiconductor layer thickness of  $\sim 80$  nm. In this first approximation, the relative permittivity of PVP used in the calculation was 4.9, while the polymer:fullerene blend was treated as a uniform, p-type effective medium of relative permittivity of 3.4.

In principle, the doping density  $N_A$  of the active layer can be determined from the slope of the  $C^{-2}$  vs  $V_G$  plot, the so-called Mott-Schottky analysis – see Section 2.3.3. However, this method may give overestimated values when the semiconductor thickness is too small, as explained in Section 2.3.5. The doping density was then estimated as a function of the depletion layer thickness using the method described by Kirchartz *et al*<sup>8</sup>, and is shown in Figure 4.4.

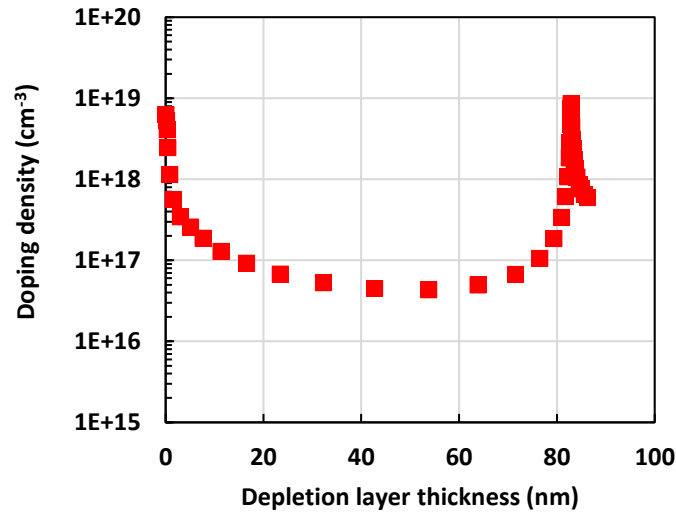


**Figure 4.4 – Doping density  $N_A$  as a function of depletion layer thickness for a P3HT:PCBM MIS capacitor.**

At the edges of the depletion layer, the calculated doping density is influenced by either the semiconductor/insulator interface or by the semiconductor/gold interface, giving values close to 3 orders of magnitudes higher than the actual doping density in the bulk of the semiconductor. As seen in Figure 4.4, the calculated  $N_A$  for the bulk of the semiconducting layer was approximately  $4.5 \times 10^{16} \text{ cm}^{-3}$ , similar to values reported in the literature<sup>8-10</sup>. Nevertheless, since the thickness of the P3HT:PCBM layer here is less than 100 nm, the value of  $N_A$  deduced from Figure 4.4 could be overestimated.

Even though the active layer was a blend of a hole conductor (P3HT) and an electron conductor (PCBM), the device displayed the characteristic behaviour of a p-type semiconductor, with accumulation of holes at negative bias and the formation of a depletion region as the gate voltage starts to become positive. Such performance can be attributed to the choice of the top electrode. The work function of gold matches well with the HOMO of P3HT, making it easier to inject/extract holes from the semiconductor layer. On the other hand, the barrier formed between the LUMO of PCBM and the work function of gold prevents good injection/extraction of electrons.

## 4.2.2 Effect of light

The absorption profile of these materials, both individually and incorporated in a blend are shown in Figure 4.5. The solutions were spin-coated on cleaned glass substrates and compared to a glass reference sample in order to remove the contribution from the substrate. The differences in the absorbance values were mainly due to differences in the thickness of each layer, with a thicker layer being able to absorb a greater part of the incident radiation than a thinner one.

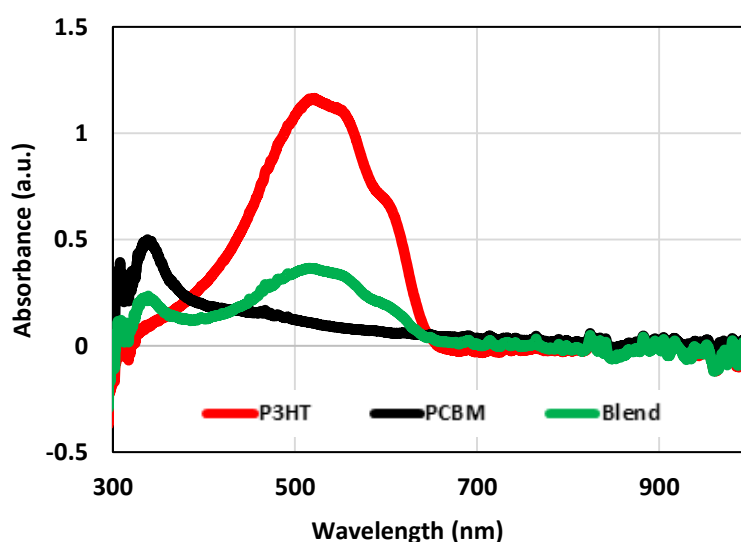


**Figure 4.5 – Absorbance of P3HT (red line), PCBM (black line) and P3HT:PCBM (green line) films.**

As can be seen, the P3HT polymer (red curve) is mainly responsible for the absorption of visible light in the blend, with peak absorption at ~520 nm, followed by two other peaks at ~570 nm and ~610 nm respectively. PCBM mainly absorbs in the UV energy range (black line), with a peak at ~320 nm that extends further in wavelength. When these materials were mixed together, the absorbance of each individual semiconductor added up to form the absorbance of the blend (green line).

As described in Section 2.2.2, when a photon with energy higher than the HOMO-LUMO transition is incident on the blend, an electron is excited to a higher energy level and a neutral entity called an exciton is created. If the exciton dissociates into a free electron and a free hole, these charges can move across the semiconductor bulk to the interface/collection terminal and influence the admittance of MIS capacitors. Due to the low relative dielectric constant of organic semiconductors, the absorption of light does not lead directly to free e/h pairs. The high exciton binding energy provides a barrier that needs to be overcome. If no voltage was applied, the excitons would have to be dissociated by the energetic difference between the  $\text{HOMO}_{\text{P3HT}}$  and  $\text{LUMO}_{\text{PCBM}}$ , as in a bulk heterojunction solar cell. However, due to the applied gate bias, the exciton binding energy barrier is more easily overcome and dissociation can happen even in the absence of an acceptor material<sup>9</sup>.

Figure 4.6 shows the  $C$ - $V$  plot of a P3HT:PCBM-based MIS capacitor, at 1 kHz, when exposed to different light wavelengths. The device was measured inside a cryostat, under vacuum, and light of desired wavelength was provided by a xenon lamp and a monochromator.

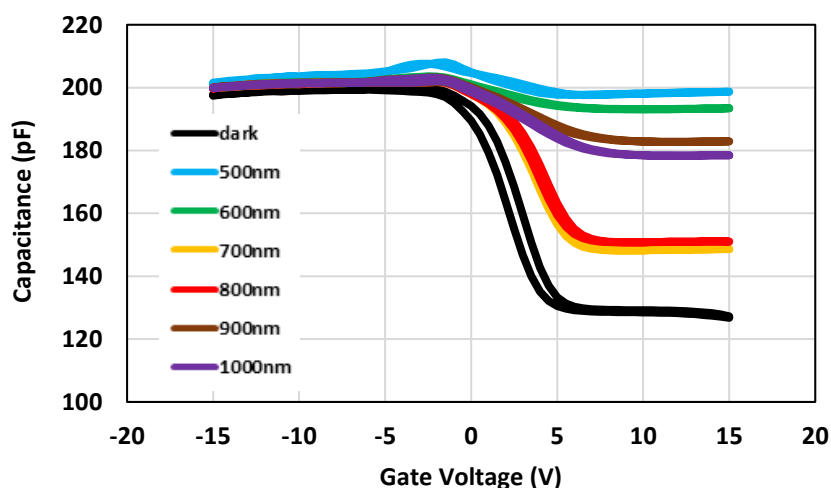


Figure 4.6 –  $C$ - $V$  of P3HT:PCBM capacitors when exposed to different light wavelengths.

Photo-created charges did not influence the measured capacitance by much at negative gate bias. The gate voltage favoured the accumulation of holes at the semiconductor/insulator interface which, during the admittance measurement, would only be seen as the insulator capacitance. However, at positive gate voltages, after dissociation happens, free holes drift to the top electrode, while free electrons were driven to the semiconductor/insulator interface. As demonstrated by Watson and Taylor<sup>11</sup>, some of these electrons fill interface traps, while some remain free and able to follow externally controlled surface potentials as in the charge injection device.

The photo-created electrons present at the interface, either free or trapped will increase the minimum capacitance of the MIS capacitor. Free electrons will partially screen the gate field preventing further increase in the width of the depletion region. If sufficient electrons are being generated, then capacitance becomes independent of applied voltage because any increase in the positive charge on the gate electrode is compensated by free electrons in the inversion layer. On the other hand, trapped electrons will cause a shift in the flatband voltage, as explained in Sections 2.3.4.3 and 2.3.4.5. If the trapping rate is sufficiently high, the shift in flatband voltage will match the sweep rate of the gate voltage<sup>9</sup>, again leading to a minimum capacitance independent of gate voltage. Electron trapping will also lead to counter clockwise hysteresis in the  $C$ - $V$  plot. Interestingly, no hysteresis is observed in Figure 4.6.

Lack of hysteresis usually indicates that no charges were trapped at the semiconductor/insulator interface during the voltage sweep. While this may be possible, a small anti-clockwise hysteresis in the dark  $C$ - $V$  measurement however, suggests that trap sites are present. The lack of hysteresis is most likely due to electron transfer to the PCBM component, as in a solar cell, rather than to interface traps due to imperfections on the PVP surface which can influence the admittance measurement made in the dark.

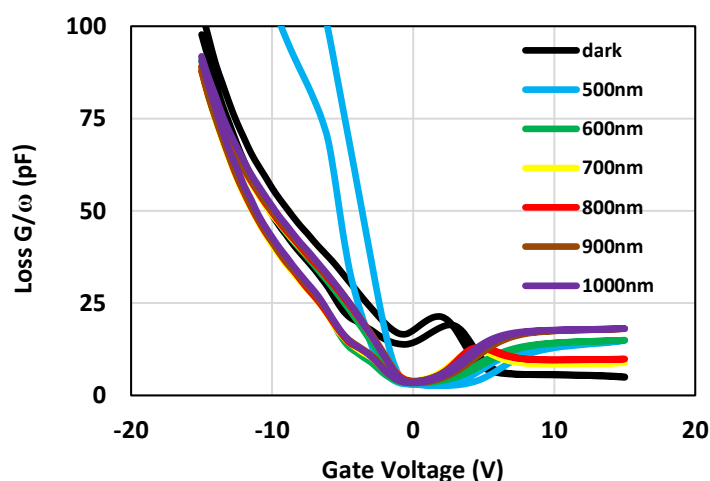
Whichever mechanism is responsible, the minimum capacitance plateau will depend on the rate at which electrons arrive at the insulator interface, which in turn depends on the rate of optical generation and hence absorption spectrum. In Figure 4.6,

---

the highest observed increases in  $C_{\text{MIN}}$  occurred when the device was exposed to 500 nm and 600 nm light and consistent, therefore, with the main absorption band of P3HT (Figure 4.5). When exposed to 700 nm and 800 nm light, a minimal effect was observed, reflecting the weak longer wavelength absorption of the blend.

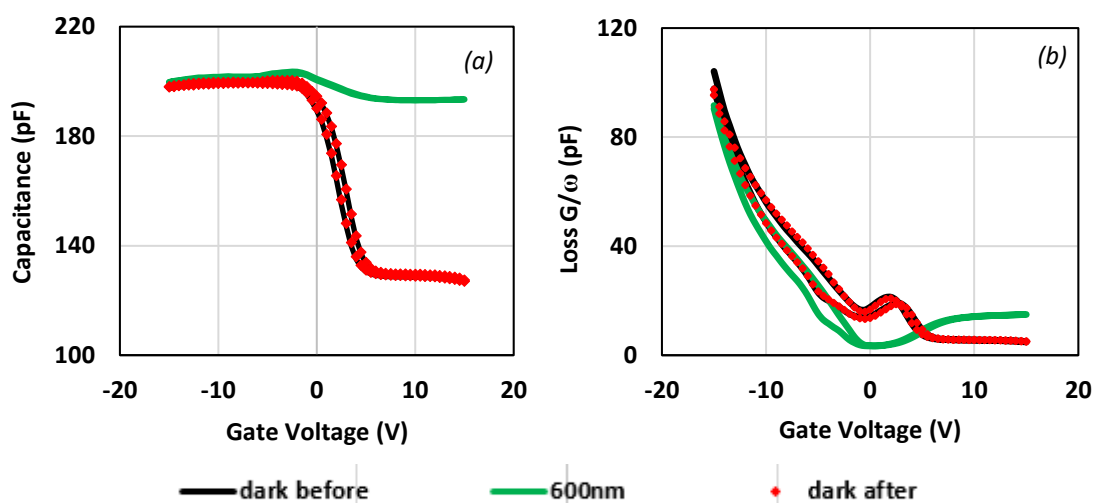
Unexpectedly, a strong capacitance response was observed when exposing the device to 900 nm and 1000 nm light. Dr. Melanie Devynck in our research group was the first to observe this unusual near infrared (NIR) response in MIS capacitors. Apart from a few reports<sup>12,13</sup>, such a response was not observed for this particular polymer:fullerene blend. The effect will be discussed in more detail in the following sections.

Figure 4.7 shows the  $G/\omega$ - $V$  plots obtained when the device was exposed to different light wavelengths. Similar to the  $C$ - $V$  plots, all the illuminated  $G/\omega$ - $V$  curves differ from the one obtained in the dark (black curve). However, the differences in the plots exposed to light are not as evident as in Figure 4.6, with only the 500 nm one being more pronounced. As in the capacitance curves, the positive shift of the loss peak was also related to the presence of electrons at the semiconductor/insulator interface.



**Figure 4.7 – Loss- $V$  of P3HT:PCBM capacitors when exposed to different light wavelengths.**

To make sure all light-induced effects disappeared after each light experiment, an admittance measurement was made, in the dark, immediately after the one exposed to light. Figure 4.8 shows three admittance curves: in the dark before the measurement (black line), the light-exposed measurement (green line) and in the dark immediately after (red rhombus).



**Figure 4.8 – (a) C-V and (b) loss-V of P3HT:PCBM capacitors in the dark before (black line) and after (red rhombus) being exposed to 600 nm light (green line).**

No residual electron trapping in the semiconductor/insulator interface was observed after light excitation, contrary to what has been reported on P3HT-only devices<sup>9,11,14</sup>. The device returned to the original state extremely quickly (i.e. the state prior to light exposure), evidencing the fast transfer processes occurring between the P3HT polymer and the PCBM fullerene. As excitons are dissociated near or at the P3HT/PCBM interface, electrons hop to the fullerene material while holes remain within the P3HT due to the energetic differences in their respective molecular orbitals, which favours such behaviour. The fast recovery shown in Figure 4.8 also highlights the fact that the active layer is indeed a mixed medium of P3HT and PCBM, as in a heterojunction solar cell. If the active layer were segregated into two different vertical phases, electron trapping at the insulator interface would occur more easily, which would then translate as a shift of the flatband voltage of the device after light exposure

is cut off. This is not observed here and so it is concluded that photogenerated electrons remain within the PCBM phase and do not interact with interface electron trap states.

### 4.2.3 Effect of NIR light

Figures 4.6 and 4.7 showed an interesting response of P3HT:PCBM MIS capacitors when exposed to near infrared light (NIR) of 900 nm and 1000 nm. Such a large response was not expected, as these materials are not known to be good absorbers of NIR light. As Figure 4.5 showed, absorption in P3HT ends at ~650 nm while the peak absorption in PCBM is ~320 nm which diminishes gradually into a weak tail at long wavelength. Nevertheless, even with these absorption characteristics being reflected in the blend, the admittance of P3HT:PCBM MIS capacitors was heavily affected when illuminated with NIR light. The use of colour filters during the experiment also rules out the possibility of any absorption of light with harmonic wavelength of  $\lambda/2$  or  $\lambda/3$ .

When exposing a P3HT-only device to different light wavelength, in the visible range,  $C_{MIN}$  increased to a new level according to the generation rate of photo-created electrons (see Figure 4.6). Figure 4.9 shows the increase ( $C_{MIN} - C_{DARK}$ ) in the minimum capacitance, when exposed to wavelengths increasing in 10 nm steps from 400 to 800 nm. In the same figure is plotted the absorption spectrum of P3HT for comparison. To make sure that light did not produce semi-permanent effects, admittance curves were measured before and after the light exposure. If needed, the samples were annealed in vacuum to return the device to its original condition before light exposure.

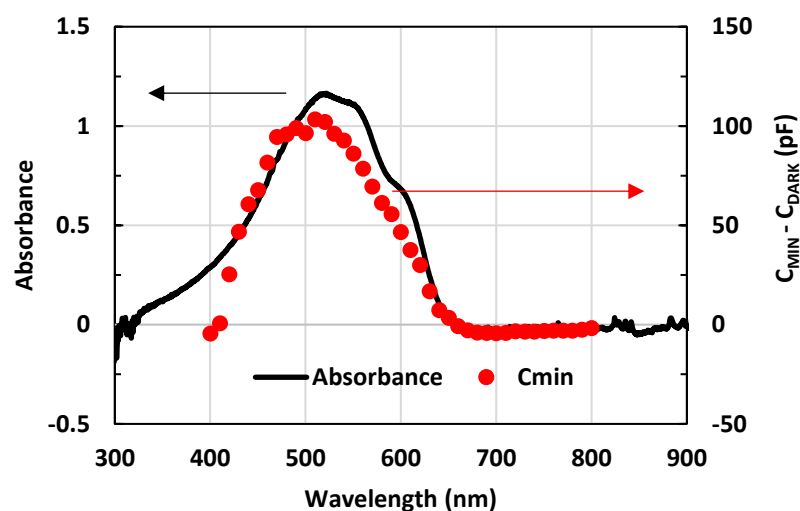


**Figure 4.9 – Absorbance (black line) and shift in minimum capacitance (red dots) of a P3HT-only device exposed to different light wavelength.**

As can be seen, the increase in minimum capacitance follows closely the absorption spectrum of P3HT, rising at 400 nm, peaking at ~520 nm and returning to the dark level at ~650 nm. In the 650-800 nm range, the minimum capacitance maintained its dark value even when exposed to light, following the absorption profile. Although the experiment did not extend further in wavelength, the absorption of NIR light by P3HT films is unlikely, especially when it is noted that the active layer is only a few hundred nanometres thick. To better absorb long wavelength light, the semiconducting layer would have to be much thicker and in the micrometre range.

On the other hand, absorption in PCBM extends to long wavelengths. Figure 4.10 shows a PCBM-only MIS capacitor exposed to different light wavelengths. The device was fabricated using the same procedures described at the beginning of this chapter, with a spin-coated 15 mg/mL solution of PCBM in chloroform, finished with a thermal evaporation of a gold electrode on top.

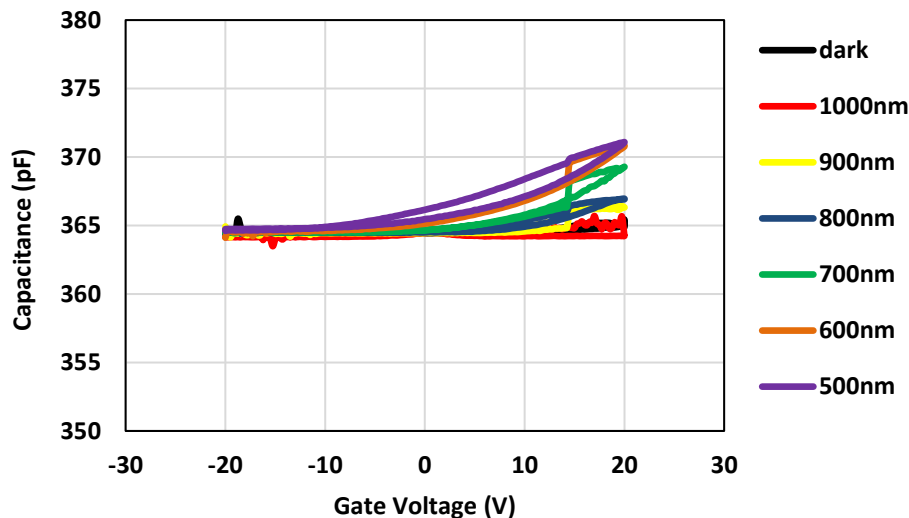


**Figure 4.10 – C-V of a PCBM-only capacitor in the dark and when exposed to different light wavelengths.**

The capacitance curves were dependent on the incident light wavelength. When exposed to 500-800 nm light, the capacitance increased at positive gate voltages, with the largest shifts corresponding to 500 nm and 600 nm light. There was only a minor increase in capacitance when the device was exposed to 900 nm light. However, when exposed to 1000 nm light, the capacitance curve was similar to the one in the dark, indicating that PCBM by itself was not responsible for the sensitivity of the P3HT:PCBM blend in the NIR range seen in Figure 4.6.

To eliminate the possibility that the NIR response arose from the PVP insulating layer, a metal-insulator-metal (MIM) capacitor was fabricated using the same procedures described in Section 4.2.1 in which only PVP was sandwiched between the metal electrodes. The sample was then illuminated with the desired light wavelength and the current through the device was measured using a Keithley 617 programmable electrometer. Figure 4.11 shows the current-voltage ( $I$ - $V$ ) curve of such a capacitor when exposed to different light wavelengths, in a  $10^{-2}$  mbar vacuum inside the cryostat.

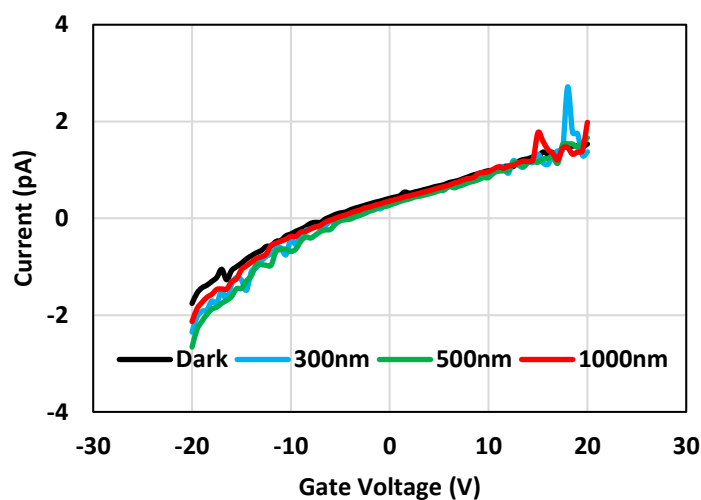


**Figure 4.11 – I-V of a PVP-only MIM capacitor in the dark and when exposed to different light wavelengths.**

The measured current barely changed when illuminated with 300, 500 or 1000 nm light, indicating that light did not excite electrons from PVP insulator states, especially when it was illuminated with NIR light (red curve). A similar experiment was undertaken this time with the blend incorporated. In Figure 4.12, the photoconductive response of the MIS capacitor is represented by the increase ( $I_{ON} - I_{OFF}$ ) in current through the device when illuminated with light in the wavelength range of 400-1000 nm. In each case, the wavelength was incremented in 10 nm steps and relaxation to the dark state checked after each exposure. Each point in Figure 4.12 corresponds to a current-time ( $I-t$ ) experiment (inset), where the MIS capacitor was biased at a fixed gate voltage and the sample was illuminated with light of desired wavelength.

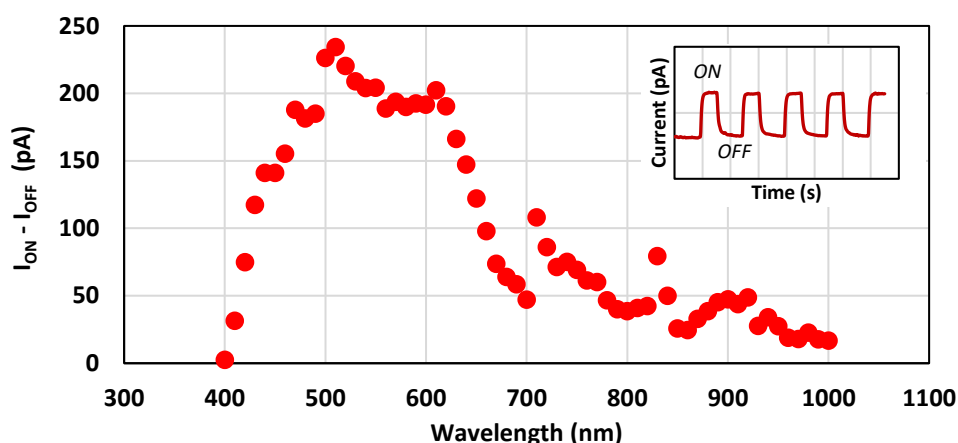


**Figure 4.12 – Shifts in current when a P3HT:PCBM-based MIS capacitor was exposed to different light wavelengths. In the inset, the current-time experiment that originated each point.**

As in the P3HT-only case, the current response followed the blend absorption very well, with a peak of current at  $\sim 510$  nm and  $\sim 610$  nm. The shifts in current decreased as the wavelength increased, but in the 850-950 nm range a small peak, centred at 900 nm is observed. PCBM contributed to some level of absorption in the long wavelength range, possibly providing an increase in current even when absorption in P3HT is negligible. However, if absorption in PCBM was solely responsible for the current shifts, then the shoulder in the 850-950 nm range would not be present, since Figure 4.5 does not display an absorption peak for the fullerene material in that wavelength range. The peaks observed around 710 nm and 830 nm are due to changes in light intensity as the filter used in the experimental setup were changed.

NIR light in the 900 to 1000 nm range corresponds to energies in the range 1.3 eV to 1.2 eV. From the energy scheme of the materials in the device (Figure 4.13), the only two transitions that are of low enough energy to be excited by NIR light seem to be: (a) from the gold Fermi level to the LUMO of PCBM (blue arrow) or (b) the HOMO of P3HT to the LUMO of PCBM (red arrow).

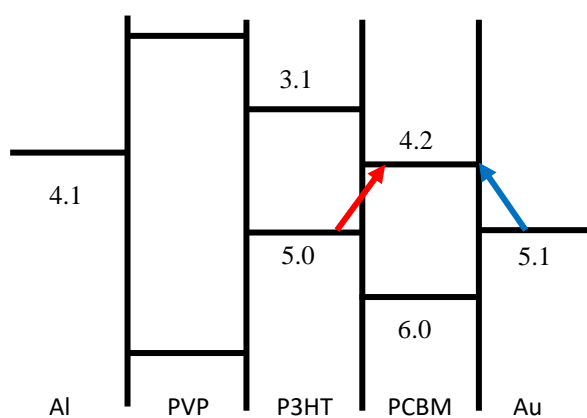


**Figure 4.13 – Energy distribution scheme of a P3HT:PCBM-based MIS capacitor. Approximate values are in eV with respect to the vacuum level.**

The first transition, injection of electrons from gold to PCBM, would be present in Figure 4.10 at a large scale as well, a feature not observed there. The electron injection would also be aided when electric fields reach a critical value at the top electrode. Figure 4.14 and 4.15 shows the current-time experiment for a P3HT:PCBM MIS capacitor when exposed to pulses of 500 nm and 900 nm light at different applied gate voltages.

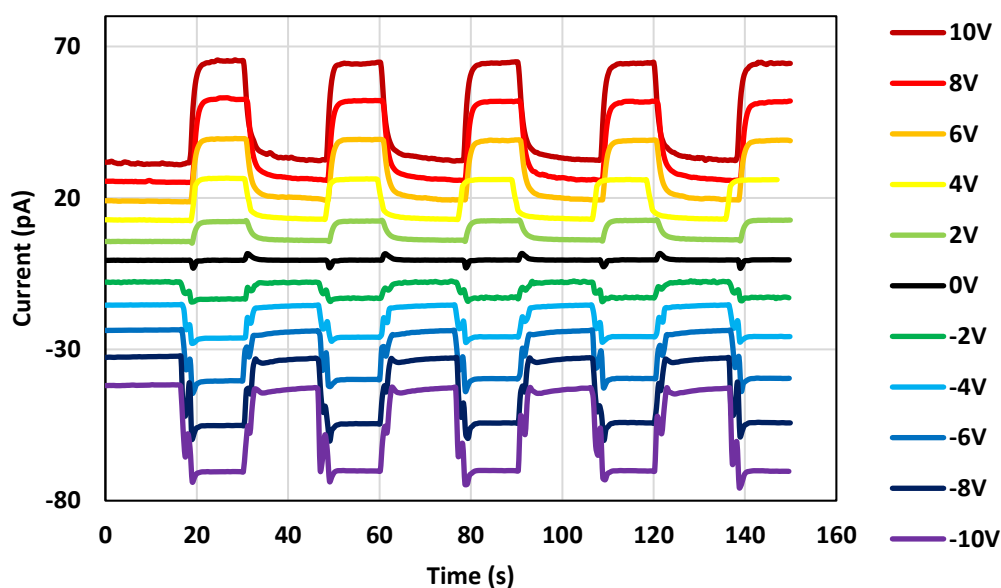


**Figure 4.14 – Current-time of a P3HT:PCBM MIS capacitor exposed to pulses of 500 nm at different applied gate voltages.**

When the device is illuminated, photons are absorbed, the created excitons dissociate and free charge carriers can follow the applied gate voltage. Contrary to the  $C$ - $V$  measurement, where the capacitance did not display significant changes when the device was exposed to light at negative gate voltages, the current through the device increased under illumination, regardless of the gate bias. Figure 4.14 indicates that 500 nm light induced current in the device both in accumulation (-10 V) and in depletion (+10 V). As voltage increases in magnitude, either to positive or negative values, the shift in current, when compared to the dark value, increased as well due to higher exciton dissociation rate at higher voltages.

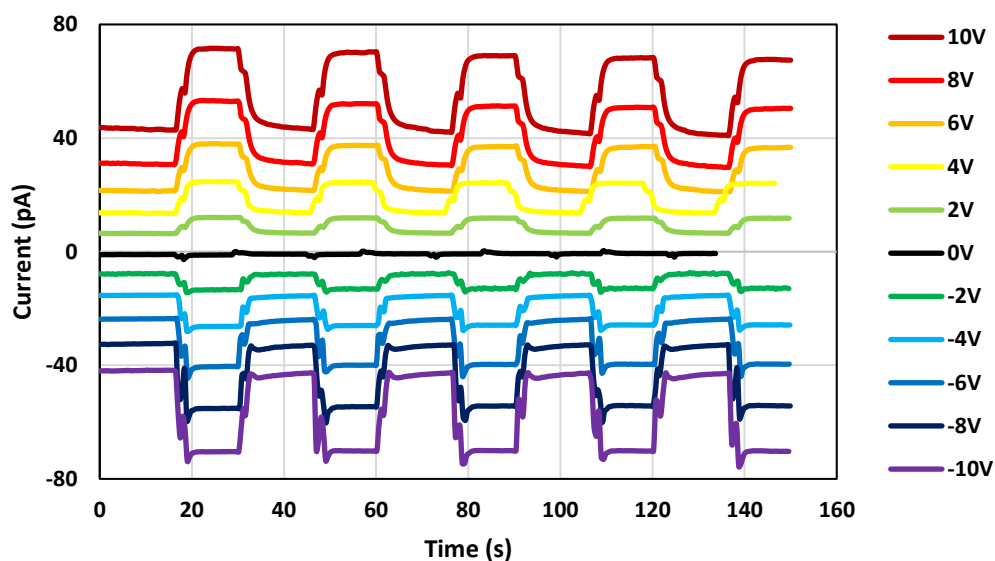


**Figure 4.15 – Current-time of a P3HT:PCBM MIS capacitor exposed to pulses of 900 nm at different applied gate voltages.**

A similar behaviour was seen when the device was exposed to pulses of 900 nm light (Figure 4.15). This points to the fact that the NIR light response is not influenced by electric fields near the top electrode, since it happens at all gate voltages, as in the 500 nm experiment. Current peaks also appeared when the device was biased at 0 V, close to the flatband voltage, when the sample was exposed to both 500 and 900 nm light. The energy differences in the blend materials produced a built-in voltage which was enough to dissociate excitons into free carriers, that quickly recombined, producing the 0 V peaks.

The other possible transition with energy close to 900-1000 nm photons is the one from  $\text{HOMO}_{\text{P3HT}}$  to  $\text{LUMO}_{\text{PCBM}}$ . Such a transition is more often associated with opposite charges injected from the electrodes, for example as in a LED, where electron-hole recombination at the polymer:fullerene interface results in light emission. During this process, a neutral entity, the so-called charge-transfer (CT) state, or exciplex, is formed at the interface that quickly recombines. CT states originate from the overlap of wave functions of the polymer and fullerene component, giving rise to intra-gap states<sup>12</sup>.

If the origin of the NIR sensitivity is due to CT states, then the NIR peak absorption would change as the energies of the materials involved are modified. Changing PCBM with a similar fullerene that has a lower lying LUMO level would push the NIR absorption to longer wavelengths, as the energy difference between  $\text{HOMO}_{\text{P3HT}}$  and  $\text{LUMO}_{\text{fullerene}}$  decreased. Figure 4.16 shows the current response, when the device is illuminated with light of various wavelengths, for a P3HT:M012-based MIS capacitor. M012 is a fullerene similar to PCBM with a lower lying LUMO energy, and was provided by Merck Chemicals Ltd.. The device was fabricated using the same procedures described in Section 4.2 and the current measurement followed the same procedures described earlier in this section.

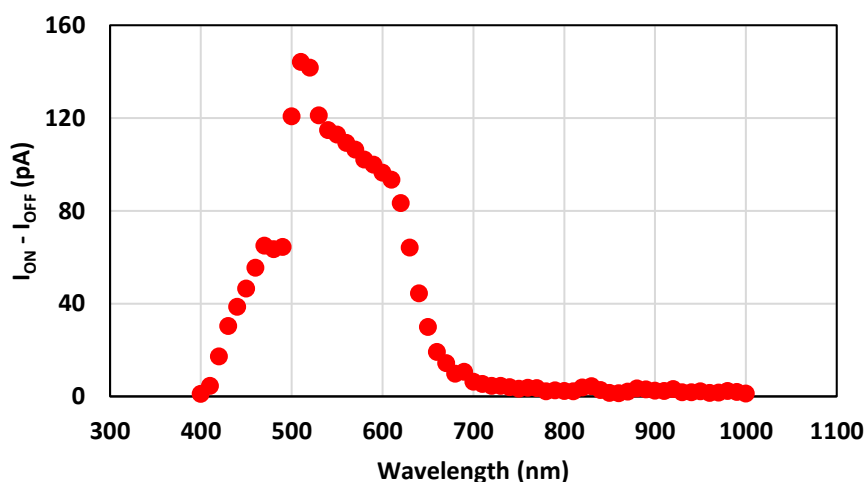


**Figure 4.16 – Magnitude of the current response when a P3HT:M012-based MIS capacitor was exposed to different light wavelengths.**

As with the P3HT:PCBM devices, the increase in current followed the absorption of the blend, peaking between ~500 nm and ~600nm. However, with M012, there was no indication of NIR sensitivity. Changing PCBM with Klook, another Merck provided fullerene with a lower lying LUMO level, resulted in the same behaviour. As Figure 4.17 shows, no NIR sensitivity was observed in P3HT:Klook MIS capacitors.

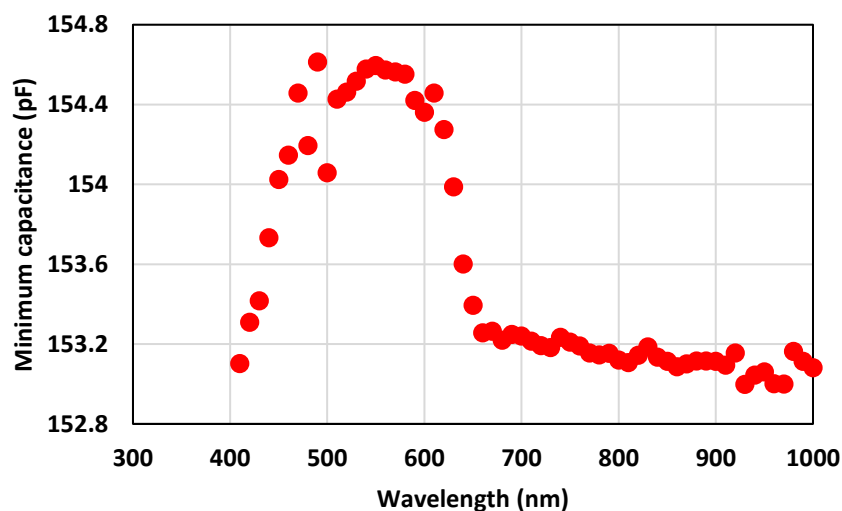


**Figure 4.17 – Minimum capacitance of a P3HT:Klook MIS capacitor when exposed to different light wavelengths.**

The results in Figures 4.16 and 4.17 indicates that the  $\text{HOMO}_{\text{P3HT}}\text{-LUMO}_{\text{fullerene}}$  energy difference, associated with the CT state, plays an important role in the NIR sensitivity of the device. When PCBM was changed with similar fullerene materials with lower lying LUMO levels, the NIR sensitivity was not observed in the 400 to 1000 nm range investigated. A possible explanation is that, since the energy difference is lower, the energy required to excite such a state would also be lower, pushing the NIR sensitivity further in wavelength, outside the range of the experiment. On the other hand, the three different fullerene compounds may have intermixed differently with P3HT, not allowing for a favourable interface between P3HT and the fullerene to be formed.

### 4.3 P3HT:PCBM Charge-Injection-Device

As studied by Watson and Taylor<sup>11</sup>, the magnitude of charge transfer as well as transfer efficiency was low in P3HT-only charge-injection-device (CID), reaching a maximum of ~40%. When an electron acceptor material, like PCBM, is incorporated with P3HT

in a blend, exciton dissociation rate is improved and photo-created charges move more efficiently. These facts suggest that the substitution of P3HT by a blend of P3HT:PCBM should improve the charge transfer efficiency in a CID. To test this hypothesis, the P3HT:PCBM blend was incorporated into a CID (Figure 4.18) and the charge-transfer signal was investigated.

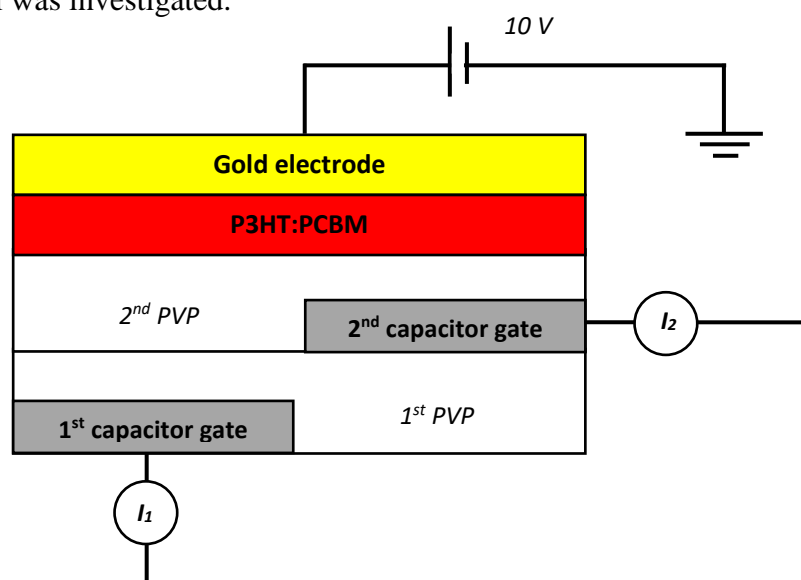


**Figure 4.18 – Structure of a CID based on PVP insulator and P3HT:PCBM blend as active layer.**

The PVP/P3HT:PCBM-based CID was fabricated using the same concentration and procedures described in section 4.2.1 and in the following sequence: first a thin layer of aluminium was thermally evaporated to form the semi-transparent aluminium gate onto which a solution of PVP was spin-coated. After thermal annealing, a thicker layer of aluminium was evaporated to form an opaque 2<sup>nd</sup> capacitor gate electrode and another layer of PVP insulator was spin-coated on top. The P3HT:PCBM blend was then spin-coated on top of the PVP insulating layer and the device was finished with the thermal evaporation of a common gold top electrode.

Biasing the top gold electrode at 10 V induces the formation of a depletion region in both capacitors. Since the insulator in the 1<sup>st</sup> capacitor is thicker, the potential well created in the active layer favours the transfer of electrons from the 1<sup>st</sup> capacitor

to the 2<sup>nd</sup> one, as in Figure 4.19. The photo-induced current in each capacitor as light illuminates only the 1<sup>st</sup> capacitor region is shown in Figure 4.20.

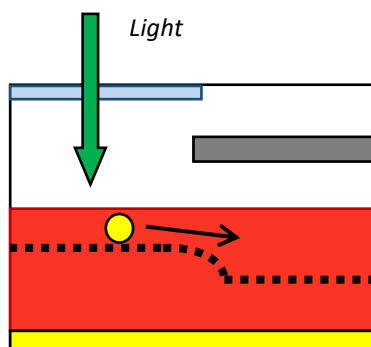


**Figure 4.19 – Transfer of photo-created electrons from the 1<sup>st</sup> capacitor to the deeper potential well beneath the 2<sup>nd</sup> capacitor.**

The charge-transfer efficiency ( $\eta$ ) is then calculated as the transferred/photocreated electrons ratio, measured by the increases in current when light is turned ON.

$$\eta = \frac{I_2}{(I_1 + I_2)} \quad (4.1)$$

where  $I_1$  is the increase in current in the illuminated capacitor and  $I_2$  the increase in current in the 2<sup>nd</sup> capacitor.

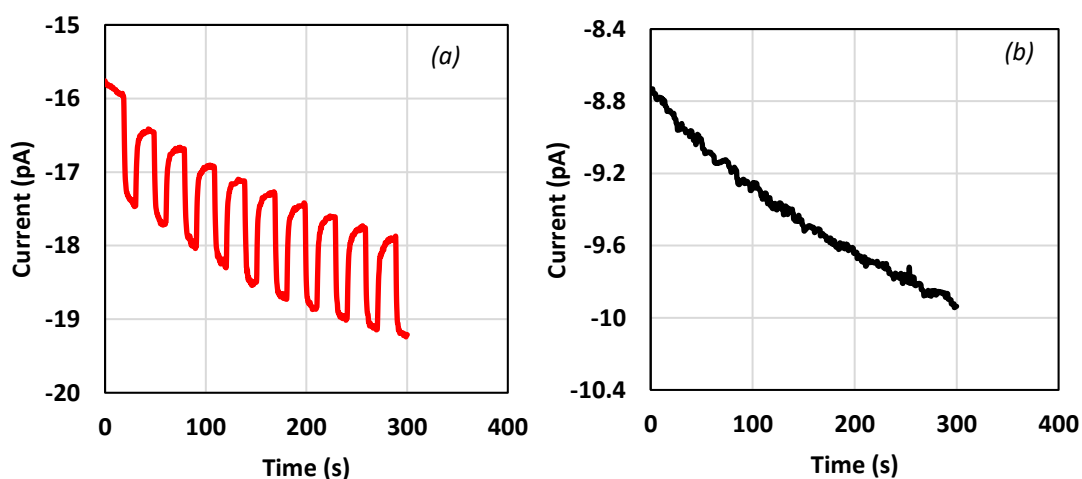


**Figure 4.20 – Current in (a) first and (b) second capacitor as 500 nm light is turned ON/OFF.**

Figure 4.20(a) shows the expected photocurrent response in the 1<sup>st</sup> capacitor. However, no corresponding signal was observed in the 2<sup>nd</sup> capacitor. Although a larger current response was observed in the 1<sup>st</sup> capacitor than in a P3HT-only CID<sup>11</sup>, consistent with a higher photo-generation rate, none of the photogenerated electrons transferred to the 2<sup>nd</sup> capacitor. This suggests that PCBM is present in the P3HT as molecular aggregates. As required in OPVs, these aggregates interlink in such a way as to provide an electron pathway through the film, but do not provide a direct path for electrons to move along the semiconductor/insulator interface.

## CONCLUSION

The admittance of P3HT:PCBM-based MIS capacitors under different light exposure conditions was analysed. Overall, the behaviour followed that of a p-type semiconductor, with accumulation of holes at negative bias and formation of a depletion region with positive voltages. When exposed to light in the visible range, the admittance of the device changed with wavelength, with the shifts in minimum capacitance following the absorption profile of the blend. The device recovered quickly after light exposure, indicating that fast transfer processes between the polymer and the fullerene were in place. The blend also showed some degree of light absorption at the NIR range which was then investigated with the use of different LUMO level PCBM-like molecules. The results indicated that the NIR-absorption was likely to be related to the energy difference between the HOMO of the polymer and the LUMO of the fullerene energy level. When incorporated in a CID, the blend did not display any electron-transfer showing that PCBM aggregated as islands in the P3HT, hindering the charge transport along the semiconductor/insulator interface.

---

## REFERENCES

- 1 A. Ng, X. Liu, W. Y. Jim, A. B. Djurišić, K. C. Lo, S. Y. Li, and W. K. Chan, *Journal of Applied Polymer Science* **131**, n/a (2014).
- 2 O. Ramirez, V. Cabrera, and L. M. Resendiz, in *Optimum ratio of electron-to-hole mobility in P3HT:PCBM organic solar cells*, 2013, p. 55.
- 3 M. T. Dang, L. Hirsch, and G. Wantz, *Advanced Materials* **23**, 3597 (2011).
- 4 W.-H. Baek, T.-S. Yoon, H. H. Lee, and Y.-S. Kim, *Organic Electronics* **11**, 933 (2010).
- 5 A. Tsumura, H. Koezuka, and T. Ando, *Applied Physics Letters* **49**, 1210 (1986).
- 6 H. Sirringhaus, P. J. Brown, R. H. Friend, M. M. Nielsen, K. Bechgaard, B. M. W. Langeveld-Voss, A. J. H. Spiering, R. A. J. Janssen, E. W. Meijer, P. Herwig, and D. M. de Leeuw, *Nature* **401**, 685 (1999).
- 7 S. M. Sze, *Physics of Semiconductor Devices* (John Wiley & Sons, 1981).
- 8 T. Kirchartz, W. Gong, S. A. Hawks, T. Agostinelli, R. C. I. MacKenzie, Y. Yang, and J. Nelson, *The Journal of Physical Chemistry C* **116**, 7672 (2012).
- 9 C. P. Watson, M. Devynck, and D. M. Taylor, *Organic Electronics* **14**, 1728 (2013).
- 10 M. Devynck, B. Rostirolla, C. P. Watson, and D. M. Taylor, *Applied Physics Letters* **105**, 183301 (2014).
- 11 C. P. Watson and D. M. Taylor, *Applied Physics Letters* **99** (2011).
- 12 J.-L. Wu, F.-C. Chen, M.-K. Chuang, and K.-S. Tan, *Energy & Environmental Science* **4**, 3374 (2011).
- 13 C.-M. Yang, P.-Y. Tsai, S.-F. Horng, K.-C. Lee, S.-R. Tzeng, H.-F. Meng, J.-T. Shy, and C.-F. Shu, *Applied Physics Letters* **92**, 083504 (2008).
- 14 D. M. Taylor, J. A. Drysdale, I. Torres, and O. Fernández, *Applied Physics Letters* **89** (2006).

# CHAPTER 5

## DNTT-BASED DEVICES

### 5.1 Introduction

This chapter presents and analyses the experimental results obtained from MIS capacitors and thin film transistors incorporating the organic evaporated small molecule DNTT. Although DNTT has a high hole mobility  $\sim 1 \text{ cm}^2/\text{Vs}$ , because of its large bandgap its absorbance of visible light is poor<sup>1</sup> when compared to more common semiconducting polymers such as P3HT being investigated for organic electronic applications. In this chapter, first the response of MIS capacitors to different ambient conditions, bias stress and light exposure is evaluated.

The latter section of this chapter is concerned with DNTT thin-film transistors fabricated on flexible PEN substrates. These transistors would be used in a dual-gate like structure, as in Figure 5.1, with a light-sensitive capacitor on top of a DNTT-based transistor.

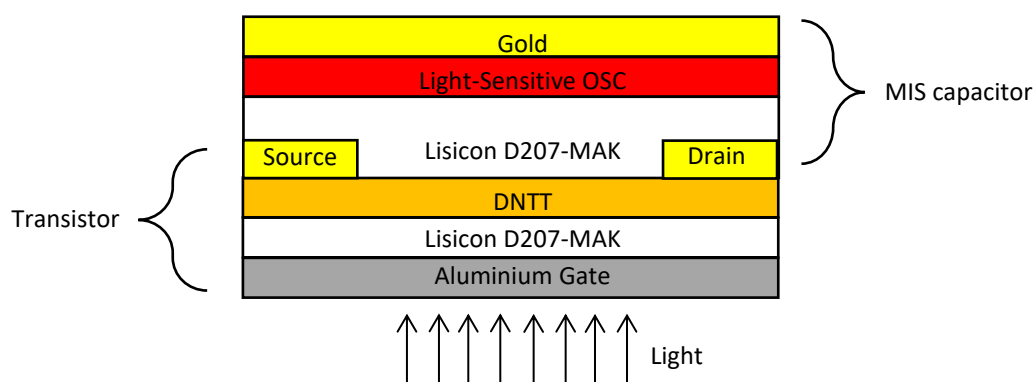


**Figure 5.1 – Dual-gate like structure consisted of an DNTT-based transistor with a blend-based MIS capacitor on top.**

When exposed to visible and/or NIR light, the photo-generated electrons created in the semiconductor blend would accumulate at the blend/insulator interface, inducing a potential across the underlying transistor. This extra potential will shift the threshold voltage to more positive values, as in a dual-gate transistor structure<sup>2</sup> and, if biased accordingly, the MIS capacitor could potentially turn the DNTT transistor into an optical sensor.

Using a similar approach, Tong and Forrest created an integrated organic pixel sensor using a pentacene-based thin film transistor and a separated subphthalocyanine/ $C_{60}$ -based photodetector<sup>3</sup>. However, the performance of the device was limited by the low hole mobility of the pentacene-based transistor ( $\mu \sim 0.09 \text{ cm}^2/\text{Vs}$ ) and by the low EQE (external quantum efficiency) of  $\sim 15$  to  $20\%$  in the 500-600 nm range.

By incorporating a P3HT:PCBM MIS capacitor with a DNTT-based transistor in a vertical stack, the concept presented in this chapter would have a wider range of light absorption, extending to the NIR region, and a better overall performance. In this chapter, DNTT MIS capacitors and transistors were analysed at different ambient conditions.

## 5.2 DNTT-based MIS capacitors

### 5.2.1 Overall behaviour of DNTT-based capacitors

As discussed in Chapters 2 and 4, small-signal admittance analysis of MIS capacitors has been widely used to probe interface states in silicon devices, with the advantage of also providing a direct measurement of the insulator thickness. Apart from a few reports<sup>4,5</sup>, the use of DNTT has not been investigated in MIS capacitors. As shown by Hayashi *et al*<sup>5</sup>, the admittance of the device can be influenced by areas of DNTT not covered by the top electrode. When the measurements are performed at low frequencies ( $\sim 10^0$ - $10^1$  Hz), as discussed in Section 2.3.4.5, charge carriers can drift and diffuse into uncovered areas, resulting in energy losses in the device<sup>6</sup>. However, no investigations on the behaviour of DNTT-based MIS capacitors under different ambient conditions have been reported.

In this section, the effects of light, air and vacuum, measurement frequency, temperature and bias stress on the electrical behaviour of DNTT-based MIS capacitors were investigated. The device structure is shown in Figure 5.2 and consisted of an aluminium gate electrode, a polystyrene insulating layer, evaporated DNTT and gold as the top electrode. Glass slides used as substrates were cleaned using standard procedures described in Section 3.3.1. A thin layer ( $\sim 10$  nm) of aluminium was thermally evaporated to serve as a semi-transparent gate electrode. A solution of polystyrene (PS) in toluene (4.5 wt %) was spin-coated on top of the gate to form the insulating layer. Thermal annealing of the sample was performed at 110 °C for 10 minutes in order to remove remaining solvent. DNTT was then thermally evaporated through a shadow mask and, without removing the sample, gold was evaporated as an injection electrode. The same mask was used to avoid any lateral conduction effects.

All electrical characterization was carried out using a precision LCR meter (HP 4284A). C-V plots were first obtained at 1 kHz with an AC signal amplitude of 100 mV with the bias voltage stepped in 0.5 V increments at a sweep rate of 0.2 V/s. During the

light experiments, MIS capacitors were illuminated through the thin Al gate electrode with monochromatic light provided by a xenon lamp. To make sure that light-induced processes had already fully developed, the device was soaked with light for 30 min before the measurement.

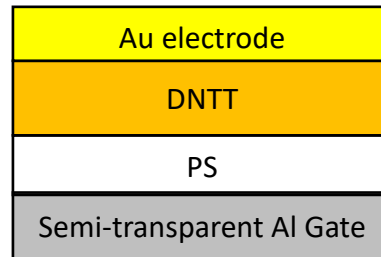


**Figure 5.2 – Device structure of DNTT-based MIS capacitor.**

The capacitance-frequency ( $C$ - $f$ ) and loss-frequency ( $G/\omega$ - $f$ ) of DNTT-based MIS capacitor in the dark at different applied gate voltages are shown in Figure 5.3 *a* and *b* respectively. Over the frequency range  $10^2$  -  $10^5$  Hz, the capacitance and loss characteristics were dependent on the applied gate voltage. At high negative voltages (black line), the capacitance decreases from  $\sim 155$  pF at  $10^2$  Hz to  $\sim 135$  pF at  $10^5$  Hz. As the voltage increases towards positive values, the maximum capacitance decreases to 133 pF at 0 V (green line). For positive voltages, the capacitance remains constant over the whole frequency range. These shifts are consistent with the formation of a conventional depletion region inside the semiconductor<sup>7</sup>, as described in Section 2.3. The  $G/\omega$ - $f$  plot displays a loss peak centred at  $\sim 3$  kHz that gradually decreases as the gate voltage increases. The increase in loss at  $10^5$  Hz is most likely due to contact resistance effects, as described in section 2.3.4.1.

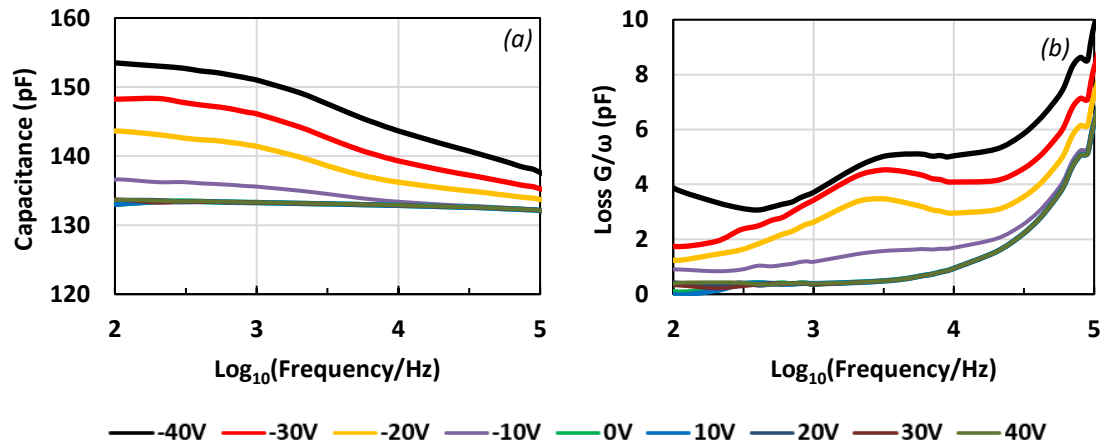


**Figure 5.3 – Frequency dependence of (a) capacitance and (b) loss ( $G/\omega$ ) of DNTT-based MIS capacitors measured in the dark, in air with different applied gate voltages.**

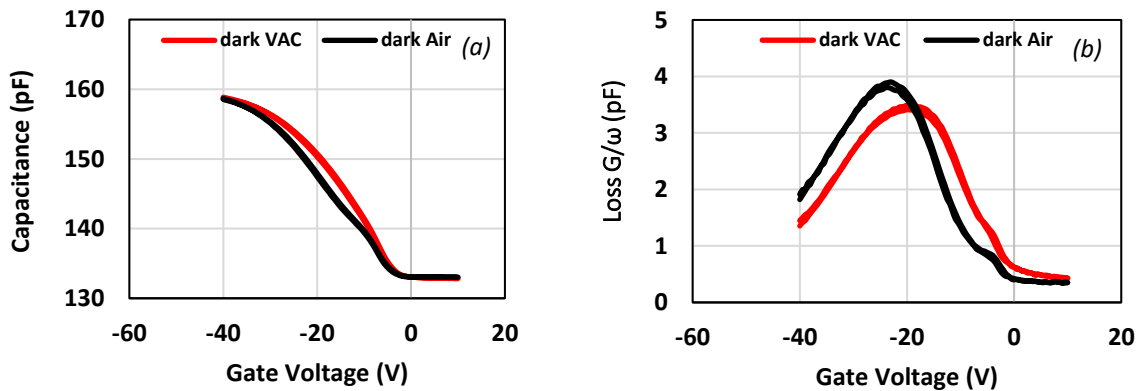


**Figure 5.4 – (a)  $C$ - $V$  and (b)  $loss$ - $V$  plots of a DNTT MIS capacitor measured in the dark in air (black) and in vacuum (red) at 1 kHz.**

The same device was used to measure the dark  $C$ - $V$  and  $loss$ - $V$  behaviour at 1 kHz, in air (first) and then under vacuum, see Figure 5.4. The vacuum plot was obtained after leaving the device under a vacuum of  $10^{-2}$  mbar for at least 30 minutes. As in Figure 5.3, the device displays the overall behaviour of a p-type semiconductor MIS capacitor, with accumulation of holes at negative bias and formation of a depletion region as the bias voltage becomes more positive. Both  $C$ - $V$  plots are similar but the one under vacuum is smoother and did not display the shoulder at around -10 V.

However, the  $loss-V$  plots showed the presence of a peak in both measurements corresponding to the -10 V shoulder in Figure 5.4a indicating that exposure to laboratory air was not responsible for this feature. The main loss peak in the vacuum measurement shifted to more positive voltages and became broader when compared to the one exposed to air. When illuminated with 360 nm light, the  $C-V$  characteristics showed different behaviour when the device was in air compared to when it was under vacuum, as shown in Figure 5.5.

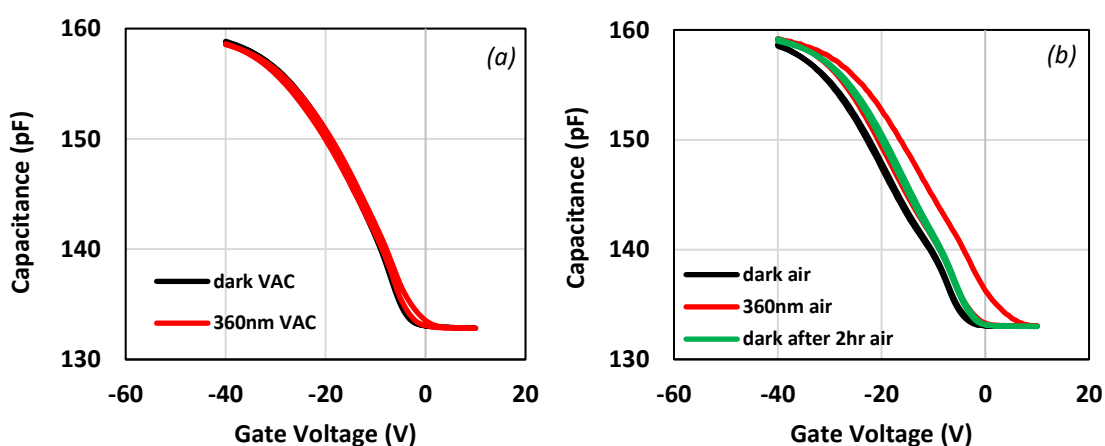


**Figure 5.5 –  $C-V$  plots for DNTT-based MIS capacitors (a) under vacuum and (b) in air when in the dark and exposed to 360 nm light.**

While under vacuum, light had little or no effect on the  $C-V$  behaviour of DNTT-based MIS capacitors. On the other hand, when the device was exposed to laboratory air, light produced a hysteresis effect owing to a positive shift in the flatband voltage. Interestingly, the minimum capacitance was not affected by light, contrary to observations in polymer-based MIS capacitors<sup>8-10</sup> (as in Figure 4.6). A low population of photo-excited electrons at the semiconductor/insulator interface could explain why the minimum capacitance was not affected and, in fact, when compared to P3HT, DNTT has a weak absorption of visible light. Thus, only a small number of electrons would be excited.

Environmental studies on the operation of DNTT transistors have been reported in the past<sup>11</sup> showing that the combination of light plus air induces a positive shift in the turn-on voltage, without changing the shape of the transfer plot. The present MIS result is consistent with the aforementioned results, showing that light by itself is not responsible for the observed hysteresis in DNTT MIS capacitors. Interestingly, hysteresis still occurs after ceasing the light exposure but disappears within 2 hours, leaving only a residual voltage shift. Photo-created electrons, once at the semiconductor/insulator interface, can become trapped at the interface or in insulator states<sup>12</sup> and, once light exposure is cut off, these electrons remain partially screening the semiconductor layer and producing a shift in the flatband voltage until they disappear.

To provide more insight into what is happening in these DNTT devices, a series of  $C$ - $V$  measurements was made, under light exposure in air, but with different end voltages (Figure 5.6).

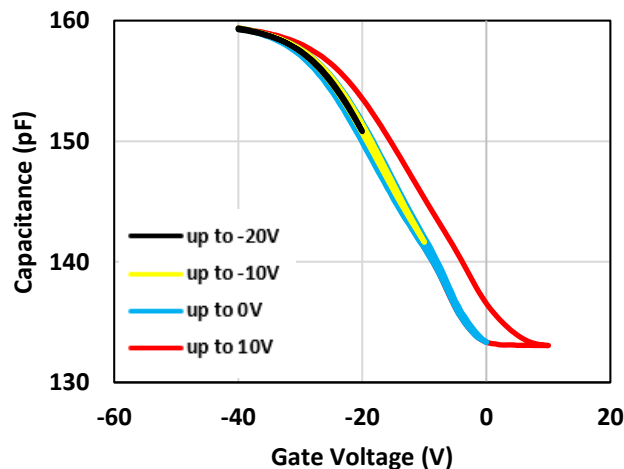


**Figure 5.6 –  $C$ - $V$  plots for a DNTT MIS capacitor under 360 nm light exposures showing the effect of voltage scan range.**

When the voltage sweep ends at -20 V, -10 V and 0 V, no hysteresis effect was observed. Hysteresis only appeared when the device was biased to a voltage corresponding to full depletion (red curve). The complete lack of hysteresis when the device was under vacuum suggests that a component of laboratory air is responsible for it. As described in Section 2.3.4.3, hysteresis can arise from a positive shift in the

flatband voltage when photo-induced electrons become trapped at the semiconductor/insulator interface. If the photo-induced electrons originated either from the air-related states in the bulk semiconductor or from direct photon excitation, then hysteresis should be observed even during partial voltage sweeps. That hysteresis was observed only when the device was in full depletion, is evidence that electrons are photo-injected from the gold electrode when the electric field there attains some critical value. A possible explanation is that a component of laboratory air provides an intermediate energy state that encourages electron injection from the top electrode. This being the case, DNTT transistors could be prone to photo-induced electron injection when operating under illumination in air.

## 5.2.2 Effect of Measurement Frequency

To further investigate the effect of frequency on the C-V characteristics, 2 mm<sup>2</sup> PS/DNTT capacitors were fabricated using the procedures as in Section 5.2.1. DNTT and Au were thermally evaporated using the same masks to minimize lateral conduction effects. C-V and loss-V measurements were made as a function of frequency, in air, in the dark and are shown in Figure 5.7.

At high frequencies, the device displayed a shoulder at around -10 V in the C-V measurements. As frequency decreased, however, the shoulder was lost with the accumulation-depletion transition dominating the whole characteristics. At the highest frequencies, the loss peaks also display a weak feature at around -10 V. As the frequency decreases, both the main peak and the weak feature decreased in magnitude, the latter disappearing at the lowest frequency. The main loss peak increased in magnitude and shifted to higher negative voltages as the frequency increased, a characteristic feature of a distribution of interface states<sup>6,10,13</sup>. As discussed in section 2.3.4.4, interface states give rise to energy levels within the semiconductor band gap and can contribute to the admittance of MIS devices. At low frequencies, the occupancy of these states can follow the applied AC signal and do not contribute to energy loss.

At very high frequencies, these states cannot respond at all, so no loss is seen. However, as the applied frequency gets closer to the capture and emission rate of the interface states, their response lags behind the AC signal, becoming a source of energy loss. The rate at which these states are occupied/unoccupied depends on the availability of majority carriers at the interface, which is determined by the applied gate voltage. Hence, as the measurement frequency changes, the loss peak will occur at different applied voltages.

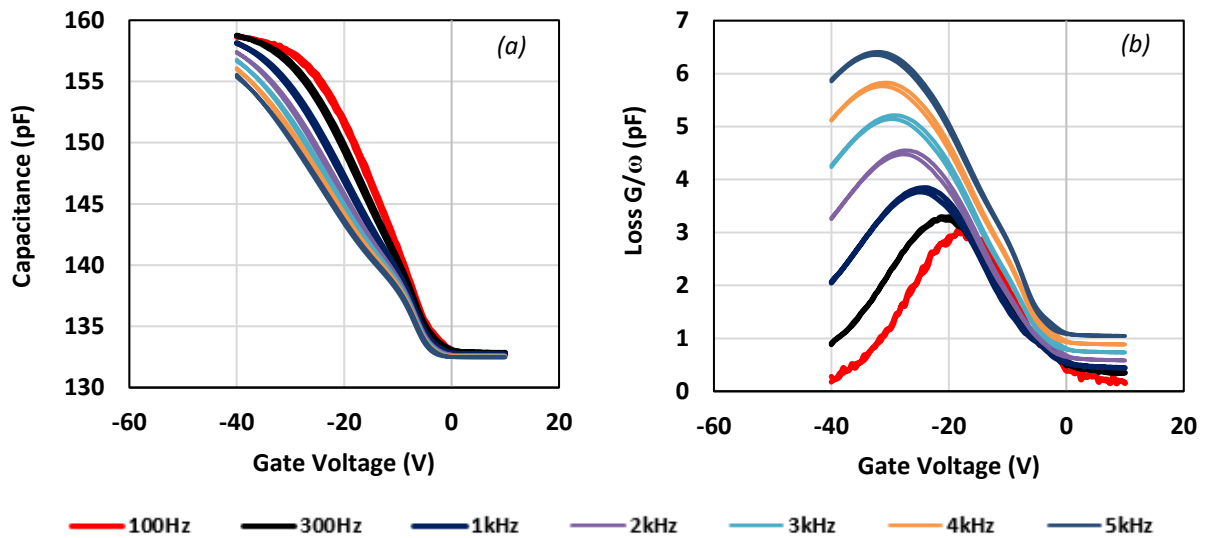


**Figure 5.7 – (a) Capacitance and (b) loss plots obtained in air for different applied AC signal frequencies.**

### 5.2.3 Effect of Temperature

The C-V and loss-V behaviour of DNTT MIS capacitors were also investigated in air for a range of different temperatures. The samples were held at each temperature for at least 30 minutes before the respective curves were obtained. It has been shown that the charge carrier mobility in single crystal DNTT-based transistors increases from  $8 \text{ cm}^2/\text{Vs}$  at 200 K to  $10 \text{ cm}^2/\text{Vs}$  at 270 K and then decreases to  $7 \text{ cm}^2/\text{Vs}$  at 300 K, remaining quite stable in the 200-300 K range<sup>14</sup>. This stability also occurs with

transistors made with evaporated DNTT, where the hole mobility remains approximately equal to  $1 \text{ cm}^2/\text{Vs}$  in the 293-363 K temperature range<sup>15</sup>. The mobility values obtained in those works are due to currents flowing parallel to the semiconductor/insulator interface, while the direction of charge movement during the admittance measurements is perpendicular to that interface. However, the evidence that temperature does not influence DNTT devices by much is important, as long as the material does not degrade.

As seen in Figure 5.8 *a* and *b*, when measurements were made at 300 Hz, temperatures in the 290-340 K range had virtually no effect. As the temperature increased, a small increase occurred in the accumulation to depletion transition slope which was accompanied by a slight narrowing of the loss peak.

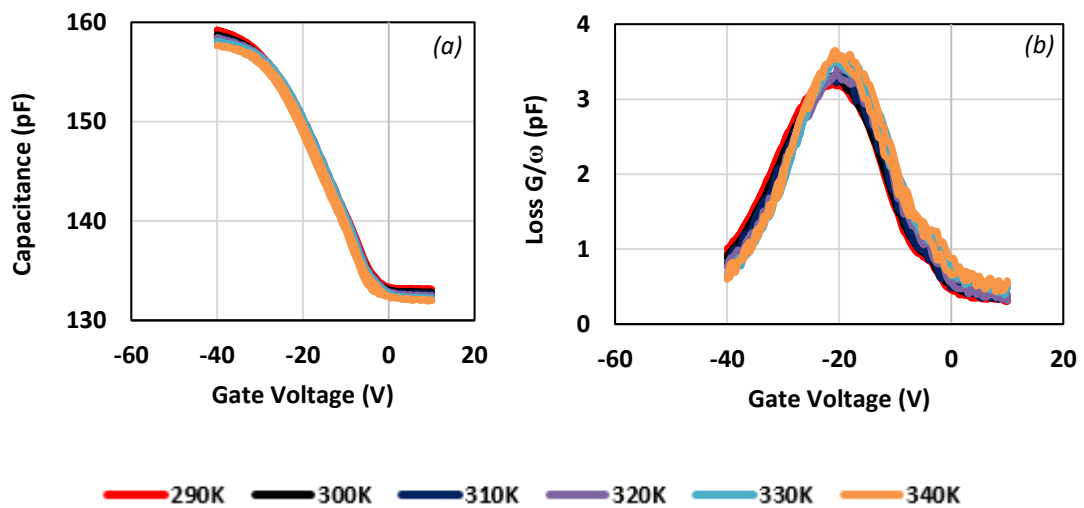


**Figure 5.8 – Effect of temperature on (a) C-V and (b) loss-V plots of a DNTT MIS capacitor when measured at 300 Hz in air.**

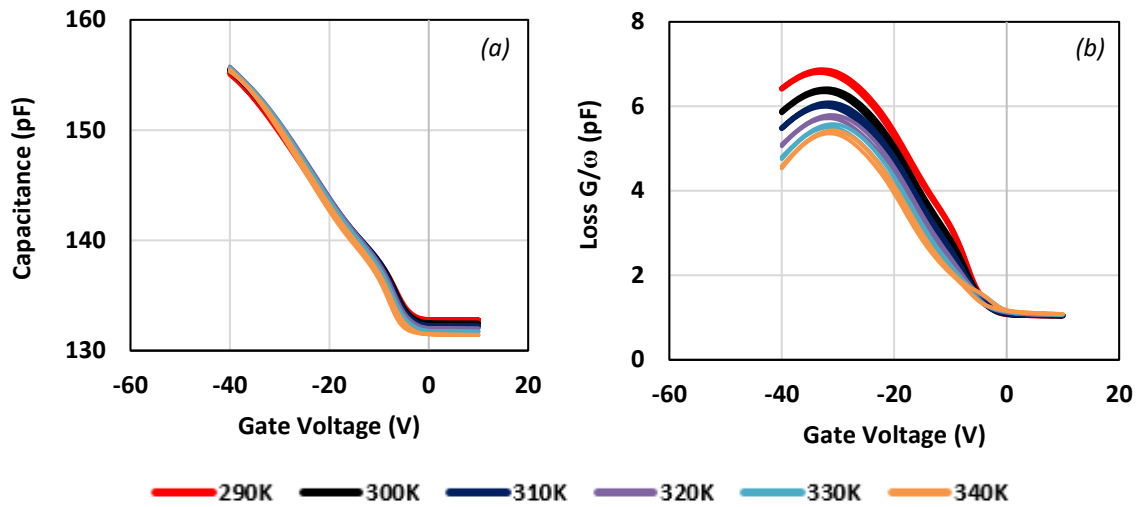


**Figure 5.9 – Effect of temperature on (a) C-V and (b) loss-V plots of a DNTT MIS capacitor when measured at 5 kHz in air.**

Figure 5.9 shows that when the small signal frequency was increased to 5 kHz, the magnitude of the loss peak decreased with increasing temperature, but little effect was seen in the C-V plot. If an increase in temperature translates to a decrease in the bulk resistance,  $R_B$ , of the semiconductor, then as the temperature increases the C-V and  $G/\omega$ -V plots would respond accordingly. Using equations 2.16 and 2.17, the effect of changing  $R_B$  in an ideal MIS capacitor may be simulated. The result is shown in Figure 5.10. As the bulk resistance decreases, the relaxation time  $\tau_R$  becomes shorter and the loss peak shifts to higher frequencies but maintains the same magnitude. In Figure 5.9b, however, the loss peaks decrease in magnitude as the temperature increases, a feature which cannot be explained by a decrease in the bulk resistance with temperature and cannot be attributed, therefore, to majority carrier energy loss.

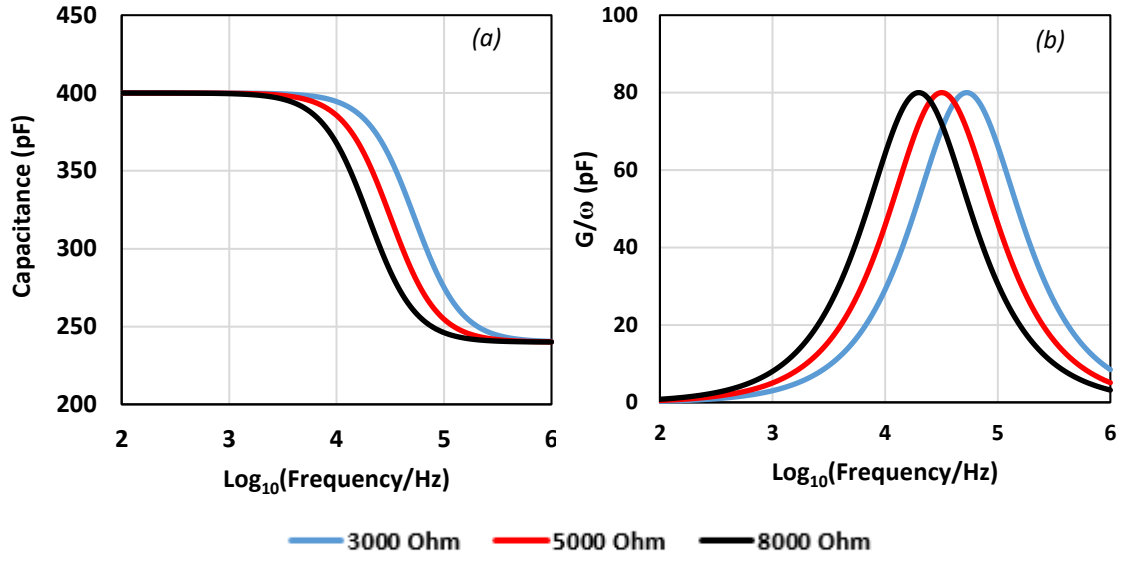


**Figure 5.10 – Simulations showing the effect of changing bulk resistance on the (a) C-f and (b) loss-f plots in an ideal MIS capacitor. Semiconductor layer thickness used was 200 nm,  $C_I = 400$  pF and  $C_B = 600$  pF.**

As mentioned in the previous section, the observed loss peaks are a result of interface states being occupied/unoccupied. This being the case, as temperature increases, the interface states probed at a particular frequency will be deeper in energy, requiring a higher voltage to shift the Fermi level at the interface deeper into the gap.

As a first approach, one can estimate the interface hole trap density ( $D_{it}$ ) from the loss-V peaks in Figure 5.9b, using<sup>16</sup>:

$$D_{it} = \frac{2}{qA} \left( \frac{G_{max}}{\omega} \right) \left[ \left( \frac{G_{max}}{\omega C_I} \right)^2 + \left( 1 - \frac{C_{max}}{C_I} \right)^2 \right]^{-1} \quad (5.1)$$

where  $q$  is the electronic charge,  $A$  the device's area,  $G_{max}/\omega$  the maximum value of the loss peak and  $C_{max}$  its corresponding capacitance and  $C_I$  the insulator capacitance, estimated from the accumulation value in the 100 Hz C-V curve. The estimated values of  $D_{it}$  as a function of temperature are presented in Figure 5.11 below:

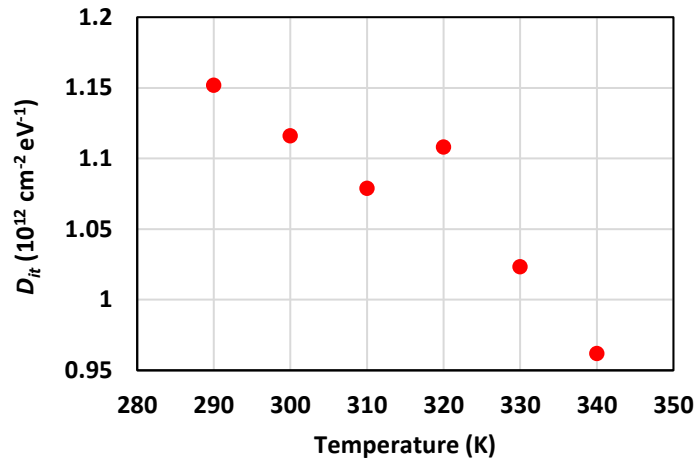


**Figure 5.11 – Estimated value of interface trap density as a function of temperature for DNTT-based MIS devices in air in dark.**

The estimated interface trap density is one order of magnitude higher than the usual values obtained for organic MIS capacitors<sup>13,16</sup>. The density of trap states at the interface usually decreases into the bandgap and, for a particular measurement frequency, as temperature increases additional voltage is required to probe the interface states of the same energy, explaining the decrease in  $D_{it}$  as temperature increases.

#### 5.2.4 Effect of Light

When exposed to light, the flatband voltage of DNTT devices tends to shift to more positive values. As explained previously, this effect is normally associated with the creation of photoinduced electrons within the semiconductor depletion region migrating to and becoming trapped at the semiconductor/insulator interface<sup>9</sup> (see Section 2.3.4.3). However, as explained in section 5.2.1, in DNTT devices, the light-induced flatband shift only appears when the electric field at the top electrode exceeds some critical value and when the device is exposed to air. In this section, we further explore the effect of light on DNTT-based MIS capacitors. Admittance measurements were made in air with a 300 Hz AC signal frequency.

Figure 5.12 shows that when exposed to long wavelength light in the 600-1000 nm range, the admittance of DNTT-based MIS devices does not change. Both the C-V and loss-V plots are identical to the one in dark.

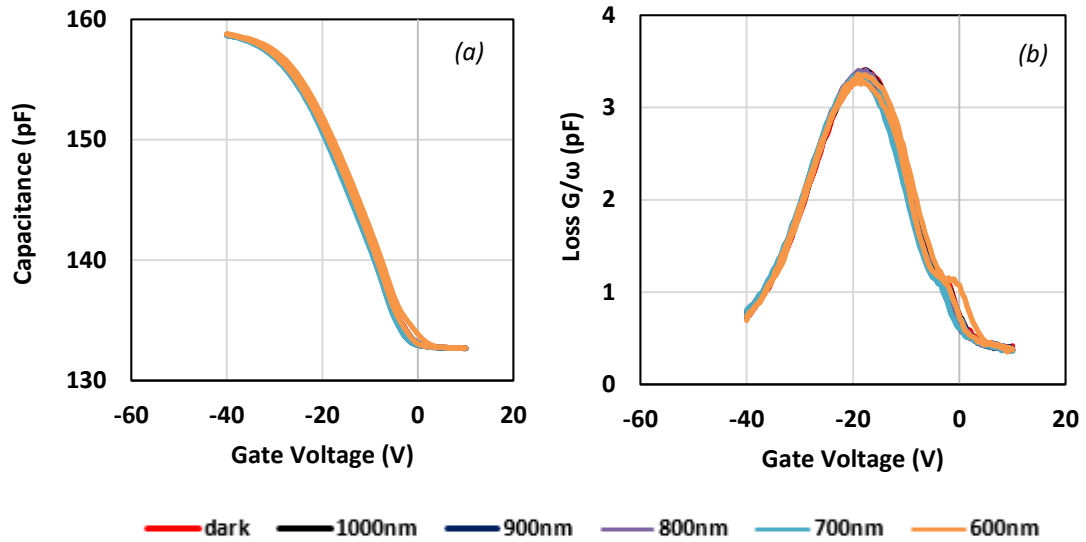


**Figure 5.12 – Effect of long wavelength light, in air, on (a) C-V and (b) loss-V of DNTT MIS capacitors.**

The lack of response in the 600-1000 nm range follows the absorption profile of DNTT<sup>1</sup> and would allow for NIR light to enter the light-sensitive blend in the device concept described in the introduction to this chapter.

In Figure 5.13 however, when the DNTT capacitors were exposed to light of 500 nm wavelength, the whole C-V and loss-V plots shifted to more positive values as time passes. The loss peaks become slightly narrower, indicating that the accumulation-depletion transition slope becomes slightly steeper with time of exposure. A small anti-clockwise hysteresis also appeared in all of the light exposed plots. A similar, but more pronounced, effect happens when the device is exposed to 400 nm light for about two hours (Figure 5.14).

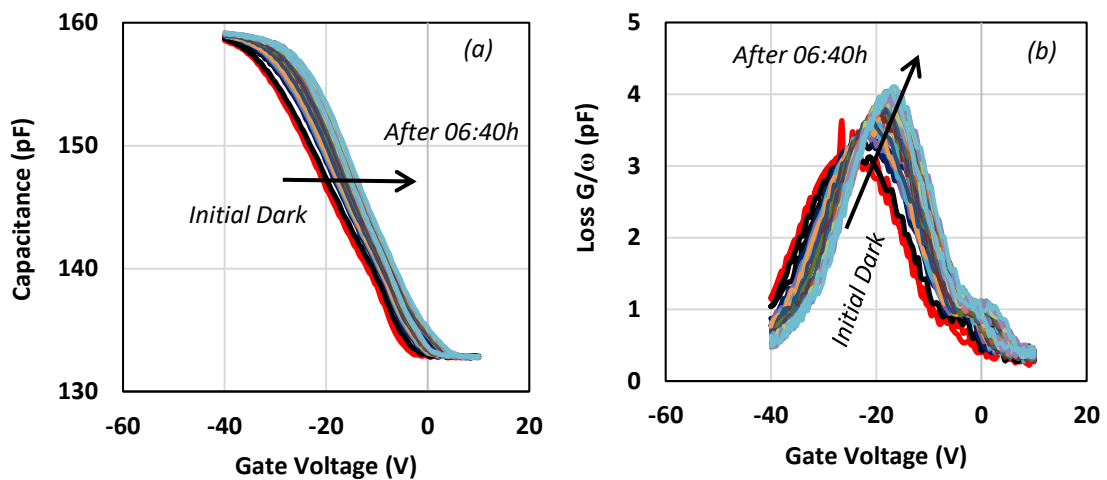


**Figure 5.13 – Effect of 500 nm light soaking in air on the (a) C-V and (b) loss-V of DNTT MIS capacitors over a period of roughly 7 hours.**

Leaving the sample exposed to 500 nm light for almost 7 hours induced changes in the admittance behaviour of the MIS capacitor. This could be due to DNTT degradation over time with light exposure. It has been shown, however, that DNTT transistors are exceptionally stable, even over a period of 9 months of storage in ambient light in air<sup>11</sup>. As demonstrated by Ding *et al*<sup>11</sup>, the transistors stored in light in air had improved charge carrier mobilities, a feature that the authors attributed to a light-assisted oxygen doping effect. In Figure 5.12a, however, the C-V curves become steeper as time passes and, assuming that DNTT is an already doped p-type semiconductor, that would mean that the doping density is decreasing as time passes, in contrast to the Ding *et al* explanation. Based on the result of Figure 5.6, it may be that the combination of light plus air could be facilitating the injection of electrons through the introduction of new energy levels in the semiconductor band gap, near the top electrode, explaining the positive shift as time passes.

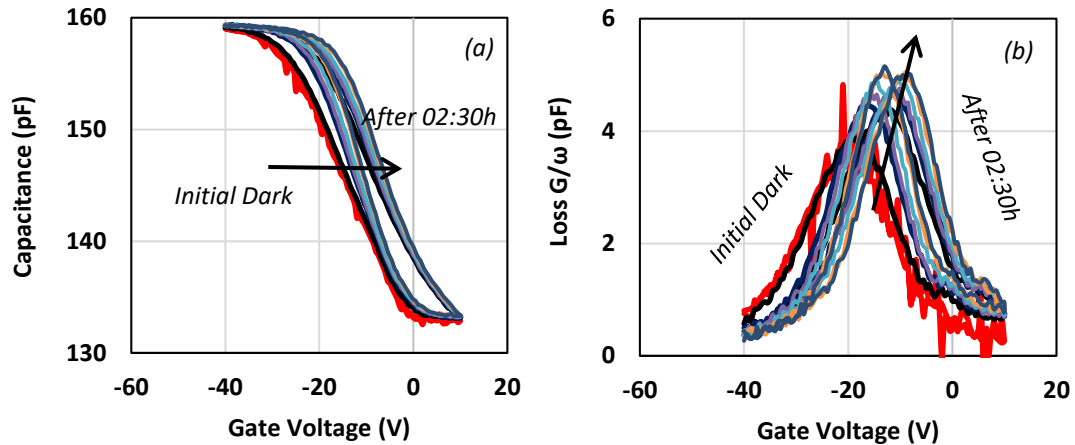


**Figure 5.14 – Effect of 400 nm light soaking in air on the (a) C-V and (b) loss-V of DNTT MIS capacitors over a period of roughly 2 and a half hours.**

Milvich *et al* reported a continuous threshold voltage ( $V_{TH}$ ) shift in the transfer curves of DNTT-based transistors when illuminated with 461 nm light<sup>1</sup>, similar to the one observed in Figure 5.13 and 5.14. However, the observed  $V_{TH}$  shift saturated at a much faster time scale ( $\sim 5$  min) than the MIS capacitor ones. The authors attributed the threshold voltage shifts to the presence of photo-generated electrons trapped near/at the DNTT/ $\text{AlO}_x$  interface. In contrast to the discussion in the previous sections, the authors credited the creation of electrons to photon absorption in the semiconductor layer and not to light-assisted electron injection. Milvich *et al* also observed that the transistor could be reset to its original  $V_{TH}$  after applying a  $V_{GS}$  of  $-3$  V for several minutes<sup>1</sup>. The same relaxation is reflected in the admittance curves of MIS capacitors when the illumination is cut off (Figure 5.15).

After ceasing the light exposure, the recovery of the device in the dark was only partial, as shown in Figure 5.15a and b. After 15 hours, the curves retracted a little, showing that light had a semi-permanent effect on the DNTT-based MIS capacitors. Hysteresis also disappeared after ceasing light exposure, following the behaviour in section 5.2.1.

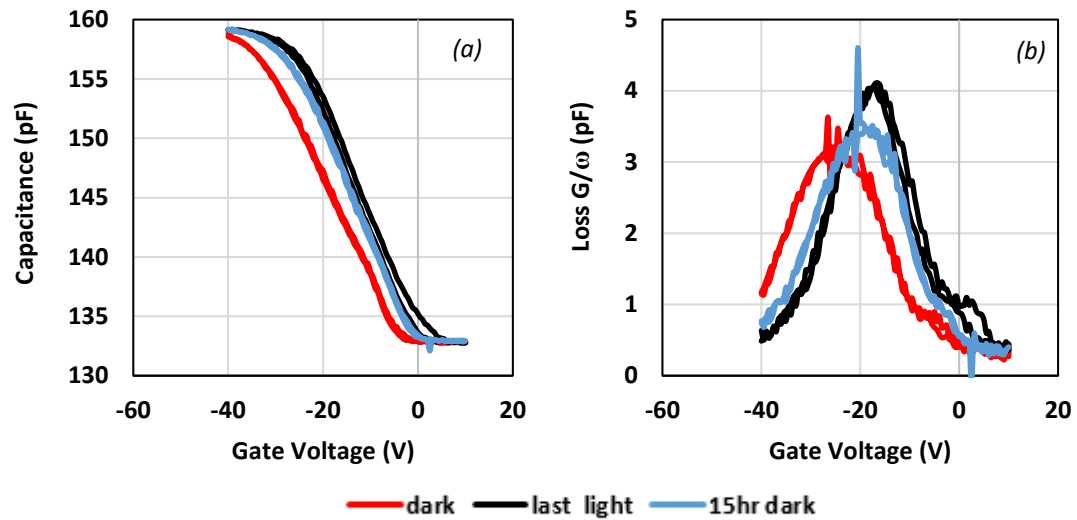


**Figure 5.15 – (a) C-V and (b) loss-V plots showing partial recovery 15 hours after ceasing the 500 nm light exposure.**

As discussed in the previous sections, light by itself is not responsible for changes in the admittance profile of DNTT-based MIS capacitors. The exposure to air is needed in order to trigger light-related processes in the semiconducting layer. These processes however, tend to follow DNTT's absorption profile, as Figure 5.12, 5.13 and 5.14 shows. For long wavelengths, light has virtually no effect on the admittance of DNTT-based MIS capacitors.

### 5.2.5 Effect of Bias Stress

The effect of bias stress in DNTT-based MIS capacitors was also investigated. For the measurements reported in this particular section, a circular (1 mm diameter) MIS capacitor was used. The PS solution was not diluted (9 wt %) and resulted in a thicker layer when compared to the previous sections. Figure 5.16 shows the initial C-V and loss-V plots before any voltage-induced stress.

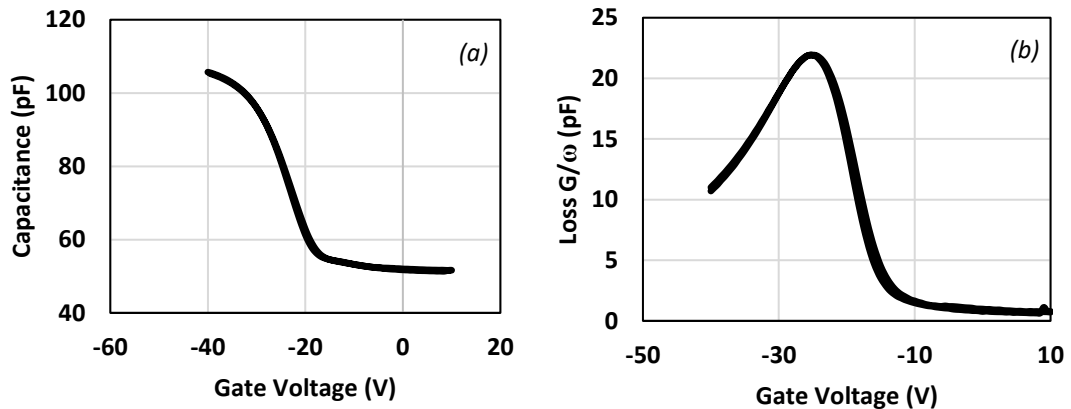


**Figure 5.16 – Voltage dependence of (a) capacitance and (b)  $G/\omega$  of DNTT-based MIS capacitors measured in the dark, in air at 1 kHz.**

As expected, the accumulation-depletion transition took place at higher negative voltages owing to the greater thickness of the PS layer. The device was then held for about 1000 minutes in the dark under ambient conditions at 300 K and a constant bias of -25 V, a voltage corresponding to midway down the C-V plot. Subsequently, capacitance and conductance readings were taken. The time evolution of the capacitance and conductance are shown in Figure 5.17.

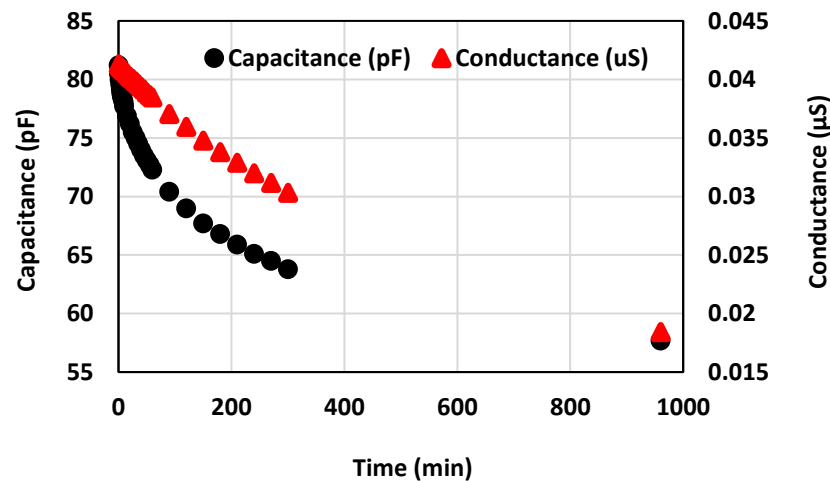


**Figure 5.17 – Time evolution of the capacitance (black dots) and conductance (red triangles) in a DNTT capacitor subject to a bias stress of -25 V.**

Both the capacitance and conductance of the device decreased, suggesting that the depletion region within the semiconductor expanded over the time investigated. This effect becomes clearer when we compare the C-V plots from before (black line) and after the bias stress (red line) in Figure 5.18. The bias stress induced a negative shift of the whole C-V plot of approximately  $-5$  V. The loss peak followed the same pattern, with its peak value maintained at  $\sim 22$  pF. This negative shift in the flatband voltage is characteristic of interface hole trapping. This, of course requires a source of holes at the interface suggesting that, when biasing the capacitor part-way down the C-V plot, band bending must be such as to encourage the drift of holes to the interface. This in turn suggests that semiconductor is acting as an intrinsic material in partial accumulation, rather than a conventional p-doped semiconductor in partial depletion.

A small anti-clockwise hysteresis also appeared in the C-V plot measured in the dark after the bias stress. This may indicate that, at full depletion, electrons are being injected into the semiconductor and thence drift to the interface. More likely, though, is that holes trapped during the bias stress are being released as the favourable band-bending is reduced during the return voltage sweep.

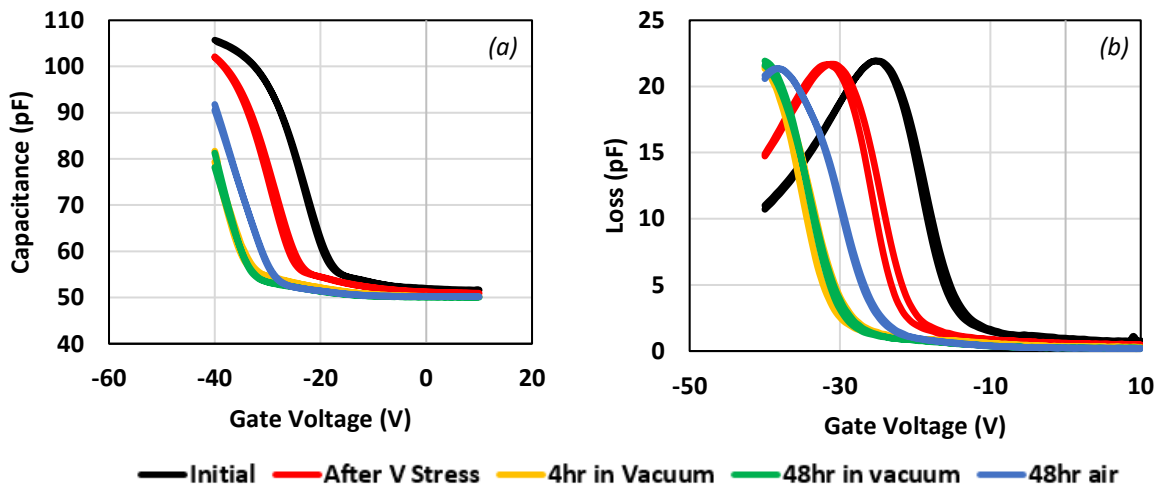


**Figure 5.18 – (a) C-V and (b) loss-V plots of DNTT-based MIS capacitors before (black) and after (red) the  $-25$  V stress. The effects of keeping the sample under vacuum for 4 hrs (yellow), 48 hrs (green) and under air exposure of 48 hrs (blue) are shown.**

In an attempt to return the device to its initial state, the sample was placed under vacuum for 4 hours. This resulted in a shift of  $\sim -10$  V in the C-V plot. Increasing the time under vacuum to 48 hours did not produce any additional effects. The negative flatband voltage shift suggests that under vacuum, either new hole trap sites were introduced or trapped electrons were removed from the PS/DNTT interface. In both cases the flatband voltage would shift to more negative values. Being prone to air-assisted effects, as discussed previously, the time under vacuum could also be removing air-related energy states from the DNTT near the top electrode, increasing the barrier height and thus shifting the flatband voltage to more negative values. Subsequently, the sample was returned to an ambient air environment at a controlled temperature of 300 K for a period of 48 hours (blue line). Now, the flatband voltage shifted to more positive values, but the device only partially recovered its initial condition. The same behaviour is reflected in the loss peaks of Figure 5.18b. The loss peak heights did not change during the bias stress test.

Assuming that DNTT is a p-doped semiconductor, for example by atmospheric oxygen, the period under vacuum would be expected to decrease the doping density  $N_A$  of the semiconductor which, according to standard Mott-Schottky theory, would increase the accumulation-depletion transition slope in the C-V plot (see Section 2.3.3), a feature not observed here. An alternative possibility is that the vacuum exposure removes oxygen/moisture induced charge centres already established in the semiconductor, effectively increasing the barrier between the injection electrode and DNTT's HOMO level. This increase in barrier height would translate as a shift in the flatband voltage, as described in section 2.3.4.3. Bias stress could also be affecting the PS insulating layer. As demonstrated by Choi *et al*, when exposed to water vapour the end chains of polystyrene can attract mobile holes and act as trap sites<sup>17</sup>.

### 5.3 DNTT-based Thin-film Transistors

In order to advance the dual-gate-like device concept presented in the introduction of this chapter, first the regular operation of DNTT transistors were investigated. The bottom-gate-top-contact devices consisted of an evaporated common aluminium gate electrode, a spin-coated film of Lisicon D207-MAK (Merck Chemicals Ltd.) as the insulating layer, evaporated DNTT and gold top source-drain electrodes. Apart from the dielectric layer, which required an UV treatment, the whole fabrication process was undertaken inside a nitrogen glovebox. In order to fabricate the whole NIR sensor device, the transistor would have to be exposed to two extra spin-coating procedures, one for the insulator layer and one for the blend. If not selected accordingly, the solvent of these two layers could damage the underlying transistor. Of the different insulators tested, Lisicon D207-MAK was the one that proved the most resilient.

On each PEN substrate a 90 transistor array was formed in 5 rows (A to E), each with a different channel length (L) ranging from 50 to 200  $\mu\text{m}$ , and with different W/L ratios as in Table 5.1.

Name Tag	Width W (mm)	Channel Length L ( $\mu\text{m}$ )	W/L ratio
A #1	2	50	40
A #2	1		20
B #1	2	75	26.6
B #2	1.5		20
C #1	2	100	20
C #2	2		20
D #1	2	150	13.3
D #2	3		20
E #1	2	200	10
E #2	4		20

**Table 5.1 – Channel length and width for the 5 different rows on the PEN substrate.  
Each group contained nine transistors.**

Following the effects reported with the MIS capacitors, DNTT transistors were also prone to air-related processes. The effects of exposure to air had already been investigated for PS/DNTT devices, and showed that after a crucial period of 2 days of air exposure the transistor's performance was at its best<sup>11,18,19</sup>. To investigate these effects, DNTT transistors fabricated with Lisicon D207-MAK as the insulating layer were measured immediately after fabrication and then after 2.5 days of exposure to air. During the air exposure period, the devices were kept in the dark to avoid any light induced effects and all measurements were taken at room temperature, in ambient air conditions and in the dark. The electrical measurements were conducted in a probe station (Sel-tek Ltd – Signatone 1160 Series) mounted within an aluminium box to minimize the effects of electromagnetic interference when measuring low currents. The three probes (source, drain and gate) were controlled using micromanipulators in order to avoid using silver paint-based connections. Transfer ( $I_D$  vs  $V_G$ ) and output ( $I_D$  vs  $V_D$ ) curves of the transistors were performed using a Keithley 2600 SMU (Tektronix).

### 5.3.1 Characteristics immediately after fabrication

Immediately after the fabrication, the devices in groups A #1, A #2, B #1, B #2 and C #1 were analysed. The devices from these 5 groups displayed the same behaviour, and to illustrate it only the devices in group A #1 are shown here. The linear (black line) and saturation (red line) transfer plot and output characteristic curves of the transistors in row A #1 are shown in Figure 5.19. The linear (saturation) transfer curves were obtained by biasing the drain electrode at -1 V (-60 V) while the drain current was measured as a function of gate bias. The output plots were measured by holding the gate bias at values from 10 V to -60 V while the drain current was measured as a function of drain voltage. Each pair of black and red curves in the transfer plot represents one transistor in that row.

The OFF current of all devices was in the  $10^{-10}$  A range, giving an ON/OFF ratio of approximately  $10^3$  for the linear and  $10^5$  for the saturation regime and turn-on voltages near 0 V. Despite having the same structure and geometric parameters, the devices in group A #1 displayed a spread in the output curves, as shown in Figure 5.19b. A weak feature at around -10 V in the output curves also appeared here, as in the MIS capacitor results. Since the MIS capacitors were made with PS as the insulating layer and the transistors with Lisicon D207-MAK, the presence of such a feature in the transistor results indicates that its origin is most likely from DNTT itself and not the underlying insulator. Of the 9 devices tested in this group, the characterization curves of 3 were very noisy and are not displayed here.

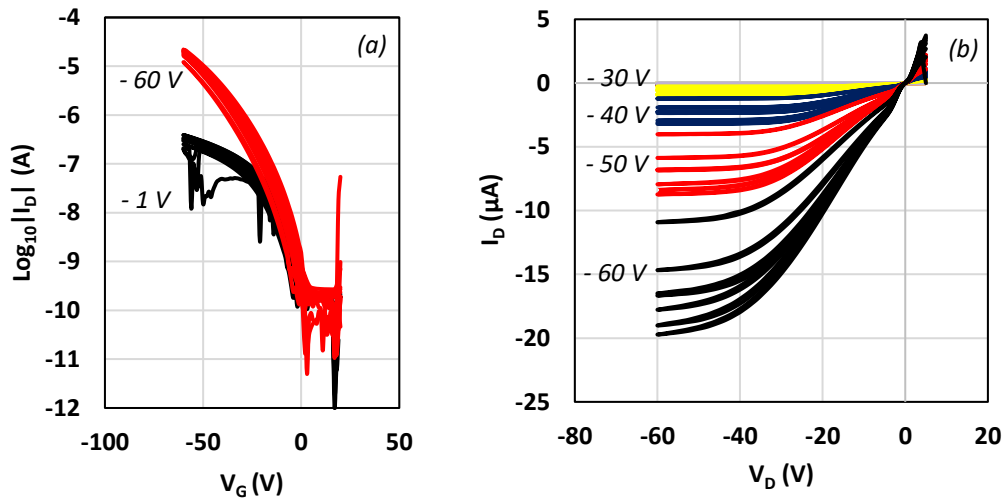


**Figure 5.19 – (a) Transfer and (b) output curves of Lisicon/DNTT transistors with a W/L ratio of 40 and channel length of  $50 \mu\text{m}$  immediately after fabrication.**

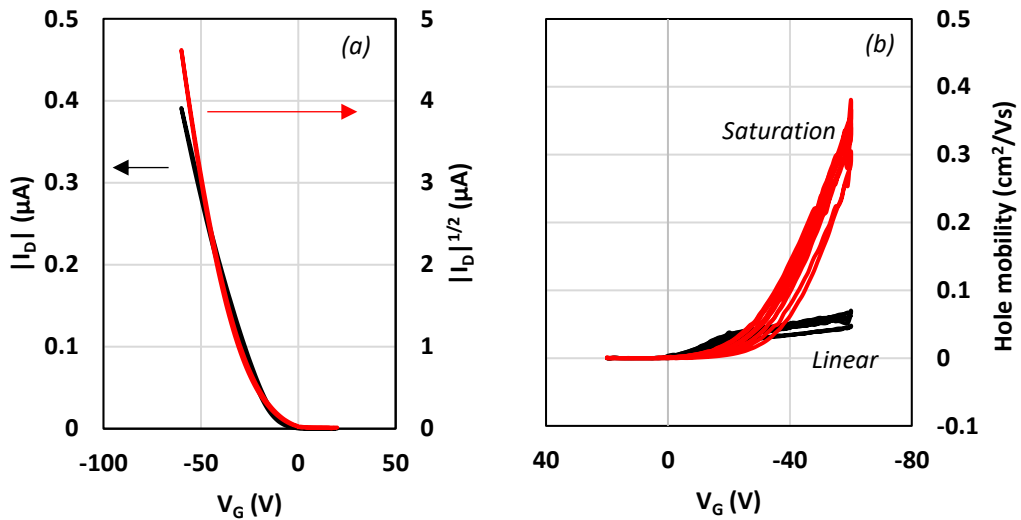


**Figure 5.20 – (a) Linear transfer curves of one device in group A #1 in the linear (black) and saturation (red) regimes. (b) Hole mobility of transistors in group A #1 calculated as a function of  $V_G$  in the linear (black) and saturation (red) regimes.**

The linear sections of the transfer plots in the linear (black line) and saturation (red line) regime for one device in group A #1 are shown in Figure 5.20a. From the extrapolation to the voltage axis, the threshold voltage ( $V_{\text{TH}}$ ) for the linear and

saturation regimes were estimated to be  $\sim -7$  V and  $\sim -15$  V, respectively. Due to the curvature of the plots, the hole mobility (shown in Figure 5.20b) was estimated from the local slope of the transfer plot following the standard equations:

$$\mu_{lin} = \frac{L}{WC_I V_D} \frac{dI_D}{dV_G} \quad (5.1)$$

$$\mu_{sat} = \frac{2L}{WC_I} \left( \frac{d\sqrt{I_D}}{dV_G} \right)^2 \quad (5.2)$$

where  $C_I$  is the insulator capacitance, measured using a circular capacitor present in the mask arrangement.

A small spread of the samples in group A #1 were also evident in the mobility plots. The hole mobility measured in the linear regime saturated at  $\sim 5 \times 10^{-2}$  cm<sup>2</sup>/Vs, while in the saturation regime the mobility was very dependent on  $V_G$ , reaching a maximum value of  $\sim 0.3$  cm<sup>2</sup>/Vs at  $-60$  V.

### 5.3.2 Characteristics after 2.5 days

After 2.5 days of air exposure in the dark, the electrical characteristics of all transistors were measured. Of all 90 devices fabricated in this array, only 3 did not work, evidencing the reliability of the Lisicon D207-MAK/DNTT pair. The high yield (> 95%) of working transistors is remarkable, especially for a solution processed insulating layer. Such high yields were also found in the literature when using a flash evaporated insulator with a roll-to-roll process in combination with DNTT<sup>19</sup>.

Figure 5.21 shows the transfer and output characteristics of 9 transistors in group A #1 after 2.5 days of air exposure in the dark. The previous data spread gave way to almost identical curves for this device geometry. The OFF current continued in the  $10^{-10}$  A range, but the ON current increase 10-fold, giving an ON/OFF ratio of approximately  $10^4$  for the linear regime and  $10^6$  for the saturation regime. As discussed in the MIS capacitor results, exposure to air affects the performance of DNTT devices. In this case, the introduction of new energy levels near the top contact, through

exposure to air, facilitated the injection of charges into DNTT, evidenced by the positive shift of turn-on voltages in both linear and saturation curves. Such positive shifts also happen when DNTT devices are exposed to light, as described in the previous sections and in other works<sup>1,11</sup>.

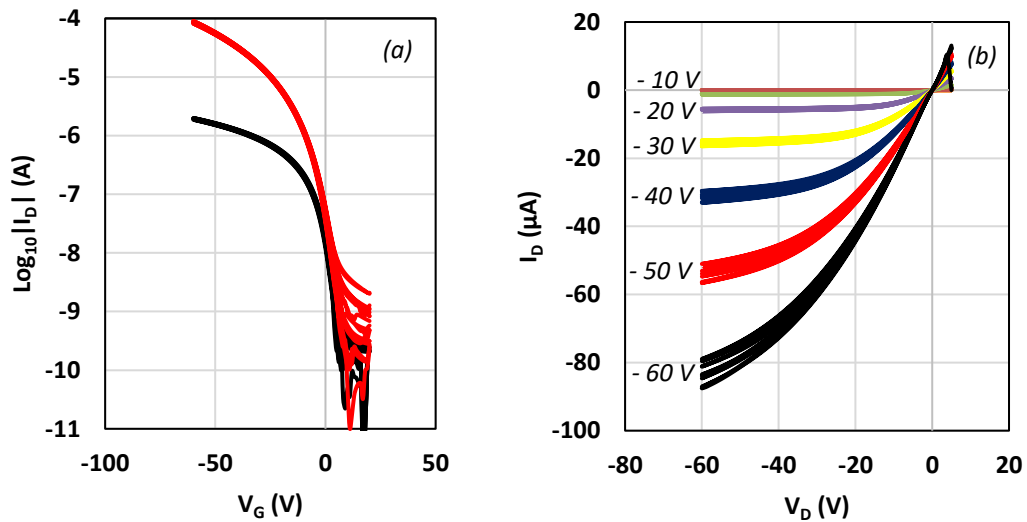


**Figure 5.21 – (a) Transfer and (b) output curves of Lisicon/DNTT transistors with a W/L ratio of 40 and channel length of 50  $\mu\text{m}$  after 2 and half days of air exposure.**

The data spread was significantly reduced in the output curves (Figure 5.21b) and the smaller negative voltage curves are now visible. When compared to devices measured immediately after fabrication, the ones exposed to air displayed an output current almost 5 times higher. The increase in current after air exposure, both in the output and in the transfer plots, can be related either to an actual increase in hole mobility by introduction of dopants or by an increase in the effective mobility through reduction of contact resistance<sup>19</sup>, with the latter being the most likely explanation. The weak feature at around -10 V is not so evident after 2.5 days of air exposure.

The linear sections of the transfer plots of all 9 devices in group A #1, after the air exposure period, are shown in Figure 5.22a. The  $V_{TH}$  values obtained from the extrapolation to the voltage axis are  $\sim -2$  V for the linear and  $\sim 0$  V for the saturation regime. Comparing to the plot obtained immediately after fabrication, a positive shift of the whole curve can be seen.

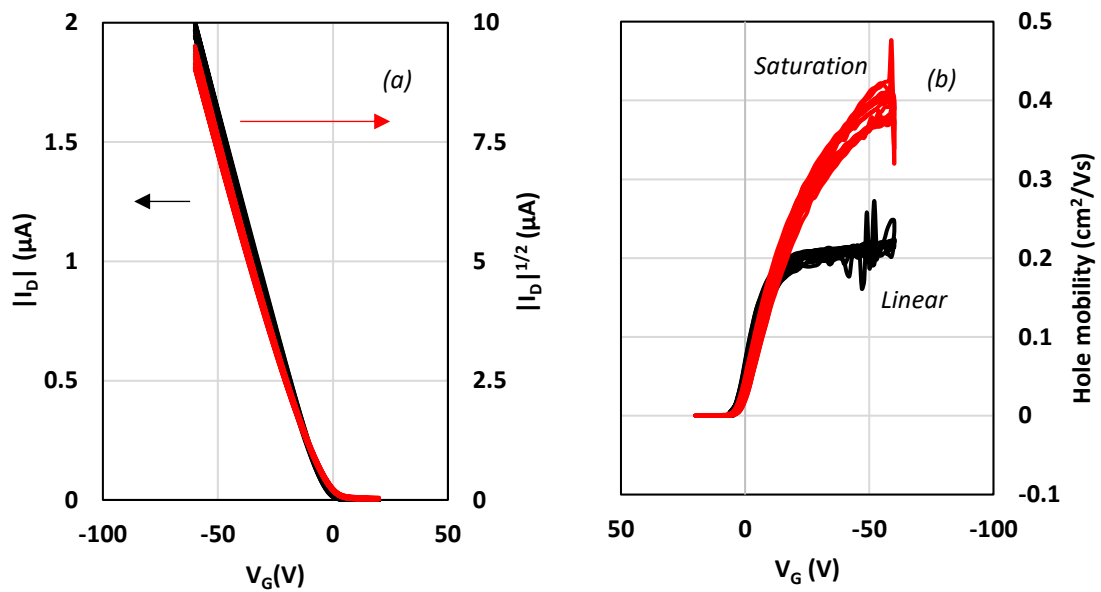


**Figure 5.22 - (a) Linear transfer curves of all devices in group A #1 in the linear (black) and saturation (red) regimes. (b) Hole mobility of transistors in group A #1 calculated as a function of  $V_G$  in the linear (black) and saturation (red) regimes after 2 and half days of air exposure in the dark.**

The hole mobility of all 9 transistors in group A #1 were calculated using equations (5.1) and (5.2) and are shown in Figure 5.22b. After the air exposure, both linear and saturation maximum hole mobilities increased. The linear mobility saturated at  $\sim 0.2 \text{ cm}^2/\text{Vs}$  and the mobility calculated from the saturation regime reached a maximum value of  $\sim 0.4 \text{ cm}^2/\text{Vs}$ . The data spread is also not observed, with all 9 transistors behaving very similarly to one another. The relation between hole mobility and device geometry are shown in Figure 5.23. Each point in Figure 5.23 represents a mean value obtained from the 9 transistors analysed in each device geometry.

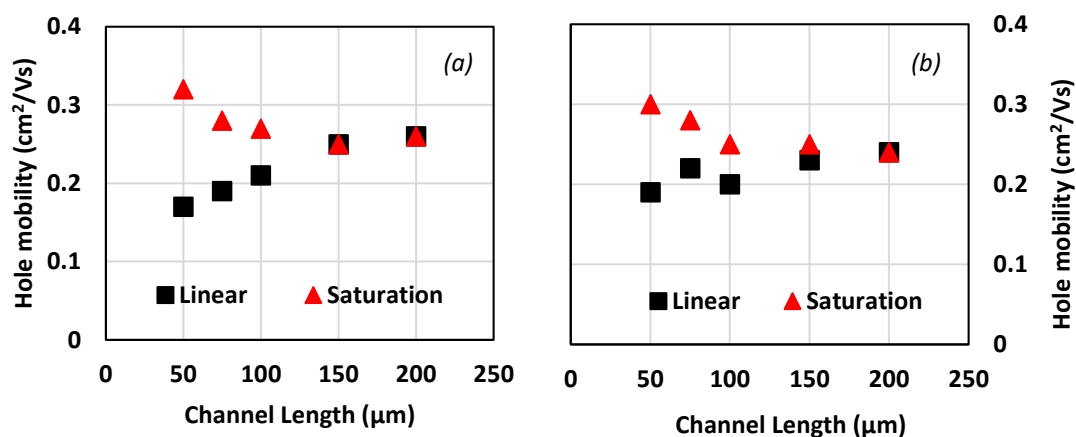


**Figure 5.23 – Mean hole mobility as a function of channel length for devices with (a) same width (2 μm) and (b) same W/L ratio (20).**

When compared to other DNTT-based transistors in the literature<sup>20-22</sup> the hole mobilities of the present devices were poorer. Such low values could be explained by the morphology of the semiconducting layer (Figure 5.24) when deposited on top of the insulator Lisicon D207-MAK. These rod-like features are exclusive to the combination Lisicon D207-MAK/DNTT and are not found in other DNTT-based devices.

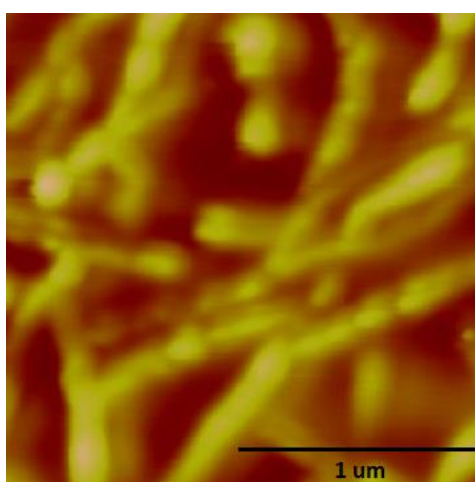


**Figure 5.24 – AFM image of DNTT on top of Lisicon D207-MAK.**

## CONCLUSION

In conclusion, the behaviour of devices based on the small molecule DNTT, an air-stable compound commonly investigated in transistors technology, under different conditions was analysed. In the first section, the admittance of MIS capacitors were analysed. The behaviour is similar to a p-type semiconductor capacitor, with accumulation of holes occurring at negative voltages and a decrease in capacitance, usually associated with a formation of a conventional depletion region, at positive voltages. While exposed to light, the capacitors behave differently when under vacuum and open to air. The results point to the fact that the combination light plus air is responsible for C-V hysteresis and shifts in the flatband voltage. When illuminated under vacuum or when kept in the dark under ambient air conditions, the devices did not display any hysteresis effect or shifts in the flatband. Also, Figure 5.6 indicates that these effects only come into play when significant electric fields are present near the gold electrode, suggesting that DNTT-based devices are prone to photo-assisted charge injection in the presence of air. The effect of measurement frequency, temperature, exposure to different light wavelengths were also investigated and indicated the presence of interface states at the PS/DNTT interface.

The effect of bias stress on DNTT MIS capacitors was also investigated. After being biased part way down the accumulation-depletion transition for over 1000 min, the admittance plots shifted to more negative values, indicating the presence of interface hole traps. For this to happen, a source of holes at the interface would be required, suggesting that the semiconductor is acting as an intrinsic material in partial accumulation. This affirmation could change the way DNTT devices are analysed and require more investigation.

In the last section, the behaviour of DNTT transistors fabricated on top of Lisicon D207-MAK insulator was analysed. Such a combination would be used in the `dual-gate` light sensor, as described in the introduction of the chapter. The pair Lisicon D207-MAK/DNTT proved to be extremely reliable as the yield of working transistors

---

was higher than 95% for the 90 transistors tested. Transistor performance improved significantly after 2.5 days of air exposure, evidencing the air-related processes discussed in the previous section. Such improvement was attributed to a decrease in barrier height facilitating the injection of charges from the top electrode into DNTT. The hole mobility obtained from these devices was smaller than expected when compared to other DNTT devices in the literature. From the AFM image, it could be seen that when deposited on top of Lisicon D207-MAK, the DNTT film was composed of rod-like structures, which possibly hindered the charge transport along the semiconductor/insulator interface.

## REFERENCES

- 1 J. Milvich, T. Zaki, M. Aghamohammadi, R. Rödel, U. Kraft, H. Klauk, and J. N. Burghartz, *Organic Electronics* **20**, 63 (2015).
- 2 F. Maddalena, M. Spijkman, J. J. Brondijk, P. Fonteijn, F. Brouwer, J. C. Hummelen, D. M. de Leeuw, P. W. M. Blom, and B. de Boer, *Organic Electronics* **9**, 839 (2008).
- 3 X. Tong and S. R. Forrest, *Organic Electronics* **12**, 1822 (2011).
- 4 T. Hayashi, N. Take, H. Nakano, A. Fujiwara, T. Sekitani, and T. Someya, *Display Technology, Journal of* **11**, 604 (2015).
- 5 T. Hayashi, N. Take, H. Tamura, T. Sekitani, and T. Someya, *Journal of Applied Physics* **115**, 093702 (2014).
- 6 D. M. Taylor and N. Alves, *Journal of Applied Physics* **103** (2008).
- 7 S. M. Sze, *Physics of Semiconductor Devices* (John Wiley & Sons, 1981).
- 8 M. Devynck, B. Rostirolla, C. P. Watson, and D. M. Taylor, *Applied Physics Letters* **105**, 183301 (2014).
- 9 C. P. Watson, M. Devynck, and D. M. Taylor, *Organic Electronics* **14**, 1728 (2013).
- 10 C. P. Watson, PhD Thesis, Bangor University (2011).
- 11 Z. Ding, G. Abbas, H. E. Assender, J. J. Morrison, S. G. Yeates, E. R. Patchett, and D. M. Taylor, *ACS Applied Materials & Interfaces* **6**, 15224 (2014).
- 12 C. P. Watson and D. M. Taylor, *Applied Physics Letters* **99** (2011).
- 13 N. Alves and D. M. Taylor, *Applied Physics Letters* **92** (2008).
- 14 W. Xie, K. Willa, Y. Wu, R. Häusermann, K. Takimiya, B. Batlogg, and C. D. Frisbie, *Advanced Materials* **25**, 3478 (2013).
- 15 N. K. Za'aba, J. J. Morrison, and D. M. Taylor, *Organic Electronics* **45**, 174 (2017).
- 16 E. M. Lopes, R. S. Ywata, N. Alves, F. M. Shimizu, D. M. Taylor, C. P. Watson, A. J. F. Carvalho, and J. A. Giacometti, *Organic Electronics* **13**, 2109 (2012).
- 17 H. H. Choi, W. H. Lee, and K. Cho, *Advanced Functional Materials* **22**, 4833 (2012).
- 18 G. A. Abbas, Z. Ding, H. E. Assender, J. J. Morrison, S. G. Yeates, E. R. Patchett, and D. M. Taylor, *Organic Electronics* **15**, 1998 (2014).
- 19 E. R. Patchett, A. Williams, Z. Ding, G. Abbas, H. E. Assender, J. J. Morrison, S. G. Yeates, and D. M. Taylor, *Organic Electronics* **15**, 1493 (2014).
- 20 T. Yamamoto and K. Takimiya, *Journal of the American Chemical Society* **129**, 2224 (2007).
- 21 S. Haas, Y. Takahashi, K. Takimiya, and T. Hasegawa, *Applied Physics Letters* **95**, 022111 (2009).
- 22 U. Zschieschang, R. Hofmockel, R. Rödel, U. Kraft, M. J. Kang, K. Takimiya, T. Zaki, F. Letzkus, J. Butschke, H. Richter, J. N. Burghartz, and H. Klauk, *Organic Electronics* **14**, 1516 (2013).

# CHAPTER 6

## DEVELOPING THE PHOTOCAPACITANCE MODEL

### 6.1 Introduction

This chapter discusses the results obtained from an improved mathematical model of photocapacitance in organic MIS capacitor in which electron trapping at the semiconductor/insulator interface is modelled. Firstly, the original model is presented and its validity is discussed. Then, as a solution to better represent a more general behaviour, the idea of electron capture, emission and recombination rates are introduced to the model.

### 6.2 Photocapacitance Modelling

In this section, a model that describes the main features observed in an admittance measurement of organic-based MIS capacitors is tested. This first approach uses the

work of Watson *et al*<sup>1,2</sup> as a starting point and advances from there. This model was already mentioned in Section 2.3.5, but a more detailed description is needed here.

The model uses an ideal MIS capacitor structure, as showed in Figure 6.1, where the active layer was treated as a uniform medium. When driven into depletion and illuminated, photons with high enough energy can be absorbed by the blend, creating excitons that are dissociated with the help of the electric field of the depletion region. While a more realistic view would include the dissociation of charges at the P3HT/PCBM interface, with the free electrons and holes being transported through the different materials, this first approach was enough to simulate the important features observed in a  $C$ - $V$  measurement using only P3HT as the active layer. The photo-created free holes are driven to the bulk of the semiconductor, while the free electrons drift to the semiconductor/insulator interface.

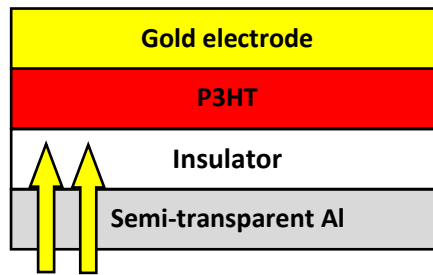


**Figure 6.1 – P3HT MIS capacitor device structure with illumination through the gate electrode.**

As described in Chapter 2, the measured capacitance per unit area  $C_M(t)$  can be calculated as the series sum of the insulator capacitance  $C_I$  and the depletion region capacitance  $C_D(t)$ , both per unit area:

$$\frac{1}{C_M(t)} = \frac{1}{C_I} + \frac{1}{C_D(t)} \quad (6.1)$$

The insulator capacitance is determined by the geometric characteristics of the device and, if all lateral conduction effects are neglected, is equal to the measured capacitance during the accumulation regime, where majority carriers in the

semiconductor are driven to the semiconductor/insulator interface. The depletion capacitance per unit area, however, is a function of depletion region width  $d_p(t)$ :

$$C_D(t) = \frac{\varepsilon_s}{d_p(t)} \quad (6.2)$$

where  $\varepsilon_s$  is the absolute permittivity of the semiconductor. The classical depletion region thickness  $d_p(t)$  is calculated as a function of the applied gate voltage  $V(t)$  and the flatband voltage  $V_{FB}(t)$  through the relation<sup>3</sup>:

$$d_p(t) = \sqrt{\frac{\varepsilon_s^2}{C_I^2} + \frac{2\varepsilon_s}{qN_A} (V(t) - V_{FB}(t))} - \frac{\varepsilon_s}{C_I} \quad (6.3)$$

where  $N_A$  is the doping density of the semiconductor, assumed to be constant throughout the semiconductor. In this approach, the concentration of thermally generated charges was assumed to be negligible due to the large band gap of organic semiconductors, so little to no interface trapping occurred in the dark  $C$ - $V$  measurement. In this model, Watson *et al* assumed that all free electrons, generated through light absorption, would drift to the interface and become trapped, shifting the flatband voltage by:

$$V_{FB}(t) = \frac{q}{C_I} n_t(t) \quad (6.4)$$

where  $n_t(t)$  is the density of trapped electrons at the semiconductor/insulator interface. With this in mind, the authors needed to describe the rate of electron generation in order to calculate the time-dependence of  $V_{FB}(t)$ , which then led to form of  $d_p(t)$  and then  $C_M(t)$ .

Light entering the device through the semi-transparent electrode is absorbed by the semiconducting material following its absorption profile, so that the intensity of light at a depth  $x$  from the semiconductor/insulator interface in the semiconductor is given by Lambert's law:

$$I(x) = I_0 e^{-\alpha(\lambda)x} \quad (6.5)$$

where  $\alpha(\lambda)$  is the absorption coefficient of the material for light of wavelength  $\lambda$ .

Since light is being absorbed by the active layer, the change in the photon flux density  $\Phi(x)$  can be interpreted as a quantity proportional to the rate of exciton generation  $N_{ex}(x)$ , depending only on the efficiency of exciton generation  $\eta$ :

$$\frac{dN_{ex}(x)}{dt} = -\eta \frac{d\Phi(x)}{dx} = \eta \frac{\lambda}{hc} \alpha(\lambda) I_0 e^{-\alpha(\lambda)x} \quad (6.6)$$

However, not all excitons dissociate into free charge carriers. Due to their extremely low lifetime, excitons can quickly recombine and photo-created charges would be lost. However, recombination rates are significantly reduced, i.e. exciton dissociation enhanced, in the presence of an electric field. Accordingly, the authors included an Onsager term to represent the probability of exciton dissociation  $\xi(F)$  (equation 6.7) in the electric field  $F(x)$  appearing within the depletion region:

$$\xi(F) = \xi(0)(1 + \beta F(x)) \quad (6.7)$$

with

$$\beta = \left( \frac{e^3}{8\pi\epsilon_s k^2 T^2} \right) \quad (6.8)$$

where  $\xi(0)$  is the probability of exciton dissociation when the electric field is zero,  $k$  is Boltzmann's constant and  $T$  the absolute temperature. The magnitude of the electric field within the semiconductor is obtained by solving Poisson's equation within the depletion region,

$$\nabla^2 \varphi = -\frac{\rho}{\epsilon_s} \quad (6.9)$$

where  $\varphi$  is the potential and assuming that (a) the charge density  $\rho$  is equal to the uniform doping density  $N_A$  in the semiconductor, i.e. no free carriers are present; and (b) that the electric field is zero in the bulk of the semiconductor ( $x \geq d_p(t)$ ) and maximum at the semiconductor/insulator interface ( $x = 0$ ):

$$F(x) = \frac{qN_A}{\varepsilon_s} (d_p(t) - x). \quad (6.10)$$

The rate of free electron generation is then obtained by multiplying the rate of exciton generation (Eq. 6.6) with the exciton dissociation probability (Eq. 6.7), while integrating over the whole depletion region. Once all free electrons are assumed to become trapped, the rate of electron trapping  $dn_t(t)/dt$  is calculated through:

$$\frac{dn_t(t)}{dt} = \eta \frac{\lambda I_0}{hc} \xi(0) \alpha(\lambda) \int_0^{d_p(t)} e^{-\alpha(\lambda)x} (1 + \beta F(x)) dx \quad (6.11)$$

Integration of Eq. 6.11 leads to:

$$\frac{dn_t(t)}{dt} = K \frac{qN_A}{\varepsilon_s} \left[ d_p(t) - \frac{1}{\alpha(\lambda)} (1 - e^{-\alpha(\lambda)d_p(t)}) \right] \quad (6.12)$$

where

$$K = \eta \xi(0) \beta \frac{\lambda I_0}{hc} \quad (6.13)$$

is a constant for a given light wavelength and temperature.

These equations were input into a MATLAB<sup>®</sup> program together with the experimental parameter values of  $C_I$ ,  $\lambda$ ,  $A$ ,  $N_A$ ,  $\alpha(\lambda)$  and  $\varepsilon_s$  and  $C$ - $V$  curves were simulated. The program was constructed in a way that the device started in accumulation and the applied gate voltage drove the semiconductor into depletion, where photo-created charges start influencing the capacitance. Figure 6.2 shows the simulated  $C$ - $V$  curves obtained with this model using different light wavelengths. In order to match the observed capacitance plateau level in depletion, when exposed to light, the authors had to adjust the value of  $K$  accordingly.

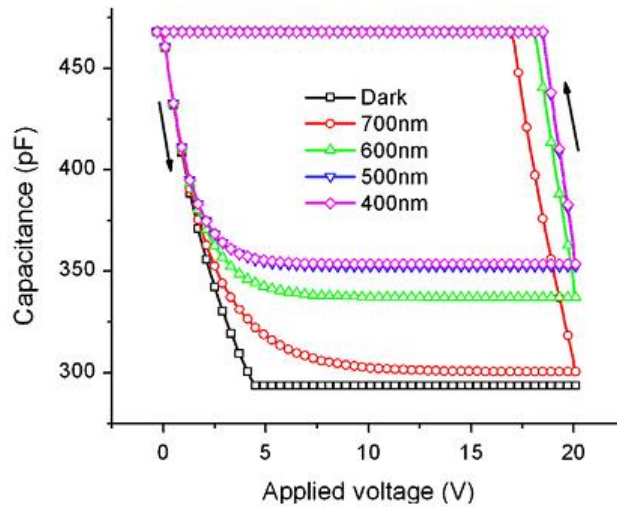


**Figure 6.2 – Simulated  $C$ - $V$  plots using the initial model for different light wavelengths. Adapted with permission from <sup>1</sup>.**

The simulated  $C$ - $V$  curves obtained with this model correctly describe the behaviour of MIS capacitors when exposed to light during the forward sweep, i.e., the minimum capacitance level in depletion follows the semiconductor's absorption spectrum. On the reverse sweep, however, the simulated value of  $C_M$  returns to the accumulation value within a few decrements of  $V_G$ . Such behaviour is a consequence of the assumption that all photoelectrons escaping recombination become trapped once they reach the interface, and remain so. This is not always true, such behaviour is only seen in real devices where extensive electron trapping occurs at the semiconductor/insulator interface.

To better represent a more general behaviour, see for example Figure 4.6 and Figure 5.14, where electrons interact with shallow interface traps, the model need to be reworked. To achieve this, consideration has to be given to electron capture and emission rate by interface traps as well as to the recombination of free electrons which escape trapping. Such processes can be described using Shockley-Read-Hall statistics, which determine the interactions between free charges and trap sites<sup>3</sup>. This effectively separates the photogenerated electrons that escape exciton recombination into trapped or free electrons, both of which influence the  $C$ - $V$  curve. Trapped electrons in the interface shift the flatband voltage of the device, modifying the depletion region

thickness. However, due to the sweep of the electric field and interaction with other particles energy is transferred to the trapped electrons and may release them, justifying the introduction of the emission rate term.

Free electrons also prevent the expansion of  $d_p(t)$  as voltage increases, since any change in negative charge induced in the semiconductor by the gate voltage, occurs in the population of free electrons, as in an inversion layer, rather than by exposure of more ionised acceptors. On the other hand, free electrons can be captured by trap sites or recombine. In the latter case electrons are effectively ‘lost’ from the device especially during the reverse voltage sweep, hence the introduction of the capture rate and recombination term.

Taking these effects into account, the rate of change of free electrons at the interface can then be described by

$$\frac{dn_f}{dt} = \frac{dn}{dt} - \frac{dn_c}{dt} + \frac{dn_e}{dt} - \frac{dn_r}{dt} \quad (6.14)$$

where  $\frac{dn_f}{dt}$  represents rate of change of free electrons,  $\frac{dn}{dt}$  the generation term described in the initial model (equation 6.12),  $\frac{dn_c}{dt}$  the rate of electron capture by traps,  $\frac{dn_e}{dt}$  the rate of electron emission from traps and  $\frac{dn_r}{dt}$  the rate of recombination for free electrons.

Based on the depth of the trap, electrons can move in and out of traps as a result of band bending – effectively the Fermi level sweeps through interface states in response to changes in  $V_G$ . The occupancy of the trap sites, which influences the shifts in flatband, can now be described by the capture and emission rate of electrons, which depends on the trap energy ( $E_t$ ) relative to the conduction band ( $E_c$ ), i.e.  $(E_c - E_t)$ , the thermal velocity of the charge carriers ( $V_{th}$ ) and the capture cross-section of the trap ( $\sigma$ ). The electron capture ( $\frac{dn_c}{dt}$ ) and emission ( $\frac{dn_e}{dt}$ ) rate can be expressed as:

$$\frac{dn_c}{dt} = \frac{\sigma N_c (N_t - n_t) V_{th}}{1 + e^{[(E_c - E_{fn}) - \phi]/kT}} \quad (6.14)$$

$$\frac{dn_e}{dt} = V_{th} \sigma N_c n_t e^{-(E_c - E_t)/kT} \quad (6.15)$$

where  $E_{fn}$  is the electron quasi Fermi level determined by illumination intensity,  $n_t$  is the density of trapped charges,  $N_t$  is the maximum density of trap sites,  $N_c$  is the effective density of states in the conduction band and  $\phi$  is the band bending at the interface for a particular depletion region width, given by

$$\phi = \frac{qN_A d_p(t)^2}{2\varepsilon_s}. \quad (6.16)$$

If all traps are filled, then the term  $(N_t - n_t)$  goes to zero and electron capture by traps ceases to exist.

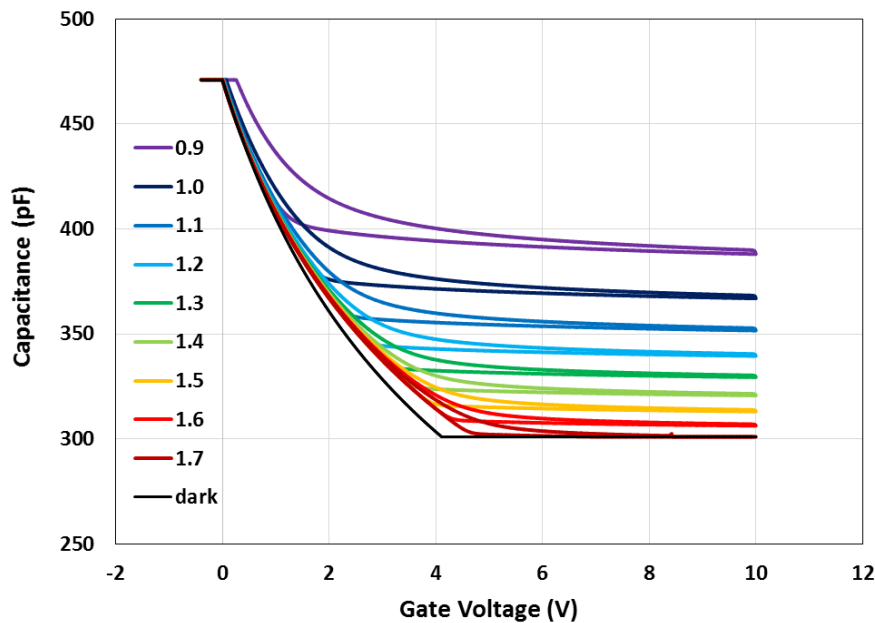
During the simulations, the material and device parameters were kept constant and are given in Table 6.1 below.

Parameter	Value
<i>Semiconductor thickness</i>	100 nm
<i>Device area</i>	$3.14 \times 10^{-6} \text{ m}^2$
<i>Semiconductor relative dielectric constant</i>	3
<i>Semiconductor doping density, <math>N_A</math></i>	$3 \times 10^{22} \text{ m}^{-3}$
<i>Absorption coefficient <math>\alpha</math>(@500nm)</i>	$7.7 \times 10^6 \text{ m}^{-1}$
<i>Insulator capacitance per unit area, <math>C_i</math></i>	$1.50 \times 10^{-4} \text{ F/m}^2$
<i>Temperature</i>	300 K
<i>Capture cross section, <math>\sigma</math></i>	$1 \times 10^{-20} \text{ m}^2$
<i>Thermal velocity, <math>V_{th}</math></i>	$1 \times 10^5 \text{ m/s}$
<i>Effective density of states at <math>E_c</math>, <math>N_c</math></i>	$1 \times 10^{25} \text{ m}^{-3}$

**Table 6.1 – Device parameters and constants used during the simulations.**

Using the values in Table 6.1,  $C$ - $V$  curves were simulated using the software MATLAB<sup>®</sup> with the introduction of the free-electron/trap related parameters (see Appendix A for the detailed MATLAB<sup>®</sup> code). The effect of systematic changes in various parameters are discussed in the following paragraphs. All dark curves shown in the following figures were obtained with the K parameter set as zero.

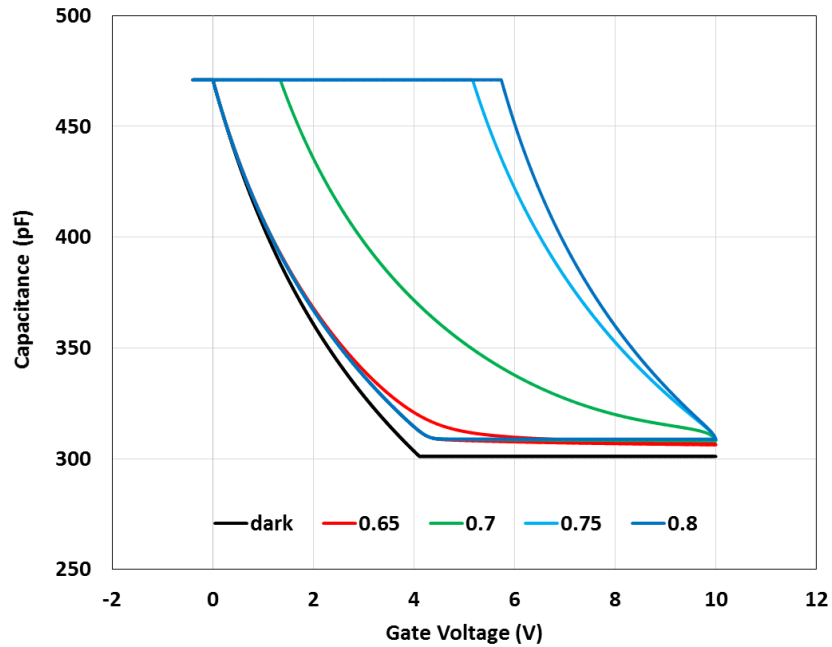
Simulated  $C$ - $V$  curves for different values of  $(E_c - E_{fn})$  are shown in Figure 6.3. As  $E_{fn}$  approaches  $E_c$ , corresponding to higher light intensity, the minimum capacitance reached during the depletion regime increases. However, the increase was not linearly dependent on the value of  $(E_c - E_{fn})$ . As the energetic difference decreased, the changes in the minimum capacitance increased. As explained in Chapter 2, both trapped charges as well as free electrons at the semiconductor/insulator interface can cause an increase in the minimum capacitance during the depletion regime, both of which are now contributing to the simulated plots.



**Figure 6.3 – Effect of  $(E_c - E_{fn})$  value on the simulated  $C$ - $V$  curves using the new model. Values used for calculation were  $K = 1 \times 10^{10}$ ,  $N_t = 1 \times 10^{18} \text{ m}^{-3}$ ,  $(E_c - E_t) = 0.65 \text{ eV}$ .**

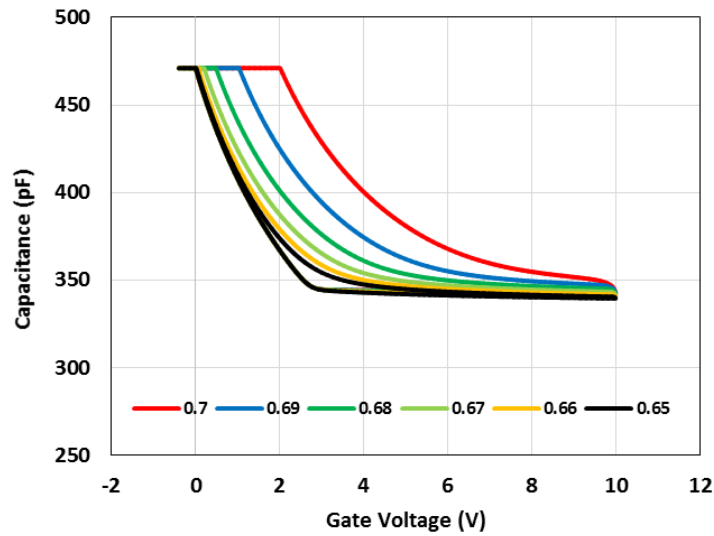
The effect of the trap depth  $(E_c - E_t)$  was also investigated with simulations shown in Figure 6.4. For the values used in the simulation, for trap depths  $\leq 0.6 \text{ eV}$ , the reverse  $C$ - $V$  curve essentially retraced that obtained during the forward sweep – electrons rapidly detrap from shallower traps. However, as the trap depth increased above  $0.6 \text{ eV}$ , the shifts in flatband voltage observed during the reverse sweep became more and more prominent, as the blue curve in Figure 6.4 shows. When  $(E_c - E_t)$  is  $0.9$

eV, the resulting  $C$ - $V$  curve resembles that produced by the original model (Figure 6.2), where extensive trapping resulted in a large shift of flatband voltage.



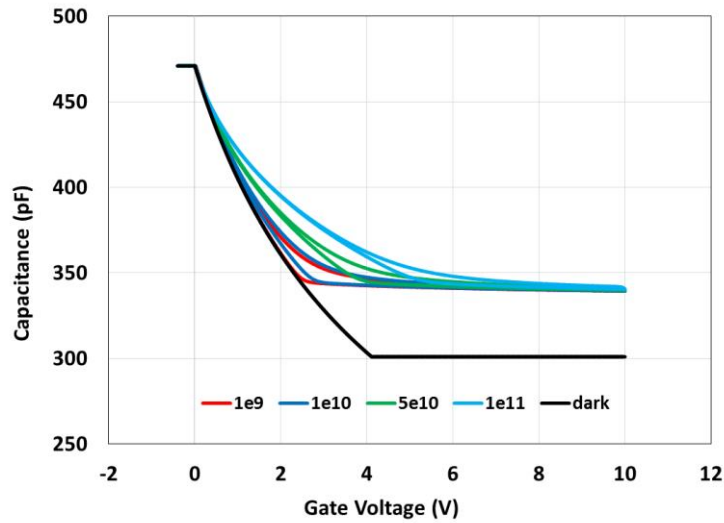
**Figure 6.4 – Effect of  $(E_c - E_t)$  on the simulated  $C$ - $V$  curves using the new model. Values used for calculation were  $K = 1 \times 10^{10}$ ,  $N_t = 1 \times 10^{18} \text{ m}^{-3}$ ,  $(E_c - E_{fn}) = 1.5 \text{ eV}$ .**

For the values used in the simulation, even a difference as small as 0.05 eV produced a large shift in  $V_{FB}$  during the reverse sweep, indicative of much deeper trapping. Figure 6.5 shows how fine tuning of  $(E_c - E_t)$  influences the shift in the flatband voltage.



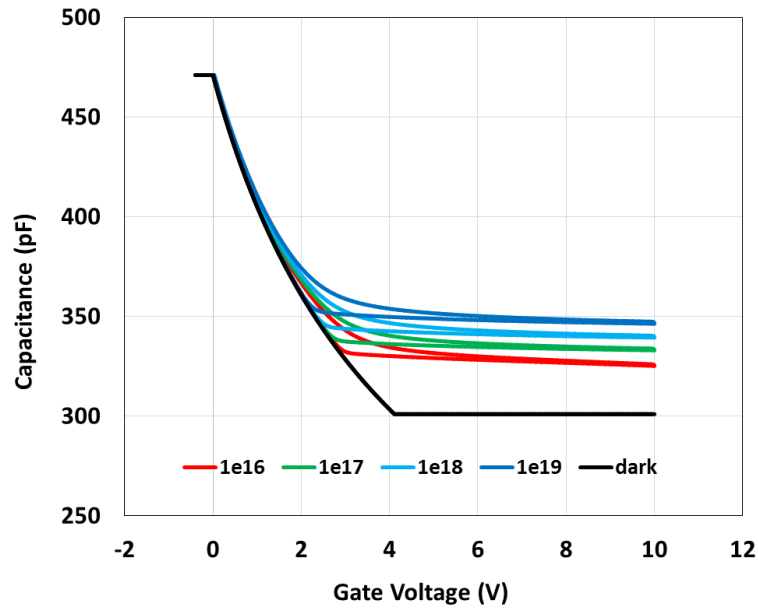
**Figure 6.5 – Effect of fine tuning ( $E_c-E_t$ ) on the simulated  $C-V$  curves using the new model. Values used for calculation were  $K = 1 \times 10^{10}$ ,  $N_t = 1 \times 10^{18} \text{ m}^{-3}$ ,  $(E_c-E_{fn}) = 1.2 \text{ eV}$ .**

Changes in the  $K$  parameter are related to changes in the zero-field quantum yield  $\eta\zeta(0)$  (Eq. 6.13), which is a measure of the conversion efficiency from photons to free electrons. Figure 6.6 shows how the simulated  $C-V$  curves respond to orders of magnitude changes in the value of  $K$ . Watson *et al* used the  $K$  parameter to match the minimum capacitance of the simulated curve to the experimental one<sup>1</sup>. Here, however, the parameter influences the accumulation-depletion transition slope, making it less steep as  $K$  increases.



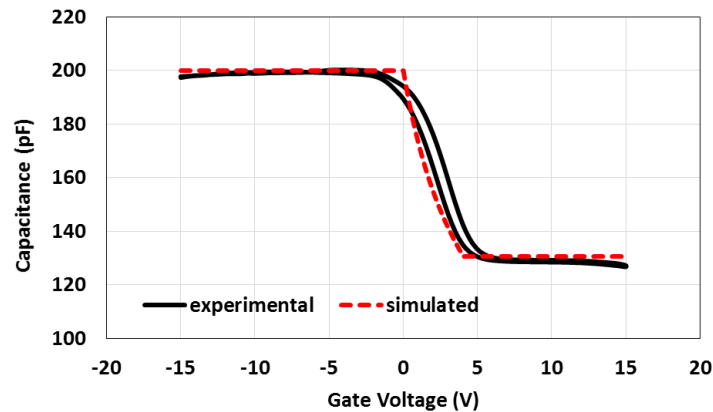
**Figure 6.6 – Effect of  $K$  value on the simulated  $C$ - $V$  curves using the new model. Values used for calculation were  $N_t = 1 \times 10^{18} \text{ m}^{-3}$ ,  $(E_c - E_t) = 0.65 \text{ eV}$ ,  $(E_c - E_{fn}) = 1.2 \text{ eV}$ .**

The effect of different interface trap densities,  $N_t$ , is demonstrated in Figure 6.7. As can be seen, an increasing trap density increases the minimum capacitance. This is readily explained. In the presence of strong trapping, the minimum capacitance occurs when the incremental change in applied voltage is matched by the shift in  $V_{FB}$ . At higher trap densities, for a given generation rate in the depletion region i.e. reduced band bending, trap occupation will occur more rapidly, resulting in a higher minimum capacitance. The forward and reverse sweep slopes (transitions between accumulation and depletion) were not affected by the density of traps.



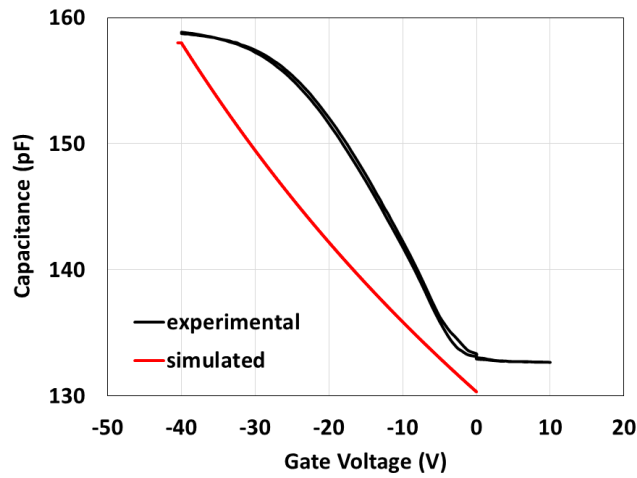
**Figure 6.7 – Effect of  $N_t$  value on the simulated  $C$ - $V$  curves using the new model. Values used for calculation were  $K = 1 \times 10^{10}$ ,  $(E_c - E_{fn}) = 1.2$  eV,  $(E_c - E_i) = 0.65$  eV.**

With the assumption that not all charges reaching the semiconductor/insulator interface become trapped, the improved model could be used to simulate the  $C$ - $V$  curves obtained in Chapters 4 and 5. Figure 6.8 shows the comparison between the experimental  $C$ - $V$  curve of a P3HT MIS capacitor in the dark (Figure 4.3a; black curve) and the simulated curve obtained from the model (red slashes). The device parameters used in the simulation, i.e. area, semiconductor thickness ( $d_{\text{semi}}$ ) and relative dielectric constant ( $\epsilon_r$ ) were obtained from section 4.2.1. Both experimental and simulated  $C$ - $V$  curves follow the same pattern with accumulation at  $\sim 200$  pF and a minimum capacitance level of  $\sim 130$  pF. The simulated accumulation-depletion transition also fits the experimental curve with the only difference being a small hysteresis in the reverse sweep and the edges of the accumulation-depletion transition.



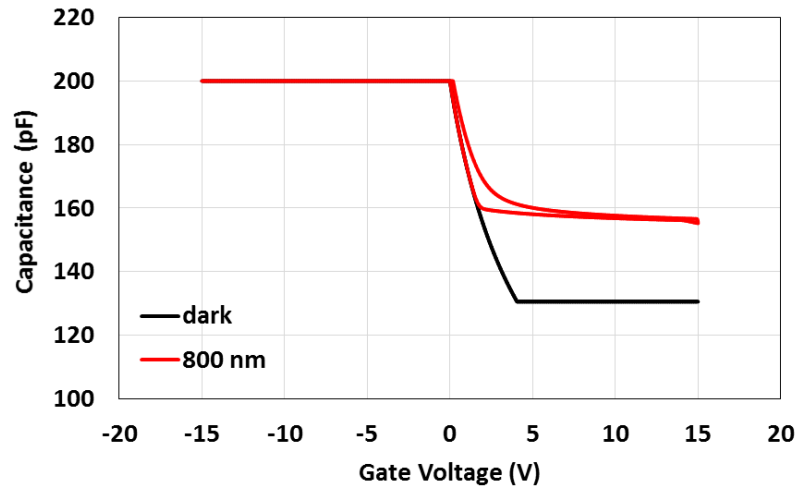
**Figure 6.8 – Experimental and simulated  $C$ - $V$  curves for a P3HT MIS capacitor in dark. Values used for calculation were  $\epsilon_r = 3.4$ ,  $C_I = 200$  pF,  $d_{\text{semi}} = 80$  nm,  $K = 0$ ,  $N_t = 1 \times 10^{18}$ ,  $E_c - E_{fn} = 1.6$ ,  $E_c - E_t = 0.65$ .**

Figure 6.9 shows the comparison between the experimental  $C$ - $V$  curve of a DNTT-based MIS capacitor in vacuum, in dark (Figure 5.5; black curve) and the simulated curve obtained with the model (red slashes). As mentioned in Chapter 5, the fabricated DNTT capacitors had a strong  $V_{\text{FB}}$  shift evidenced by the  $C$ - $V$  curves. Since the model starts the calculation at  $-0.4$  V, the simulated curve had to be adjusted by  $-40$  V to match the start of the experimental  $C$ - $V$  curve. The adjusted simulated curve fail to simulate the slope at which the capacitance goes from accumulation to depletion. The experimental curve was smoother and less steep both at the beginning and at the end of the transition, while the simulated  $C$ - $V$  curve shows roughly the same slope throughout the interval. In order to make the accumulation-depletion transition span from  $-40$  V to  $0$  V, the NA value had to be increased to  $10 \times 10^{23} \text{ m}^{-3}$  which is much higher than the value used for P3HT ( $5 \times 10^{22} \text{ m}^{-3}$ ).



**Figure 6.9 – Experimental and simulated  $C$ - $V$  curves for a DNTT MIS capacitor in dark. Values used for calculation were  $\epsilon_r = 3$ ,  $C_I = 158$  pF,  $d_{\text{semi}} = 80$  nm,  $K = 0$ ,  $N_t = 1 \times 10^{18}$ ,  $E_c - E_{fn} = 0.01$ ,  $E_c - E_t = 0.60$ .**

Figure 6.10 shows the simulated curves when the device was exposed to light with different wavelengths, as in Figure 4.6. To match the same minimum capacitance level of the experimental  $C$ - $V$  curves, the values of the parameters  $K$ ,  $\alpha$ ,  $N_t$ ,  $E_c - E_{fn}$  and  $E_c - E_t$  were adjusted accordingly. Since each parameter used in the modelling indirectly affects the behaviour of all the others, and hence, the overall shape of the  $C$ - $V$  curve, the task of finding a perfect match for a specific experimental capacitance curve is time consuming.



**Figure 6.10 – Simulated  $C$ - $V$  curves for a P3HT MIS capacitor in dark. Values used for calculation were  $\epsilon_r = 3.4$ ,  $C_I = 200$  pF,  $d_{\text{semi}} = 80$  nm,  $K = 0$ ,  $N_t = 1 \times 10^{18}$ ,  $E_c - E_{fn} = 1.6$ ,  $E_c - E_t = 0.65$ .**

## CONCLUSION

An improved model, used to describe the main features observed during an admittance measurement, was discussed during this chapter. The previous model correctly predicted the behaviour of MIS capacitors with extensive electron trapping at the semiconductor/insulator interface, but failed to simulate the behaviour of more general devices where trapping is not as prominent. To tackle this problem, the electron capture and emission rate by traps were introduced. Free electrons that escaped traps with the aid of the electric field within the depletion layer could now recombine, effectively removing their influence on the admittance measurement and decreasing the shift in flatband voltage caused by the interface traps.

By changing the value of the energy level parameters, the improved model can be tuned to represent devices where the hysteresis is not large, as the simulated curve of Figure 6.10 shows. However, due to the inherent interconnection between all the parameters, changing one parameter by a small amount can lead to a cascade of effects

which can change the behaviour of the whole simulated  $C$ - $V$  curve. Finding a set of parameters that correctly simulates the features observed in an experimental curve proved to be challenging.

## REFERENCES

- <sup>1</sup> C. P. Watson, M. Devynck, and D. M. Taylor, *Organic Electronics* **14**, 1728 (2013).
- <sup>2</sup> M. Devynck, B. Rostirolla, C. P. Watson, and D. M. Taylor, *Applied Physics Letters* **105**, 183301 (2014).
- <sup>3</sup> S. M. Sze, *Physics of Semiconductor Devices* (John Wiley & Sons, 1981).

# CHAPTER 7

## CONCLUSIONS & FUTURE WORK

### 7.1 Conclusions

In summary, the operation of organic-based MIS capacitors, using the well-known blend of P3HT:PCBM and the small molecule DNTT as active layer materials, was investigated under different ambient conditions. The operation of DNTT transistors, in combination with Lisicon D207-MAK as the insulator layer, was also the object of investigation. An improved model was derived to better explain the features observed in the C-V plots of the MIS capacitors.

The overall C-V behaviour of P3HT:PCBM MIS capacitors, discussed in Chapter 4, followed that of a p-type semiconductor, with accumulation of holes at negative bias and formation of a depletion region with positive voltages. When the device was exposed to light of different wavelengths, minimum capacitance shifts was observed which followed the absorption profile of the blend. Contrary to P3HT-only devices, the recovery of the device was quick, indicating that fast transfer processes between the polymer and the blend were in place. When incorporated in a CID, the

blend did not display any electron transfer showing that PCBM aggregated as island in the P3HT, not allowing for any charge transport along the semiconductor/insulator interface. Response to NIR light was also shown by the blend-based capacitor, which was investigated with the use of different LUMO level PCBM-like molecules. The results indicated that the NIR-absorption was likely to be related to the energy difference between the HOMO of the polymer and the LUMO of the fullerene energy level.

In Chapter 5, the behaviour of DNTT-based devices was investigated. The overall behaviour of DNTT MIS capacitors followed that of a p-type semiconductor. However, different responses were obtained when the device was illuminated when in air and when under vacuum. The hysteresis shifts were only visible when the device was exposed to air and light at the same time and when significant electric fields near the gold electrode were present. These results suggest that DNTT-based devices are prone to photo-assisted charge injection in the presence of air. The effect of bias stress on DNTT MIS capacitors was also investigated. After being biased part way down the accumulation-depletion transition for over 1000 min, the admittance plots shifted to more negative values, indicating the presence of interface hole traps. For this to happen, a source of holes at the interface would be required, suggesting that the semiconductor was acting as an intrinsic material in partial accumulation. This affirmation could change the way DNTT devices are analysed and require more investigation.

In order to explore the `dual-gate` light sensor idea, DNTT transistors were fabricated using Lisicon D207-MAK as the insulator layer. The semiconductor/insulator pair proved to be very reliable as the yield of working transistors, after 2.5 days of air exposure, was higher than 95% for the 90 transistors tested. The improvement over 2.5 days of air exposure was attributed to a decrease in barrier height, which facilitated the injection of charges from gold into DNTT. The data spread was also not observed, with all 9 transistors fabricated with the same geometry behaving very similarly to one another. Their linear mobility saturated at  $\sim 0.2 \text{ cm}^2/\text{Vs}$  and the mobility calculated from the saturation regime reached a maximum value of  $\sim 0.4 \text{ cm}^2/\text{Vs}$ . Such low values, when compared to other DNTT transistors in the

---

literature, were attributed to the rod-like structures of the DNTT film deposited on top of Lisicon D207-MAK. These rod-like features are exclusive to the combination Lisicon D207-MAK/DNTT and are not found in other DNTT-based devices.

Chapter 6 discusses the theoretical model used to explain the main features observed in the C-V plots of organic-based MIS capacitors. The improved model introduced the idea of electron capture and emission rate by traps, which were used to better describe the hysteresis effect observed in devices where trapping is not prominent. By changing the value of the energy level parameters, the improved model can be tuned to represent devices where the hysteresis is not large. However, due to the inherent interconnection between all the parameters, changing one parameter by a small amount can lead to a cascade of effects which can change the behaviour of the whole simulated C-V curve. Finding a set of parameters that correctly simulates the features observed in an experimental curve proved to be challenging.

## 7.2 Further Work

The dependence of the energy difference between  $\text{HOMO}_{\text{P3HT}}$  and  $\text{LUMO}_{\text{PCBM}}$  on the NIR light absorption of P3HT:PCBM-based MIS capacitors could be further investigated. Using different combinations of P3HT and PCBM with different HOMO and LUMO levels could highlight the shift of the NIR absorption, evidencing the nature of the effect. This absorption band is not usually explored in devices based on these materials.

Further studies on the morphology of the P3HT:PCBM blend could improve the understanding of the lack of electron transfer in the CID device. Controlling the surface tension of the insulator could help create a layer of PCBM where electrons can be transferred along the semiconductor/insulator interface. This would allow for better device performance as a proto CCD, as device recovery was substantially improved

with the addition of PCBM in the active layer. This could be achieved by using different solvents for the blend, as chlorobenzene. Once these points are better understood, the CID device geometry could be extended to allow for multiple stage transfers.

After the right morphology is found, the blend could be used as the active layer in the ‘dual gate’ light sensor idea. A similar device structure was already published using DNTT as the transistor’s active layer, proving the feasibility of the concept<sup>1</sup>.

The behaviour of DNTT under light and air is a point of interesting discussion. Usually, organic semiconductors are assumed to be n- or p-type doped, but the overall admittance behaviour of DNTT suggests that an evaporated small molecule could be intrinsic. Different DNTT MIS capacitors geometry could be fabricated to further investigate how fast the effects of the electron injection from the gold electrode takes place.

The theoretical model that describes the features observed in the C-V plots could be further improved. The way the different parameters interact made the programming part challenging and the search for an experimental fit was time consuming. The code requires further development.

---

<sup>1</sup> A. Pierre, A. Gaikwad, and A. C. Arias, *Nature Photonics* **11**, 193 (2017).

# APPENDIX A

The MATLAB code used in the simulations described in Chapter 6 is detailed here.

```
function [Nt]=CVSimulation

%%%constants%%%
q=1.602e-19;           %electric charge (C)
ep0=8.854e-12;        %vacuum permitivity (F/m)

%%%variables%%%
Na=4e25;              %semiconductor doping (/m3)
Ci=1.55e-4;          %insulator capacitance (F/m2)
eps=3;                %semiconductor relative dielectric constant
area=1e-6;           %contact area (m2)
deltaT=0.001;        %delta time (s)%
scan=0.2;            %voltage step size (V/s)%
alpha=7.7e6;         %optical absorption (/m)
K1=0e08;             %photogenerated charge rate
s=0;                 %counter for array line number%
vg=-0.4;             %start gate voltage(V)
stop=60;             %stop gate voltage (V)
dsemi=80e-9;         %semiconductor thickness (m)
nt=0;               %initial number of trapped charges%
nf=0;               %initial number of free charges%
t=0;                %initial time (s)%
k=8.617e-5;         %Boltzmann constant (eV/K)%
T=300;              %temperature (K)%
sigma=1e-20;        %cross section area (m2)%
Vth=1e5;            %thermal velocity (m/s)%
Xt=1e18;           %Maximum trap charge density m-2%
Ecfn=1.6;          %Ec - Efn LUMO to electron fermi level (eV)%
Ect=0.65;          %Ec - Et LUMO to Trap level (ev)%
Trec=1e-3;         %Recombination period (s)%
dnt=0;             %initial delta nt
Nc=1e25;           %effective

%%% Pre calcs%%%
```

---

```

B=(2*Ci^2)/(eps*ep0*q*Na);
E=eps*ep0/Ci;
A1=K1*q*Na/(eps*ep0);
X=Vth*Nc*sigma;

%%%calculation%%

%forward sweep%

while (vg<=stop)
    vg=vg+deltaT*scan;
    t=t+deltaT;

    if vg>stop
        break
    end

    if K1>0;                                %check light ON/OFF

        ddep=real(E*sqrt(1+B*(vg-(q*(nt+nf)/Ci)))-E); %depletion width
        if ddep<0
            ddep=0;
        end
        if ddep<dsemi
            dn=A1*((ddep-(1-exp(-alpha*ddep))/alpha)); %generation rate
            phi=q*Na*(ddep^2)/(2*ep0*eps);           %band bending

            if dn>0;
                CapR=X*(Xt-nt)/(1+(exp((Ecfn-phi)/(k*T))));%Capture rate
                if CapR>dn;
                    CapR=dn;
                end
                if CapR<0;
                    CapR=0;
                end
                EmiR=X*nt*(exp(-Ect/(k*T)));          %Emission Rate
            else
                CapR=0;
                EmiR=0;
            end
            dnt=(CapR-EmiR)*deltaT;                    %delta trap
            dnf=dn*deltaT-(nf*deltaT)/Trec-dnt;        %delta free
            if dnt>dn;
                dnt=dn;
            end
            nf=nf+dnf;
            nt=nt+dnt;
            if nt<0;
                nt=0;
            end
            Vmax=vg; %set value for Vmax when ddep=dsemi
        end

        if ddep>=dsemi
            ddep=dsemi;

```

---

---

```

    dn=A1*((ddep-(1-exp(-alpha*ddep))/alpha)+(vg-Vmax)*(1-
(CM/Ci))*(1-exp(-alpha*ddep))*(K1/(A1*ddep)));
    phi=q*Na*(ddep^2)/(2*ep0*eps);           %band bending

    if dn>0;
        CapR=X*(Xt-nt)/(1+(exp((Ecfn-phi)/(k*T))));%Capture rate
        if CapR>dn;
            CapR=dn;
        end
        if CapR<0;
            CapR=0;
        end
        EmiR=X*nt*(exp(-Ect/(k*T)));           %Emission Rate
    else
        CapR=0;
        EmiR=0;
    end
    dnt=(CapR-EmiR)*deltaT;                   %delta trap
    dnf=dn*deltaT-(nf*deltaT)/Trec-dnt;       %delta free
    if dnt>dn
        dnt=dn;
    end
    nf=nf+dnf;
    nt=nt+dnt;
    if nt<0;
        nt=0;
    end
end
end

if K1<=0;
    ddep=real(E*sqrt(1+B*(vg-(q*(nt+nf)/Ci))-E));
    dn=0;
    CapR=0;
    EmiR=0;
    phi=0;
    dnf=0;
    dnt=0;
    Vmax=0;
    if ddep<0
        ddep=0;
    end
    if ddep>=dsemi
        ddep=dsemi;
    end
end

end

CM=Ci*eps*ep0/(eps*ep0+ddep*Ci); %calculated capacitance per
unit area

```

---

---

```

C=CM*area*1e12;                                %capacitance (pF)

%%populate output array
Nt(s+1,1)=vg;
Nt(s+1,2)=C;
Nt(s+1,3)=nt;
Nt(s+1,4)=nf;
Nt(s+1,5)=dn;
Nt(s+1,6)=ddep;
Nt(s+1,7)=t;
Nt(s+1,8)=CapR;
Nt(s+1,9)=EmiR;
Nt(s+1,10)=phi;
Nt(s+1,11)=dnf;
Nt(s+1,12)=dnt;
Nt(s+1,13)=Vmax;
s=s+1;
end
vg=stop;

%reverse sweep

while(vg>0)
    vg=vg-scan*deltaT;
    t=t+deltaT;

    if K1>0;                                     %check light ON/OFF
        ddep=real(E*sqrt(1+B*(vg-(q*(nt+nf)/Ci))-E));
%depletion width
        if ddep<0
            ddep=0;
        end
        if ddep<dsemi
            dn=A1*((ddep-(1-exp(-alpha*ddep))/alpha));
%generation rate
            phi=q*Na*(ddep^2)/(2*ep0*eps);
%band bending

            if dn>0;
                CapR=X*(Xt-nt)/(1+(exp((Ecfn-phi)/(k*T))));
%Capture rate
                if CapR>dn;
                    CapR=dn;
                end
                if CapR<0;
                    CapR=0;
                end
                EmiR=X*nt*(exp(-Ect/(k*T)));
%Emission Rate
            else
                CapR=0;
                EmiR=0;
            end
            dnt=(CapR-EmiR)*deltaT;                %delta
        end
    end
end
trap

```

---

---

```

                                dnf=dn*deltaT-(nf*deltaT)/Trec-dnt;                                %delta
free
    if dnt>dn
        dnt=dn;
    end
    nf=nf+dnf;
    nt=nt+dnt;
    if nt<0;
        nt=0;
    end
    Vmax=vg;                                %set value
for Vmax when ddep=dsemi
    end

    if ddep>=dsemi
        ddep=dsemi;
        dn=A1*((ddep-(1-exp(-alpha*ddep))/alpha)+(vg-Vmax)*(1-
(CM/Ci))*(1-exp(-alpha*ddep))*(K1/(A1*ddep)));
        phi=q*Na*(ddep^2)/(2*ep0*eps);
%band bending

        if dn>0;
            CapR=X*(Xt-nt)/(1+(exp((Ecfn-phi)/(k*T))));
%Capture rate
            if CapR>dn;
                CapR=dn;
            end
            if CapR<0;
                CapR=0;
            end
            EmiR=X*nt*(exp(-Ect/(k*T)));
%Emission Rate
        else
            CapR=0;
            EmiR=0;
        end
        dnt=(CapR-EmiR)*deltaT;                                %delta
trap
    dnf=dn*deltaT-(nf*deltaT)/Trec-dnt;                                %delta
free
    if dnt>dn
        dnt=dn;
    end
    nf=nf+dnf;
    nt=nt+dnt;
    if nt<0;
        nt=0;
    end
end
end

if K1<=0;
    ddep=real(E*sqrt(1+B*(vg-(q*(nt+nf)/Ci))-E));
    if ddep<0
        ddep=0;

```

---

---

```

        end
        if ddep>=dsemi
            ddep=dsemi;
        end
        dn=0;
        CapR=0;
        EmiR=0;
        phi=0;
        dnf=0;
        dnt=0;
        Vmax=0;
    end

    nf=nf+dnf;
    nt=nt+dnt;
    if nt<0;
        nt=0;
    end

    CM=Ci*eps*ep0/(eps*ep0+ddep*Ci); %capacitance per unit area
    C=CM*area*1e12; %capacitance (pF)
    %%%populate output array
    Nt(s+1,1)=vg;
    Nt(s+1,2)=C;
    Nt(s+1,3)=nt;
    Nt(s+1,4)=nf;
    Nt(s+1,5)=dn;
    Nt(s+1,6)=ddep;
    Nt(s+1,7)=t;
    Nt(s+1,8)=CapR;
    Nt(s+1,9)=EmiR;
    Nt(s+1,10)=phi;
    Nt(s+1,11)=dnf;
    Nt(s+1,12)=dnt;
    Nt(s+1,13)=Vmax;
    s=s+1;
end
%%plot data%%
plot(Nt(:,1),Nt(:,2),'k-','linewidth',2);figure(gcf);
xlabel('\fontsize{12}\bfBias (V)','fontname','times')%x-axis label
ylabel('\fontsize{12}\bfCapacitance (pF)','fontname','times')%y-axis
label
set(gca,'FontSize',12,'fontname','times')

```

# PUBLICATIONS AND CONFERENCES

## **PUBLICATIONS**

M. Devynck, B. Rostirolla, C. P. Watson, and D. M. Taylor, “*Photo-response of a P3HT:PCBM blend in metal-insulator-semiconductor capacitors*”, Applied Physics Letters 105, 183301 (2014)

## **CONFERENCES**

“*Charge Injection Device – A Diagnostic Tool*” B. Rostirolla and D. M. Taylor, 20<sup>th</sup> Merck CASE Conference, Brockenhurst, UK, April 28-29, 2014

“*P3HT:PCBM Based Metal-insulator-semiconductor Capacitors Under Visible and Near-infrared Light Stimulation*” B. Rostirolla and D. M. Taylor, 21<sup>st</sup> Merck CASE Conference, Brockenhurst, UK, April 13-14, 2015. Awarded best presentation from a 2<sup>nd</sup> year student.

“*P3HT:PCBM based metal-insulator-semiconductor capacitors under visible light stimulation*” B. Rostirolla and D. M. Taylor, XIV Brazil MRS Meeting, Rio de Janeiro, Brazil, September 27-30, 2015. Award best poster presentation in Symposium O.

“*Photo-effects in Organic MIS Devices*” B. Rostirolla and D. M. Taylor, 22<sup>nd</sup> Merck CASE Conference, Brockenhurst, UK, April 11-12, 2016.